UNIVERSIDAD AUTÓNOMA DE NUEVO LEÓN FACULTAD DE INGENIERÍA MECÁNICA ELÉCTRICA SUBDIRECCIÓN DE ESTUDIOS DE POSGRADO

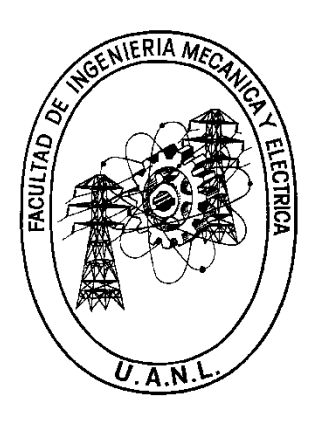


"Diesel engine connecting rod life assessment based on Static & Dynamic Finite Element Analyses."

Por: Ing. Marcelo Enrique García Martínez

EN OPCIÓN AL GRADO DE: MAESTRÍA EN CIENCIAS DE LA INGENIERÍA AUTOMOTRIZ

UNIVERSIDAD AUTÓNOMA DE NUEVO LEÓN FACULTAD DE INGENIERÍA MECÁNICA ELÉCTRICA SUBDIRECCIÓN DE ESTUDIOS DE POSGRADO



"Diesel engine connecting rod life assessment based on Static & Dynamic Finite Element Analyses."

Por: Ing. Marcelo Enrique García Martínez

EN OPCIÓN AL GRADO DE: MAESTRÍA EN CIENCIAS DE LA INGENIERÍA AUTOMOTRIZ

UNIVERSIDAD AUTÓNOMA DE NUEVO LEÓN

Facultad de Ingeniería Mecánica y Eléctrica Posgrado

Los miembros del Comité de Evaluación de Tesis recomendamos que la Tesis "Diesel engine connecting rod life assessment based on static & dynamic finite element analyses", realizada por el estudiante Marcelo Enrique García Martínez, con número de matrícula 1516995, sea aceptada para su defensa como requisito parcial para obtener el grado de Maestría en Ciencias de la Ingeniería Automotriz.

El Comité de Evaluación de Tesis

Dr. Mario Alberto Bello Gómez
Director

Dra. Adriana Salas Zamarripa Co-director

Dra. Tania Paloma Berber Solano Revisor

Dr. Diego Francisco Ledezma Ramírez Revisor

M.C. Jorge Alejandro Rodríguez Meléndez Revisor

Dr. Simon Martinez Martinez M

Subdirector de Estudios de osgrado

Institución

190001

Programa

554502

Acta Núm.

4503

Ciudad Universitaria, a Junio 2025.

To my beloved wife & daughter,
Hilda and Emilia,
for their support, love, and patience
during this academic process.

To my parents, for teaching me to pursuit higher education and values.

To my family, for always being present.

Acknowledgements

I want to thank the Deere & Co for their trust in investing in this project, to let me achieve a higher degree and support the in-house analysis development. The success of the company reflects the success of their employees inside and outside the work.

A debt of gratitude is also extent to the UANL-FIME, for providing the environment to increase the knowledge, methods, and qualified personnel to conclude this project. Given the opportunity to have me back as a student and allowing me to take this step further in my academic career.

The John Deere's Enterprise Technology and Engineering Center's – Intellectual Property Council for approving the business cases and sharing the vision of he added value to the unit and local talent to improve the analysis capabilities.

To my thesis director, PhD. Mario Alberto Bello Gomez, for setting a higher goal in this project, continuous feedback, support and always being present for discussion. Your methods allowed me to complete this project, nonetheless, your passion for investigation inspired me to enroll in this program.

To my thesis codirector, PhD. Adriana Salas Zamarripa, to let me know that the fatigue failures are just a glimpse of the engineering capabilities that are from many factors. No absolute truth exists, but a very good approximation can be obtained. Thanks for your advice and reality comebacks.

The knowledge obtained from experience obtained by Daniel Blake Walker triggered my will to invest more time in some of the unknowns from the field and take them to the virtual world. Thanks for your trust and sharing the facts that validate this project.

Finally, thanks to MSC. Jorge Alejandro Rodríguez Meléndez, for being a coach in the industry's needs, continuous feedback and mentoring in the final stages of this study.

Contents

Acknowledgements	2
Figure Index	6
Table Index	9
Acronyms	10
Summary	11
Chapter 1 Introduction	12
1.1 Motivation	13
1.2 Problem Statement	14
1.3 Hypothesis	14
1.4 Proposal	14
1.5 Objectives	15
1.5.1 General Objective	15
1.5.2 Specific Objectives	15
1.6 Methodology	15
Chapter 2 Internal Combustion Engine Fundamentals	18
2.1 Engine cycle & operation theory	18
2.1.1 Diesel cycle & otto cycle	19
2.2 Main components	24
Chapter 3 Connecting rod fundamentals	27
3.1 Connecting rod structure & manufacturing	27
3.2 Connecting rod dynamics	29
3.3 Connecting rod's bolted joint	34
3.4 Bearing crush	35
3.5 Body interactions within the connecting rod	37
3.6 Study approaches	38

Chapter 4 Fatigue analysis & testing	40
4.1 Fatigue life	40
4.2 Connecting rod testing	44
Chapter 5 Design of experiments	46
5.1 Methodology of the design of experiments	46
5.1.1 Designs' summary	48
5.1.2 Screening	48
5.1.3 Optimal designs	49
5.2 Factorial design of experiments in Minitab	50
Chapter 6 Finite element modelling & simulation	54
6.1 Introduction to FEA	54
6.2 Historical development	55
6.3 Methodology	55
6.3.1 Preprocessing	55
6.3.2 Processing	63
6.3.3 Postprocessing	64
6.4 Modelling approaches and applications	65
Chapter 7 Experimental process	67
7.1 Dynamic load calculation	67
7.2 Geometry description of Engine "A" connecting rod	68
7.3 Load case description	69
7.4 Factorial design of experiments	72
7.5 Finite element model description for the Engine "A" connecting rod	75
Chapter 8 Results & discussion	77
8.1 Testing Results	77
8.2 Design of experiments results	78
8.3 Finite element analysis results	81
8.3.1 Assembly state	82
8.3.2 Peak pressure condition at 1,900 r.p.m	83

8.3.3 Full load at rated speed at 2,400 r.p.m	86
8.3.4 Overspeed	89
8.4 Fatigue assessment results	92
Chapter 9 Conclusions & perspectives	95
Bibliography	97
Appendix	103

Figure Index

Figure 1.1 World population growth projection 1950-2050 [2]	12
Figure 1.2 Daimler - First four-wheeled [7]	13
Figure 1.3 Methodology flow	
Figure 2.1 Engine operating cycle scheme	20
Figure 2.2 Crank angle vs Pressure with Coefficient of Variation percentage [5	[22
Figure 2.3 Variable geometry turbocharger sample[10]	23
Figure 2.4 Engine performance curve sample [11]	24
Figure 2.5 Diesel engine section view [13]	25
Figure 2.6 Crank train components [15]	26
Figure 3.1 Connecting rod component description [18]	28
Figure 3.2 Fracture split connecting rod[21]	28
Figure 3.3 Connecting rod geometrical description	30
Figure 3.4 Angular acceleration of a connecting rod vs crank angle	33
Figure 3.5 Translational acceleration of the small end vs crank angle	33
Figure 3.6 Bearing crush on inspection gauge [10]	35
Figure 3.7 Oil hole concepts on connecting rod [24]	36
Figure 3.8 Flexible multibody simulation[3].	38
Figure 3.9 Modal analysis mode shapes of connecting rod [17]	39
Figure 4.1 Typical S-N Curve[31]	
Figure 4.2 Stress concentration factor based on Ra, Kt vs UTS [35]	
Figure 4.3 Surface roughness produced by common production methods [34].	.43
Figure 4.4 Connecting rod fatigue test bench[36]	44
Figure 4.5 Test rig sizes by Sincotec [37]	44
Figure 5.1 Design of experiments process overview	47
Figure 5.2 Cube plot sample[39]	47
Figure 5.3 graphical depiction of various experimental designs: (A) fractional	
factorial design, (B) Taguchi design, (C) Plackett-Burman design, (D) full facto	orial
design, (E) central composite design, (F) Box-Behnken design, (G) optimal	
design, and (H) mixture design [40]	
Figure 5.4 Available factorial designs[42]	
Figure 5.5 Pareto chart sample[44]	
Figure 6.1 2-D Element shape: triangular, rectangular, quadrilateral [48]	
Figure 6.2 (a) Tetrahedron, (b) Rectangular prism, (c) Arbitrary hexahedron, (c	
Three-dimensional quadratic [49]	56
Figure 6.3 Element discretization of a domain[45]	
Figure 6.4 Free-body diagram of a linear spring element	58

Figure 6.5 FEA model of linear springs	59
Figure 6.6 Max and min principal stress plot sample	65
Figure 7.1 Connecting rod components for simulation	68
Figure 7.2 Fillet radius detail of first revision	68
Figure 7.3 Output torque vs Engine speed curve	69
Figure 7.4 Firing pressure vs Engine speed curve	70
Figure 7.5 Load cases description.	70
Figure 7.6 Load cases summary per engine speed	72
Figure 7.7 Mesh generated for the simulation	75
Figure 7.8 Contact status of geometry in FE	76
Figure 8.1 Broken connecting rod of engine "Engine "A"	
Figure 8.2 Crack initiation site of the connecting rod in Engine "A"	78
Figure 8.3 Pareto chart of effects	80
Figure 8.4 Main effects plot for alternating stress (Salt)	80
Figure 8.5 Cube plot for alternating stress (Salt)	81
Figure 8.6 A1 Assembly Max & Min Principal Stress	82
Figure 8.8 A1 Firing Max & Min Principal Stress at 1,900 r.p.m	83
Figure 8.10 A1 Whip 90° Max & Min Principal Stress at 1,900 r.p.m	84
Figure 8.11 A1 Whip 270° Max & Min Principal Stress at 1,900 r.p.m	84
Figure 8.14 A1 Pull Max & Min Principal Stress at 1,900 r.p.m	85
Figure 8.16 A1 Firing Max & Min Principal Stress at 2,400 r.p.m	86
Figure 8.18 A1 Whip 90° Max & Min Principal Stress at 2,400 r.p.m	87
Figure 8.19 A1 Whip270° Max & Min Principal Stress at 2,400 r.p.m	87
Figure 8.22 A1 Pull Max & Min Principal Stress at 2,400 r.p.m	88
Figure 8.24 A1 Whip 90° Max & Min Principal Stress at 3,600 r.p.m	89
Figure 8.25 A1 Whip 270° Max & Min Principal Stress at 3,600 r.p.m	89
Figure 8.28 A1 Pull Max & Min Principal Stress at 3,600 r.p.m	90
Figure 8.29 A2 Pull Max & Min Principal Stress at 3,600 r.p.m	
Figure 8.30 Safety factor A1 – Engine operation	92
Figure 8.31 Safety factor A2 – Engine operation.	92
Figure 8.32 Safety factor A1 - Engine operation + Overspeed	93
Figure 8.33 Safety factor A2 - Engine operation + Overspeed	93
Figure 8.34 Revision 1 at fillet, FoS = 0.99	94
Figure 8.35 Revision 2, FoS = 1.23	94
Figure 10.1 A2 Assembly Max & Min Principal Stress	103
Figure 10.2 A2 Firing Max & Min Principal Stress at 1,900 r.p.m	103
Figure 10.3 A2 Whip 90° Max & Min Principal Stress at 1,900 r.p.m	104
Figure 10.4 A2 Whip 270° Max & Min Principal Stress at 1,900 r.p.m	104

Figure 10.5 A2 Pull Max & Min Principal Stress at 1,900 r.p.m	105
Figure 10.6 A2 Firing Max & Min Principal Stress at 2,400 r.p.m	105
Figure 10.7 A2 Whip 90° Max & Min Principal Stress at 2,400 r.p.m	106
Figure 10.8 A2 Whip 270° Max & Min Principal Stress at 2,400 r.p.m	106
Figure 10.9 A2 Pull Max & Min Principal Stress at 2,400 r.p.m	107
Figure 10.10 A2 Whip 90° Max & Min Principal Stress at 3,600 r.p.m	107
Figure 10.11 A2 Whip 270° Max & Min Principal Stress at 3,600 r.p.m	108

Table Index

Table 5-1 Resolution differences	51
Table 6-1 Degrees of freedom and force vectors per discipline	57
Table 6-2 Node and element connectivity table	60
Table 6-3 Element stiffness decomposition	61
Table 6-4 Force contribution per element	62
Table 6-5 Solution to displacements	64
Table 7-1 Design summary	72
Table 7-2 Alias structure naming	73
Table 7-3 Alias structure	73
Table 7-4 Design table (randomized)	74
Table 8-1 Testing loads	77
Table 8-2 Coded coefficients for the factors	78
Table 8-3 Coefficient of determination	79
Table 8-4 Analysis of variance	79
Table 8-5 Safety factor (FoS) on fillet	

Acronyms

<u>Abbreviation</u> <u>Definition</u>

UANL Universidad Autónoma de Nuevo León FIME Facultad de Ingeniería Mecánica y Eléctrica

BEV Battery Electric Vehicle AV Autonomous Vehicle

ICE Internal Combustion Engine
CAD Computer-aided Design
BMT Brake Maximum Torque

COV Coefficient of Variation Percentage

FE Finite Element
HCF High Cycle Fatigue
LCF Low Cycle Fatigue

UTS Ultimate Tensile Strength
FEM Finite Element Method
FEA Finite Element Analysis

EO Engine operation

OS Overspeed

COF Friction coefficient
MBS Multibody simulation
ANOVA Analysis of variance

FFD Fractional Factorial Design

DOF Degree of freedom EPU AVL's Excite PU

ARD Ansys Rigid Dynamics Ecalc Excel based calculator

SS Sum of squares
MS Mean of squares
T.D.C. Top Dead Center
B.D.C. Bottom Dead Center
S1 Maximum principal stress
S3 Minimum principal stress

FoS Safety factor

Summary

Product development methodologies are continuously evolving and, in the need, to catch up with markets and population's needs. The usage of the internal combustion engines as a power source since the last century is evolving with the trends of lower emissions.

The methodology developed in this work intends to establish a safety factor through numerical simulation. Reducing the cost needed for design, optimization, and production of the connecting rod and consequently the engine. The connecting rod is one of the key members of the crank train components and is subjected to high inertial loads, as well as compressive forces.

By using the classical dynamics and cutting-edge simulation techniques, it was associated with a crack from fatigue testing on a production connecting rod. The usage of a factorial design of experiments allowed to evaluate the impact of the factors that cause the effects on fatigue crack.

The safety factor results are obtained matching the location where crack initiation due to fatigue present. To support these results, the design of experiments showed that the firing and pull forces of the connecting rod have the highest alternating stress, which can lead to a fatigue crack.

It was concluded that the test will not show the bending failures due to the lateral acceleration but could be captured and evaluated through the simulation. While the firing events and the axial inertial force are well replicated by the testing techniques.

Designing the connecting rod to endure the testing will leave a small margin for failure due to the lateral accelerations. However, the failure modes caused by improper manufacturing techniques, surface finishes, material specification are not covered by the limitation of the analysis tool.

Further study in manufacturing defects is encouraged to replicate and prevent unexpected outcomes not limited to connecting rods will be a key for future developments. However, it depends on the quality of the inputs for the simulation and the evidence acquired historically on the components.

Chapter 1 Introduction

The development of heavy machinery and engineering solutions has always been driven by the increasing demands on goods and services throughout history. Present days the world is facing the upcoming challenge on providing food and shelter to the coming population by [1] people, a projection can be observed in Figure 1.1.

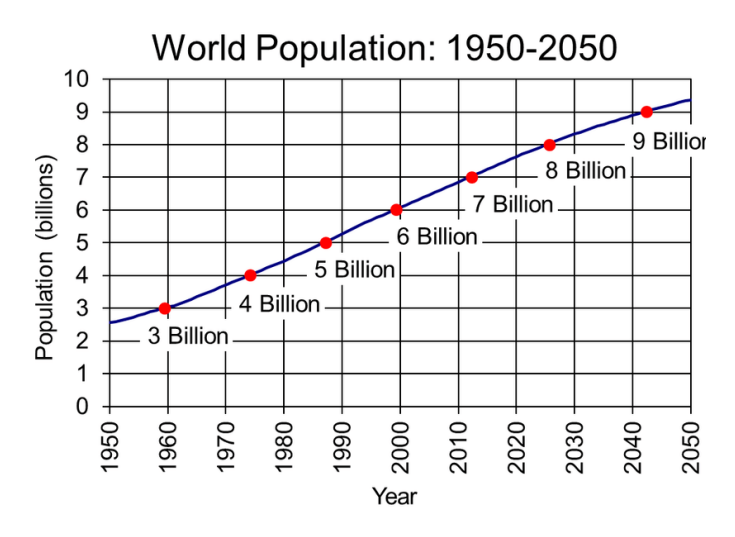


Figure 1.1 World population growth projection 1950-2050 [2]

Despite that the global trends pointing to electrification in vehicles, where the power train is mainly an electric motor powered by a battery (BEV, Battery Electric Vehicle) and autonomous vehicle (AV), they are still under development [1].

On other hand, hydrogen is becoming a primary option in the pursuit of decreasing ${\it CO}_2$ emissions [3]. Now, various scenarios have been studied within hydrogen blends and pure hydrogen in terms of power generation. For gas engines, spark ignited, modifications for hydrogen compliant materials are not expected to cost more than 30%.

This might give another opportunity for the internal combustion engine to continue production lines, not only for heavy machinery but also on-road applications [4]. Another major advantage is that the tooling costs might not have a major increase since they use a similar components type.

The four-stroke internal combustion engine (ICE) was introduced by Nicolaus Otto and Eugen Langen in 1876 [5]. By 1886 Karl Benz invents the first motorized tricycle, giving birth to the automotive industry [6]. In parallel, Gottlieb Daimler and

Wilhelm Maybach created the first four-wheeler, gas-engine vehicle, as shown in Figure 1.2

The engine cycle has not changed since, but the method to improve efficiency, fuel consumption, speed, torque, among other key characteristics have been improved through the years.

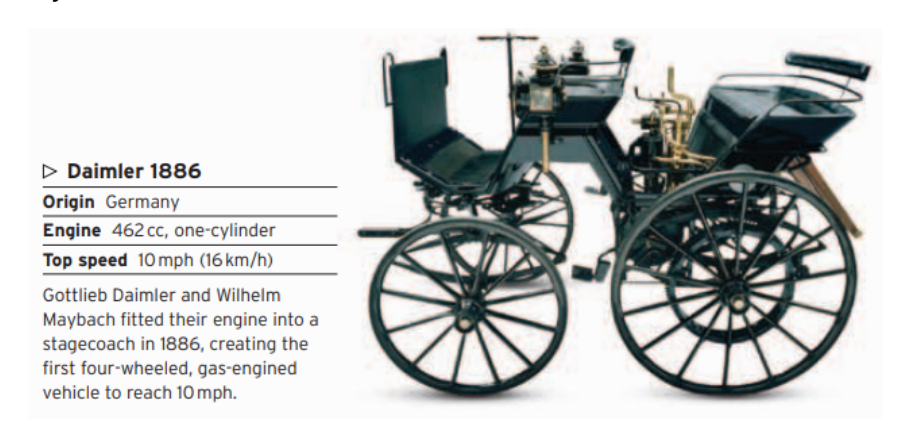


Figure 1.2 Daimler - First four-wheeled [7]

The ICE, however, has its basic mechanism from the slider crank concept, developed in modern times by Franz Reuleaux in 1882 [8]. Where the connecting rod is the linking element for the crankshaft and piston. Two of the main components to transmit combustion power to an output torque.

1.1 Motivation

The focus of this study is to increase the certainty of the durability of the connecting rods on diesel engines. This subject has been relevant with the increase of numerical simulation predictive capabilities. It could impact directly on the testing of the component and subsequently the cost attached to it. The benefits of this study are mainly linked to the correlation between the physical approach and the virtual duty cycles that apply.

The method to be developed has the intention of fostering the multidisciplinary subjects of static, dynamic, statistics and fatigue phenomena undergoing simultaneously at the connecting rods.

Currently the extent of the simulation methods is continuously expanding, and in some cases, it cuts the testing of certain components. Increasing the fidelity of the models plus the correlation of design points can empower the usage of the virtual

tools, as well as the support of calculations from classic mechanics to close the loop between the theory, simulation, and practice.

The connecting rod as a subject of study will not be limited to ICE, since there are other machines that use this type of components e.g., compressors, dies, cutting machines, presses, etc. For future applications, as previously mentioned, the hydrogen engine could become the first candidate to apply this validation method.

1.2 Problem Statement

Currently the physical and virtual validation procedure of the connecting rod is being simplified as a compression and tension cases. These values are given by the cylinder pressure caused by the firing event on an engine, while the tension force is given by the acceleration of the piston and the reciprocating mass. The lateral loads of the connecting rod are not being reflected on any test in the present day.

There is a need for a procedure that can assess the stresses on the connecting rod due to the different loads that happen during an engine's duty cycle, regardless of the application vehicle.

1.3 Hypothesis

A fatigue safety factor could be established, which will determine if the connecting rod could endure an engine's duty cycle and correlates with the current testing in laboratory. Where the inertial loads of the engine cycle could be taken in count, without disregarding the firing event's forces.

1.4 Proposal

From the correlation of design points and testing, diverse finite element models will be generated, where the boundary conditions will reflect an engine duty cycle. The known conditions are idle, maximum torque, overspeed and full load at rated speed.

Additionally, other models will also be generated, where the test bench conditions will be applied. Once the results are correlated, a fatigue and life assessment will be done. The main output of this project will be the definition of the acceptance criteria.

1.5 Objectives

1.5.1 General Objective

Establish a stress-based fatigue safety factor by performing a series of finite element simulations that include the engine's duty cycle loads and correlates crack locations from field or testing.

1.5.2 Specific Objectives

- Select a low and high-performance promise engine and obtain the CAD, duty cycles, torque curve, crank angle vs cylinder pressure curve, and field crack information.
- Obtain the material properties of the components selected, including S-N curves.
- Conduct finite element simulations for both engine programs, boundary conditions to be evaluated from design points, hand calculations and supporting analysis.
- Analyze the results obtained from the simulations and conduct a fatigue safety factor assessment.

1.6 Methodology

The following diagram (Figure 1.3) shows the basic steps to be taken for the fatigue safety factor study.

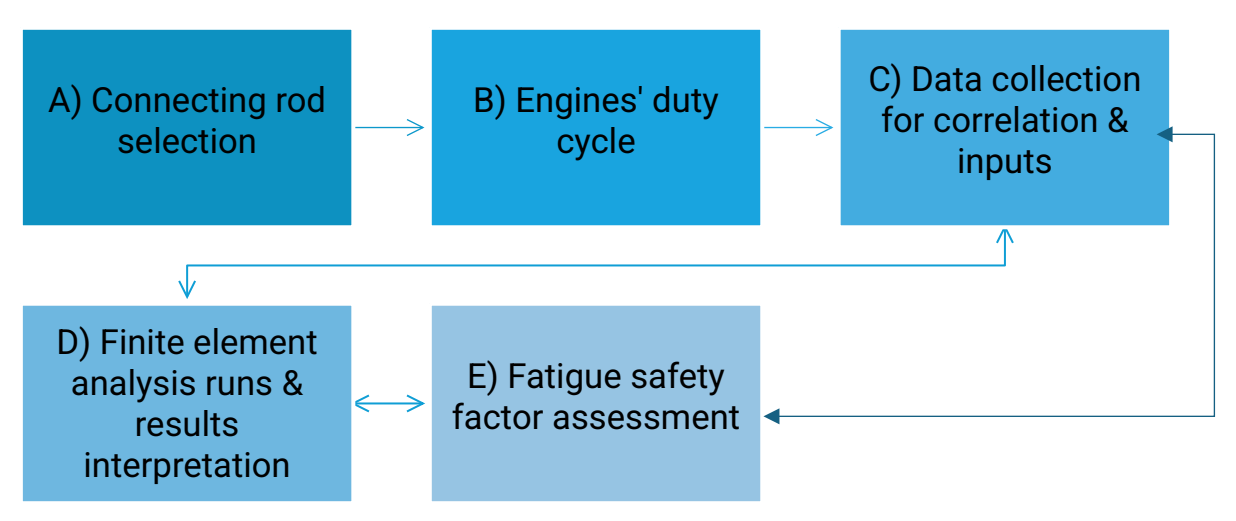


Figure 1.3 Methodology flow

- A) There are two known connecting rods that have shown high & low operational discrepancy on test and field. The geometry in CAD format (.step) is needed on the versions that have shown the cracks and updated if available.
- B) The engine duty cycle should be constructed of the engine torque curve, crank angle vs cylinder pressure behavior and the load versus rpms map of the available field data.
- C) For all connecting rods released on the market, there is fatigue test bench information, as well as the corresponding evidence of the deviation from standards of the field. This also might include the material's engineering reports. The SN fatigue data of the materials is also needed for study.
- D) The finite element analysis runs will be considering the dynamic loads of the connecting rod, with basis on the reciprocating crank slider mechanism. The forces can be hand-calculated with the following assumptions [2]:
 - 1. Force on the piston due to gas pressure and inertia of the reciprocating parts.
 - 2. Force due to inertia of the connecting rod or inertia bending forces.
 - 3. Force due to friction of the piston's rings and of the piston.
 - 4. Force due to friction of the piston pin bearing and crankpin bearing.
 - i. The dynamic forces will be generated through Ansys explicit dynamics module. In the procedure carried out by Göös[3] was conducted through AVL's Power Unit module and later added to the model. Different in this process is going to add nonlinearities such as frictional contacts.
 - ii. Bearing assembly can have a reality check based on the radial pressure generated by the bearing crush [2].
 - 5. The information of the duty cycles will be used as a starting point for the inputs and to get more boundary conditions that can increase the

fidelity of the model.

E) The fatigue assessment will be initially conducted using the Haigh diagram [9]. Afterwards it will be conducted a separate study to calculate the fatigue safety factor on Fe-Safe.

The limitations of the study are subjected to the theoretical correlation of the load cases and missing the so-called known unknowns, temperature, material degradation, forging direction, etc. Where the relationship of the inherent physical boundary conditions of the engine with the components are based on historical and empirical evidence. Some of this limitations are the hydrodynamic loads, material homogeneity and temperature profile at the different positions of the connecting rod during the cycle.

In the upcoming chapters the fundamentals of the internal combustion engine will be reviewed as a starting point, to be followed by the connecting rods. Next, since it is a component subjected to high cycle fatigue regime it will be given a detail of the fatigue studies. The study required a strategy for setting up the experimental process, where a design of experiments was used.

The experimental process was conducted on a virtual assessment, using the finite element analysis where its foundations will be brought to detail and application. Finally, the results of the experiment and its corresponding conclusions will be shared with a given perspective of the industry standpoint and program schedule.

Chapter 2 Internal Combustion Engine Fundamentals

In this chapter, it will cover the internal combustion engine foundations. As it stands as one of the key inventions that combined the transformation of thermal energy into mechanical power. The process has undergone little change since its invention with both cycles, Otto and Diesel. Where it relies on the combustion within a chamber, generating a strong impulse that feeds a rotating array of components. The intention of this chapter is to provide the theoretical basis for the different components that integrate the engine, with some emphasis on the key components, thermodynamics and operation.

2.1 Engine cycle & operation theory

Power of the internal combustion engine is generated by the combustion event. Combustion is the rapid oxidation of combustible substances with a release of heat. Carbon and hydrogen are the most important of the combustible substances, while oxygen is the main supporter of the event. Only sulfur is considered a combustible element. It also plays a key role in the pollution control since its presence must be reduced to avoid high emissions [10].

The thermodynamic analysis of the internal combustion engine is carried out with the assumption of the idealized air cycle. This approach is widely used due to the simplicity of having an initial result of the engine's design, however it sacrifices the accuracy of the real behavior and does not consider some of the limitations that happen physically.

The internal combustion engine is a heat engine where the chemical reaction (combustion) is the energy source due to the burn of the working fluid. In contrast, external combustion engines, such as the steam powered engines have their heat source from an external boiler for instance [10].

Operation basics of the ICE are listed as follows [10]:

- 1. Intake: The working volume increases, while the intake valve is being open to let enter air or an air/fuel mixture.
- 2. Compression: The working volume decreases; the intake valve is closed, and the mixture is compressed.
- 3. Combustion & expansion: The mixture burns and releases chemical energy, if only air was compressed the fuel is injected in this step. Due to

- expansion, the pressure increases rapidly and the working volume increases.
- 4. Exhaust: Engine working volume decreases, while the exhaust valve is open to release the combustion products.

2.1.1 Diesel cycle & otto cycle

Some conditions on positioning of the system on the engine have known descriptions. Top-Dead-Center (T.D.C.) is the position of the piston when it stops at the furthest point away from the crankshaft. *Top* since it is at the top of most engines, and *dead* due to the stop of the piston at this point. In counterpart, the Bottom-Dead-Center (B.D.C) is basically at 180° from T.D.C. having the piston closest to the crankshaft [4].

Some other definitions relevant to the basics of the engine are as follows:

- 际 Bore: Diameter of the cylinder or diameter of the piston face.
- 际 Stroke: Movement of the piston from T.D.C. to B.D.C. and vice versa.
- 际 Displacement Volume: Volume displaced by the piston while it travels through one stroke.
- 际 Brake maximum torque (BMT): Speed at which maximum torque occurs.

The most popular arrangement for cycles on the engines on heavy machinery and on road applications is the four-stroke engine. The following steps describe in more detail the stages in a Diesel engine, since it is a compression combustion engine [4].

- At the intake stroke the piston travels from T.D.C to B.D.C. while the intake valve is open, and the exhaust valve closed. Since most Diesel engines are turbocharged the volume in the chamber increases during a supply of compressed air from to the compressor attached to the turbocharger.
- 2. In the compression stroke, the piston reached the B.D.C. The piston starts travelling back to T.D.C. with all valves shut. At this stage only the air is compressed, and this compression leads to higher pressure and temperature. At the end of the compression, the fuel is injected into the cylinder fostering a mix with the hot air within self-igniting and starting the combustion.
- 3. The combustion is full when the piston has already reached the T.D.C. Having the pressure effect on the piston, started travelling back to B.D.C.

- 4. At the third stroke, the power obtained continues as the combustion is ending and the piston continues its travel toward B.D.C.
- 5. Late at the previous stroke, the exhaust valve is opened, and the remains of the combustion are blown down through the valve. The pressure and temperature are still high in comparison to the surroundings. The turbo at the manifold in this case generates a vacuum and gets power from the exhaust gas.
- At the time the piston reaches the B.D.C. the exhaust blowdown is completed, but the cylinder still has gas remains. This last stroke is when the piston travels back to T.D.C. pushing the remains through the exhaust valve.

A graphical scheme is presented in the following diagram in Figure 2.1.

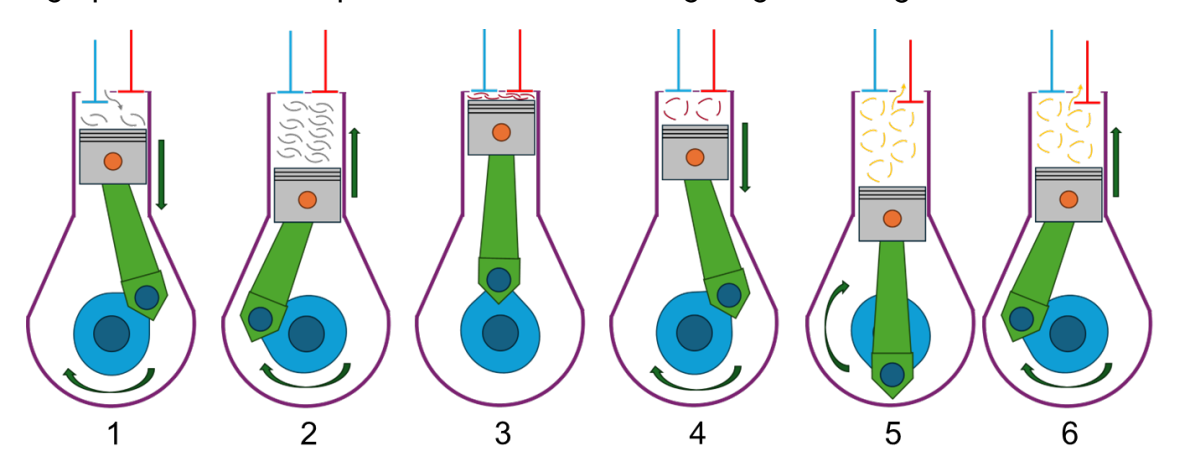


Figure 2.1 Engine operating cycle scheme.

There is a characteristic behavior of the cylinder pressure at a given crank angle as observed in Figure 2.2. Since the pressure in the cylinder is changing, a mean effective pressure can be calculated by the Equation 2.1. Hence, the total force will be proportional to the surface area on which that pressure is applied [4]. For the connecting rod according to the previous stroke scheme it can be determined some of the load cases to be performed.

$$mep = W/V_d$$
 Equation 2.1

Where:

际 mep = mean effective pressure

际 V_d = displacement volume

It has been studied as well that the cycle-by-cycle can be evaluated by analyzing the cylinder pressure traces of each cycle against the crank angle. The effects can vary due to the rate of change in burning, as the volume. Other factors as well can be the variation of the combustion compared to the T.D.C., the magnitude and the shape of the heat release rate [5].

There is an impact on the cylinder pressure generated by the combustion, depending on the following items: mixture content, injection timing according to the crankshaft angle, injection pressure, fuel type. To begin with the mixture content, increasing biodiesel in a mixture can reduce the combustion noise, ignition delay, the mep, and cylinder pressure [6].

This has a particular effect on the power output since the cylinder pressure is linked with the torque output. The position of the crankshaft has a significant role, for instance at -2°, mep, combustion noise, and burn duration decrease, while the ignition delay increases. On the contrary, +4°, cylinder gas pressure increases getting close to the T.D.C. [6].

Using newer fuels, such as biodiesel, can represent some disadvantages such as its higher viscosity in comparison to diesel, but can be compensated for by increasing the pressure in common rail injection systems. Nevertheless, using blends of alternative fuels can bring the best of both, or at least decrease the flaws and promote the combustion parameters [6].

In terms of emissions, Diesel engines produce higher levels of emissions in comparison to gasoline engines. This is because Diesel engines have unsteadied diffusion flames inherent to its combustion process. However, this unsteady behavior results in higher efficiency in comparison to gasoline engines. The emissions of the diesel engine are reduced by an aftertreatment system, which controls the NO_x generated by the combustion[7].

In Figure 2.2 it can be observed the overlap of different pressures at the crank angle at different cycles. There is some delay in the peak pressure, meaning that the combustion event is not always at the same crank angle nor the T.D.C. Still,

for analysis & design purposes it can be simplified to assume that the highest pressure happens at T.D.C.

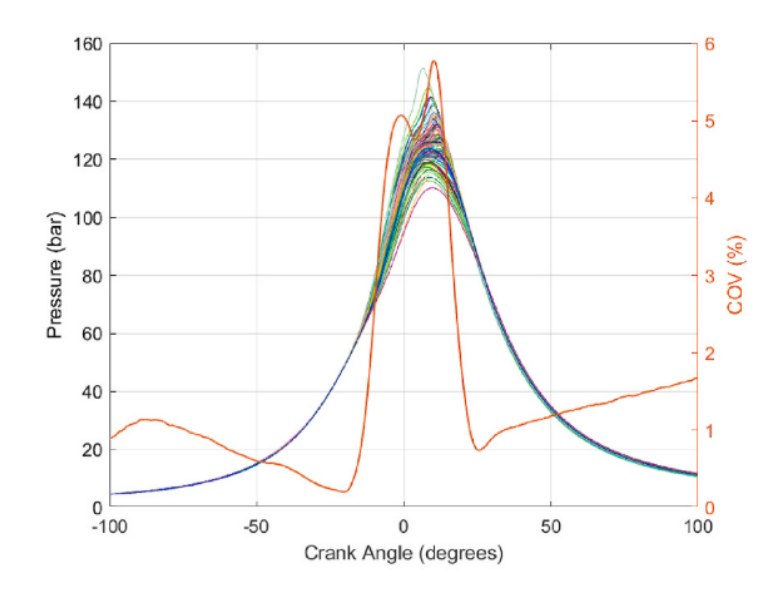


Figure 2.2 Crank angle vs Pressure with Coefficient of Variation percentage [5]

The output torque of an engine is a good indicator of its performance. It is defined as the force acting at a moment distance, with the units of N-m or lbf-ft. The point of maximum torque is called maximum brake torque speed. The relationship between power and torque for four stroke engine is given as follows in Equation 2.2:

$$W = (mep)A_p\bar{U}_p / 4$$
 Equation 2.2

Where:

际 mep = mean effective pressure

际 A_n = piston face area of all pistons

呀 $ar{U}_p$ = average piston speed

Power and torque, nonetheless, as key indicators of the engine performance are used as a reference point in improvement while changing other subsystems or variables in the engines. There is potential in using graphene oxide as an engine oil additive which in effect could return energy saving. Using nanosheets to the oil can improve the viscosity-temperature-shear rate characteristics reducing friction [8].

The current trend for engines is adding turbochargers, sample in Figure 2.3, with different arrangements and displacement geometries. This allows the engines to have less displacement volumes and have similar or higher power in comparison with atmospheric engines. When supercharging an engine the following can be obtained: Reduction in cooling loss ratio in relation to supplied heat. Maintain the NO_{χ} concentration, increasing the thermal efficiency. Adaptability, the superchargers can be used in gasoline, gas, diesel, and hydrogen fueled combustion engines [9].



Figure 2.3 Variable geometry turbocharger sample[10]

The operating range as has been described; it could be determined by the performance curve as shown in Figure 2.4. The operating range where the highest cylinder pressures could be inferred from the torque and the given speed of the crankshaft for later generate different load cases that imply the combustion forces and the inertial loads.

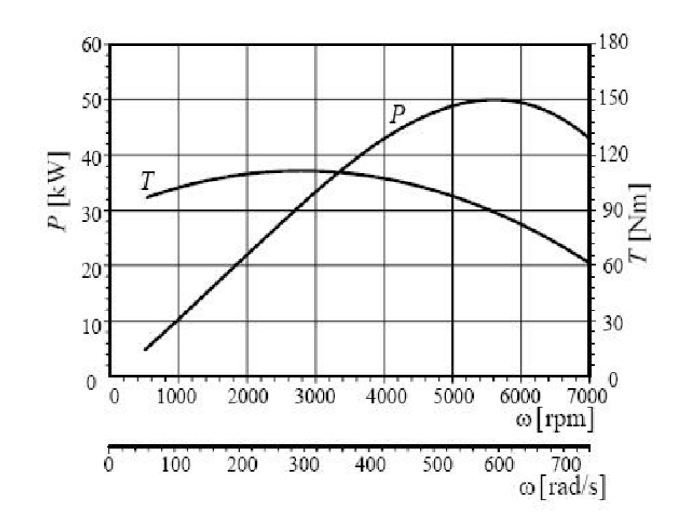


Figure 2.4 Engine performance curve sample [11]

The forces on the connecting rod due to the accelerations can be developed by rigid dynamics principles where no deformation is considered. Based on the crank slider mechanism, it can be noted that the lateral force on the connecting rod is when the crankshaft is perpendicular to it either 90° or 270° [11].

2.2 Main components

The main components to be described are the cylinder, piston, connecting rod, crankshaft, damper, and flywheel. The cylinder is basically a tube of circular cross section, closed with the cylinder head. The piston is a gas-tight component, which fits inside the cylinder and is attached to the connecting rod with a pin [12].

Other component descriptions can be observed in the following Figure 2.5. The marked components are the core of the engine. The crankshaft is the component that is driven by the combustion of the different cylinders, generating a torque output. While the cylinder liner is the component that brings the angular and lateral constraints for the piston and allows the vertical degree of freedom for the linear motion.

Other components highlighted in Figure 2.5 play a major role in the engine. For instance, the valves allow the passage of either fuel and air mixture, or the path for the exhaust gases due to the combustion. The front pulley and damper are a power output as well, plus the damper brings stability to the structure due to the excitation of the rotating components.

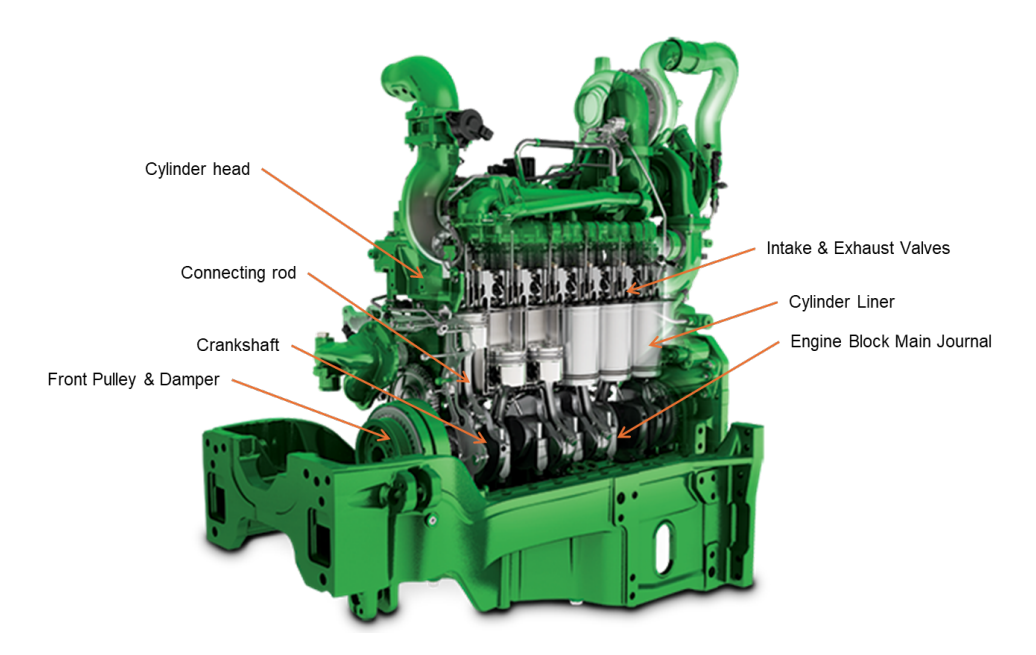


Figure 2.5 Diesel engine section view [13]

The cylinder head basically is the structure that holds up together the upper components such as the valves, turbo, and valve train structure among others. It plays a significant role in the combustion, cooling, and exhaust, providing the adequate passages for each of the fluids involved. The engine block at the end is a structural component for fitting all these assemblies and systems [14].

Lastly, on regard to the crank train, the flywheel is the component that provides inertia to the rotating motion, keeping the assembly rotating between the strokes [12]. In Figure 2.6 can be observed at the rear of the crankshaft, as well as the other crank train components.



Figure 2.6 Crank train components [15]

As mentioned previously, it can be concluded that there are Multiphysics involved in the study and development of an engine. Where the outputs measured in the industry in terms of torque and power, are heavily influenced by the different components that made up the setup of the engine. It can be noted that despite having the same principle in the last 100 years, the engine has evolved integrating more components that increase its efficiency and demonstrate that it could be adapted to the upcoming needs of the industry.

Chapter 3 Connecting rod fundamentals

Connecting rods are often considered as one of the critical components, since its failure leads to stopping the engine and hence the operation. The content to be shown is about the common nomenclature of the different components that integrate the subassembly of the connecting rod within the crank train.

The classical dynamics of the crank slider mechanism are part of the foundation of the loads to which the connecting rod will be subjected. The novelty of this study is to bring more information and sensitivity to the events that cause more damage during operation.

3.1 Connecting rod structure & manufacturing

Due to the relative velocity & acceleration between the members of a crank-slider mechanism, obeying the law of sines we can also confirm when doing calculation of the full revolution of the crankshaft; that there are higher lateral accelerations at the perpendicular angles between them.

However, the acceleration of the small end of the connecting rod, or the piston is quite different. Since it's only a translational displacement, having the peak acceleration at reaching the top dead center[16]. The calculations are going to be carried out with the relative-velocity and relative acceleration equations.

It is also considered the prime component between the crankshaft and piston, vastly used on the internal combustion engines. They are designed to withstand the previously mentioned forces, justifying the need for outstanding material properties, high tensile strength, hardness, and rigidity [17].

About the connecting rods for the study, all diesel engines have two-piece, H-section rods. Usually they are made from medium-carbon steel[18]. It can be described more thoroughly in the Figure 3.1. It can be noted as well that the upper bore is smaller than the lower bore of the connecting rod, they are also known as the big and small end.

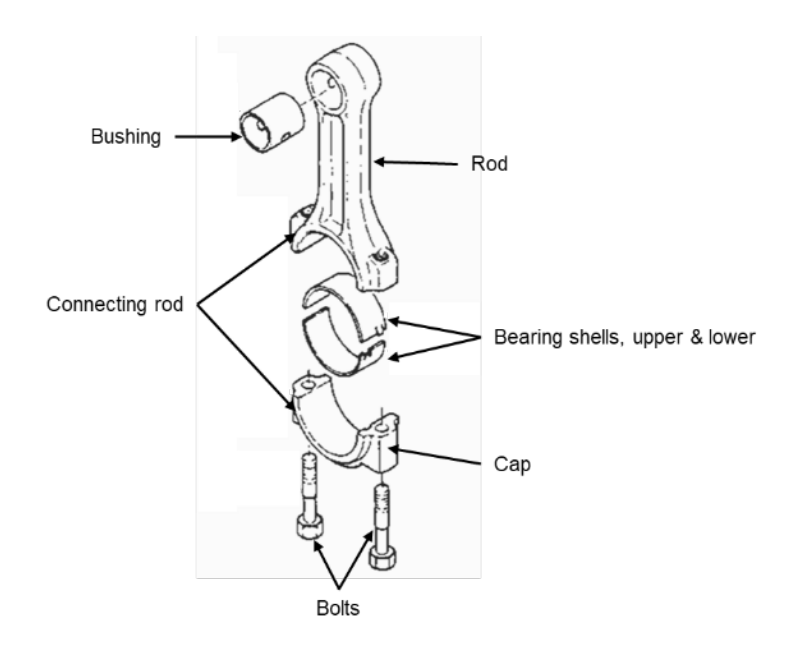


Figure 3.1 Connecting rod component description [18]

The manufacturing of connecting rods is based on forging processes. The cap and the rod are separated through a process called "fracture splitting". This is a processing technique which is very precise and has a relatively low cost for separating the forge. It has importance on the design for the manufacturing area since the notches for a successful separation must be specified properly [19]. A sample can be observed on Figure 3.2, note that the rod mating face has an irregular pattern, which will be a matching profile with the cap.



Figure 3.2 Fracture split connecting rod[21]

Forging in general terms is described as a manufacturing process where the metal is shaped by compressive forces. One of the main advantages is the high strength and durability for the finished component, required for the connecting rod as previously mentioned. The alignment of the grains in the microstructure is also an enabler for the increased strength, the reduction or internal voids and inclusions generating a more homogeneous material. Plus, high precision in dimension tolerance and good consistency for mass production [20].

3.2 Connecting rod dynamics

For the inertial load cases it will be performed a series of calculations as follows in the next sample. Based on Figure 3.3, it is needed to calculate the translational acceleration of the piston or small end and the angular acceleration of the connecting rod. The mass of the reciprocating mass can be given or measured to develop the inertial load cases.

In this case, the clockwise direction will be considered as positive. The characteristics depicted in Figure 3.3 will be described as follows and detailed with the rigid dynamics equations to determine the accelerations at a given crankshaft speed.

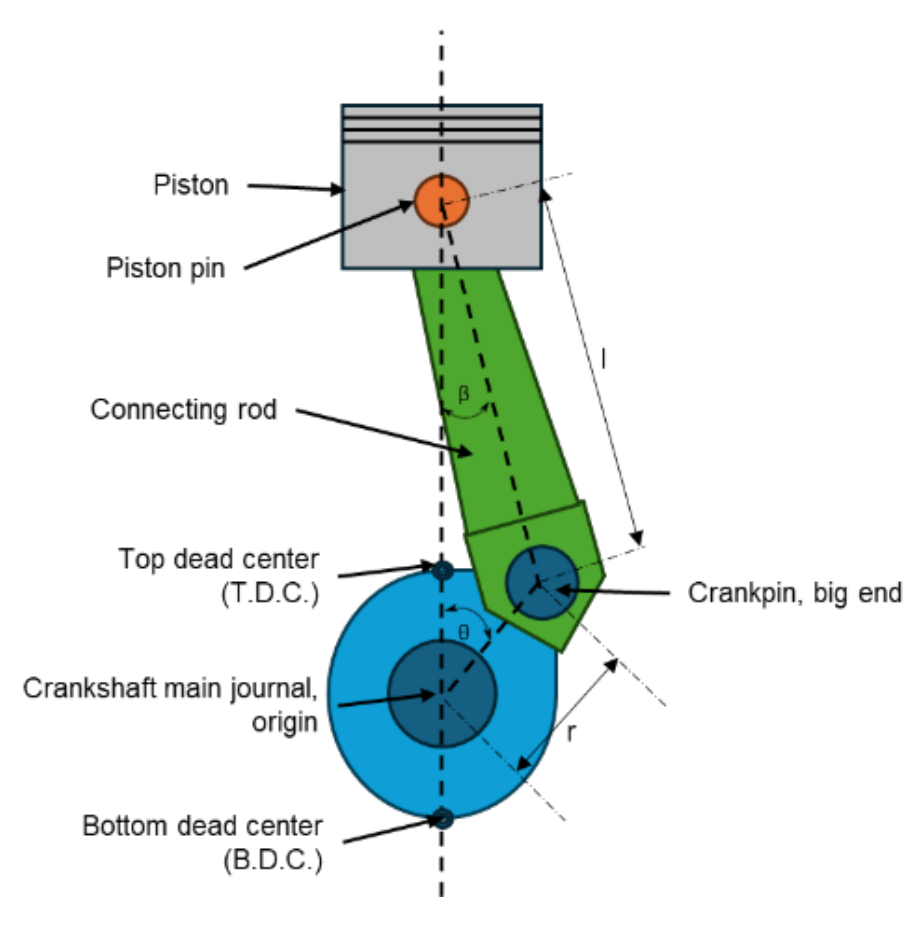


Figure 3.3 Connecting rod geometrical description

- 际 I = length of the connecting rod from big end to small end in meters.

- 际 β = resulting angle between the normal center line and the connecting rod center.
- 际 ω = rotational speed of the crankshaft in radians/seconds.

It is required to determine the velocities of the piston, connecting rod and crankshaft to later calculate the accelerations. For analysis purposes, a constant speed plus no deformation is assumed.

The velocity of the crankpin as a point to the small end (se) and the big end can be determined by using the crankpin (cp) as a reference point, to determine the velocity of the small end. The relative velocity is depicted in Equation 3.1. The crankpin velocity can be calculated by Equation 3.2. The resultant angle β is computed using the law of sines as shown in Equation 3.3.

$$V_{se} = V_{cp} + V_{se-cp}$$
 Equation 3.1
$$v_{cp} = r\omega$$
 Equation 3.2
$$\frac{l}{\sin \beta} = \frac{r}{\sin \theta}$$
 Equation 3.3

There is the need to determine the angle between V_{se} and V_{se-cp} and the resultant angle of the connecting rod and the crankshaft position.

Angle between $V_{se} \& V_{se-cp} = \alpha$ stated as Equation 3.4, while its complementary angle, γ , in Equation 3.5, using the complementary angle of θ .

$$\alpha = 90^{\circ} - \beta$$
 Equation 3.4

$$y = 180^{\circ} - 30^{\circ} - \alpha$$
 Equation 3.5

Using the law of sines, it can be now determined the velocities V_{se} and V_{se-cp} , in Equation 3.6 and Equation 3.7, respectively.

$$\frac{v_{se}}{\sin \gamma} = \frac{v_{cp}}{\sin \alpha}$$
 Equation 3.6
$$\frac{v_{se} - cp}{\sin 90^{\circ} - \theta} = \frac{v_{cp}}{\sin \alpha}$$
 Equation 3.7

Once the tangential velocities of the members have been determined, the angular velocities can be computed. As follows in the Equation 3.8. Note that the units of ω are radians/second, while v are meters/second.

$$\omega_{se-cp} = \frac{\upsilon_{se-cp}}{l}$$
 Equation 3.8

Now that the velocities can be determined for the components of the mechanism, the acceleration calculations can take place as shown in Equation 3.9.

$$a_{se} = a_{cp} + (a_{se-cp})_n + (a_{se-cp})_t$$
 Equation 3.9

The crankpin acceleration has only a normal component of acceleration, thus a_{se} can be calculated as shown in Equation 3.10. The normal acceleration of small end-crankpin can be obtained from Equation 3.11, since ω_{se-cp} has been previously computed.

$$a_{se} = r\omega^2$$
 Equation 3.10
$$(a_{se-cp})_n = l\omega_{se-cp}^2$$
 Equation 3.11

From a simultaneous isolation solution, it can be determined a_{se} and $+ (a_{se-cp})_{t'}$ as it is being depicted in the Equation 3.12 and Equation 3.13, respectively. These computed magnitudes will be on $\frac{meters}{second^{2'}}$ the angular acceleration of $(a_{se-cp})_{t}$ can be computed using Equation 3.14.

$$a_{se} = a_{cp} \cos \theta + (a_{se-cp})_n \cos \beta - (a_{se-cp})_t \sin \beta$$
 Equation 3.12

$$0 = a_{cp} \sin \theta - (a_{se-cp})_n \sin \beta - (a_{se-cp})_t \cos \beta$$
 Equation 3.13

$$\alpha = (a_{se-cp})_t / r$$
 Equation 3.14

Applying the formulae previously mentioned, accelerations can be obtained to be used on the finite element models. The ruling equations for the accelerations show

that the highest angular accelerations are when the angle values are at 90° and 270° as seen in the Figure 3.4.

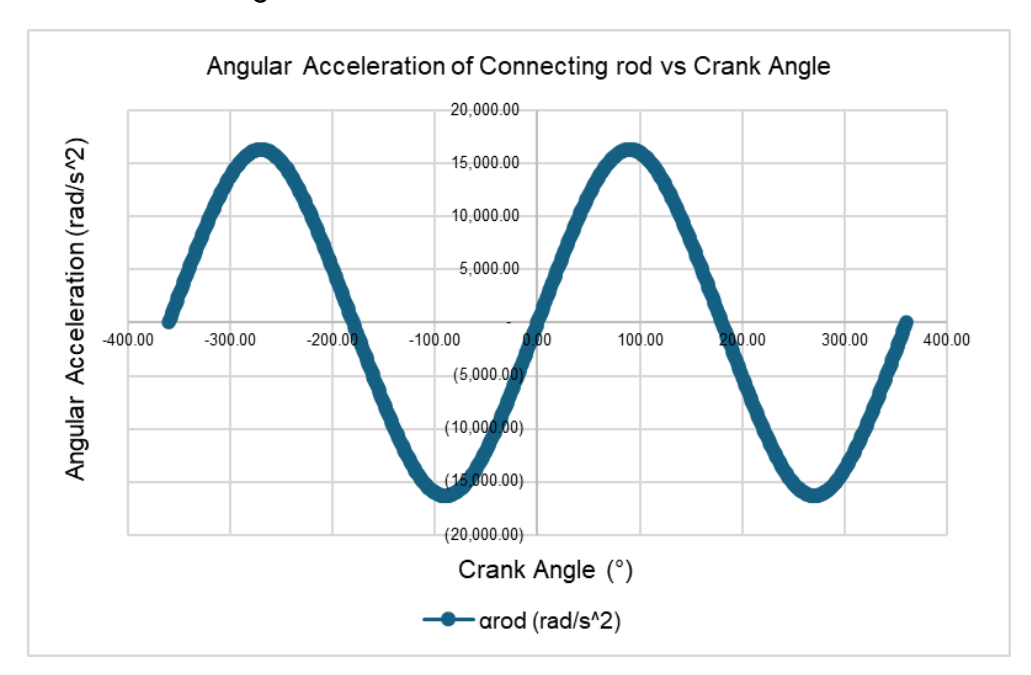


Figure 3.4 Angular acceleration of a connecting rod vs crank angle.

In contrast, the small end's highest translational acceleration is at the 0° shown in Figure 3.5.

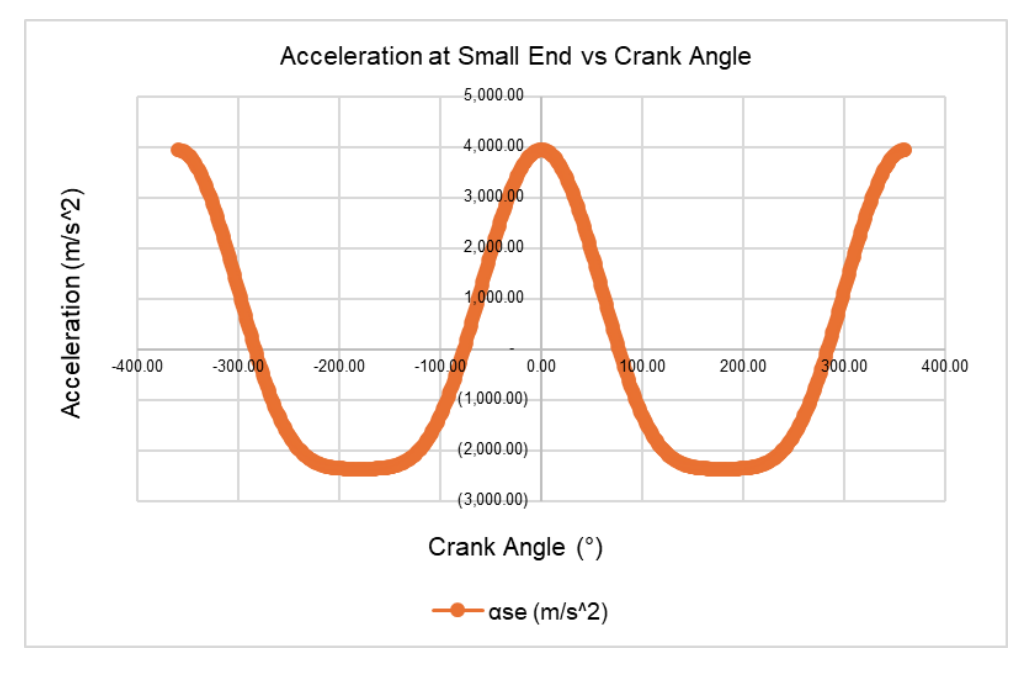


Figure 3.5 Translational acceleration of the small end vs crank angle.

Thus, the angular accelerations can be directly applied within the FE model, and the pull force can be computed by following Equation 3.15, using the reciprocating mass and the translational acceleration at the small end.

$$F = m_r a$$
 Equation 3.15

Where:

际 F = Force in Newtons (N)

际 m_r = Reciprocating mass (kilograms)

际 a_{se} = translational acceleration ($\frac{meters}{second^2}$)

With the previous accelerations the inertial load cases can be applied adjusting to the desired study speed, as well as the pull load. For the firing load, it can be obtained by using the cylinder pressures at each given torque/speed parameter from Equation 3.16.

$$F_{\sigma} = PA$$
 Equation 3.16

Where:

际 F_{σ} = Force in Newtons (N)

际 P = Pressure in Megapascals (MPa)

际 A = Area of the cylinder bore in square millimeters (mm^2)

3.3 Connecting rod's bolted joint

The cap and rod are joint through bolt pairs usually. Interface between cap and rod depends on each manufacturer's design. This interface can be done by a fracture split, which creates a rugged interface with valleys and crests across the faces but making a perfect fit. Even so, this rugged interface prevents lateral sliding, securing the joint.

In theory, all threads engaged in the bolt should share the load, but the inaccuracies in the profile and spacing cause that most of the load to be carried by the first few threads. The common failure modes for the bolts are by fatigue, yielding and wear [22].

Recent studies show that the empirical formulas used for design have a good correlation with the finite element analysis. The expected results from the bolt performance have an average difference of 0.76% [23].

3.4 Bearing crush

The bearing crush is not literally on the connecting rod's bearings, it is referred to the quantitative measure of the crush of the excess length of the exterior circumference of the bearing over half the interior circumference of the connecting rod. When assembled the parting lines are reduced to zero. The back pressure usually is around 5.5 to 8.24 MPa. Once they are disassembled, they tend to spring back, having no real crush [10].

The crush can be defined by the following three items, the housing bore tolerance crush, the checking load crush, and the engineering crush. The housing bore tolerance is defined by the Equation 3.17. After some load application to the bore gauge, the bearings obey Hooke's law.

$$B_c = 0.5\pi (D_2 - D_1)$$
 Equation 3.17

The initial behavior of the bearings is nonlinear corresponding to the checking load. This load is intended to fit the bearing properly in the housing. Each manufacturer determines the method and the crush height accordingly [10]. A schematic of the crush can be observed in the Figure 3.6.

Where:

际 B_c = Bearing crush, mm.

际 D_1 = Lower limit of the bore diameter, mm.

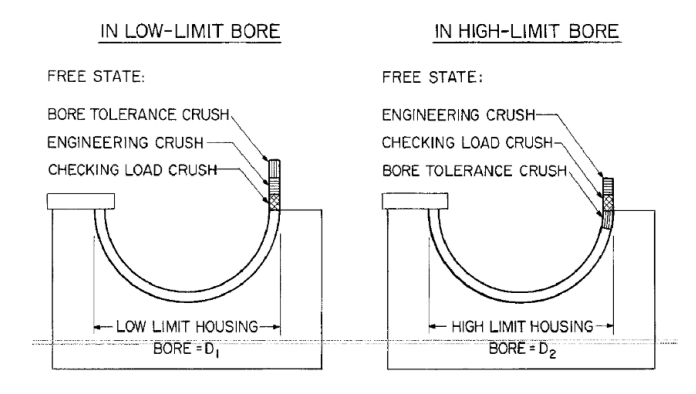


Figure 3.6 Bearing crush on inspection gauge [10].

This type of bearing is named hydrodynamic since they act with an oil film between the shaft and the inner surface. The intention of the crush is also to fix the bearing against its corresponding housing; to avoid slippage it is designed with some features that prevent the rotation.

A common failure mode is the oil starvation which ends in temperature rise and can get to the melting point, also the eccentricity caused by the assembly can lead to a not desired oil profile. These are some of the aspects that are relevant to bearing selection and design, but the major effect on the connecting rod is the assembly compressive stress [10].

The location and size of the oil supply holes play a major role in avoiding excessive wear and reducing friction losses. In the following Figure 3.7, it can be observed different oil supply holes concepts. The oil supply in excess can also lead to problems when an additional oil gallery is added, resulting in additional wear for the bearings on the small end [24].

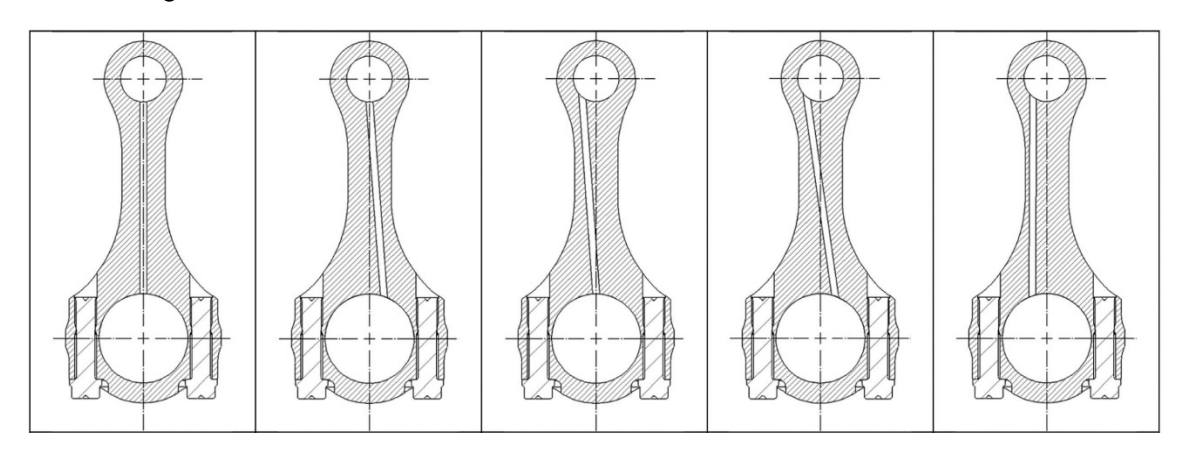


Figure 3.7 Oil hole concepts on connecting rod [24].

It is not easy to replace the bearings either on the crankshaft or the connecting rod, because the engine must be dismounted to be repaired. The bearing failures usually are attributable to melting due to high friction in the absence of lubrication. Hence the relevance of the oil supply and quality.

3.5 Body interactions within the connecting rod

The friction coefficients and state of contact depend on the manufacturing condition and afterwards with the engine operation. A description of these different states will be described as follows:

际 Bushing to rod.

This interface contact is constrained during assembly and generated by press fit. The typical friction for a bronze to steel interface is 0.2 - 0.5. A conservative approach would be using 0.2, to detect a sliding failure mode if given [25].

际 Bushing to piston pin.

The interface contact during engine operation is lubricated by a spray pointing at the joint. The friction coefficient (COF) is ~ 0.07 -0.12. For a higher acceleration transfer and force, it will be taken the lower value [26].

际 Rod to cap.

Due to the connecting rod manufacturing process, the cap and rod are separated through a fracture process. This means that the interfaces have a rough asperity surface but perfectly match each other. The tangential movement is not possible and in different internal testing have been shown that the bolt would be broken prior to separation. This shows a friction coefficient higher than 0.74 [25].

际 Bearing to rod, bearing to cap, bearing to bearing.

The friction coefficient of the rod and cap to the bearings is ruled by the coating type of the bearing, usually an alloy including Si, Cu, Ti, and C. This is a static condition due to the assembly and can be taken as 0.23 [25].

际 Bearings to crankshaft.

It is worth noting that this type of bearing has a very low friction coefficient, due to the high presence of fluid films between the interfaces. The coefficient values can round as low as 10^{-6} or 10^{-7} .[27] It can be considered as frictionless, however for design purposes it has been also taken as 0.001[26].

际 Bolt to connecting rod.

The bolts used in this type of connection have a specific coating that must comply with the specifications on print by supplier. The COF may vary from 0.12 up to 0.19 accordingly.

3.6 Study approaches

The use of static analysis with loads generated from MBS as shown in Figure 3.8, with flexible bodies have shown good correlation in large engines. The usage of analysis tools, such as AVL's Excite PU, can provide the dynamic loads to use in static analyses. Nevertheless, these methods are usually linear models that do not take into consideration the non-linearities implied in these physics, such as frictional interfaces and change in stiffness due to loading or material conditions [3].



Figure 3.8 Flexible multibody simulation[3].

In the model from Göös [3], manufacturing conditions are not considered. However, incorporating these factors could improve the fidelity of the simulation, though it would also increase its complexity. Bore distortion due to assembly conditions is not reflected, but it could be addressed along with failure modes caused by bearing deformation.

Weight reduction and optimization of the connecting rod has been addressed several times. Testing of different I-Beam sections has shown consistent results but highlights the relevance of the microstructure given through the connecting

rod. For instance, there is no consistent homogeneity between the I-beam section and the larger bore of the connecting rod yet must be addressed through temperature control in the manufacturing process [28].

Modal analysis to determine the resonant response of the component has also been conducted to determine the stiffness of the component. Other advantages of this type of study include the awareness of the mode in which the component can resonate and generate damage to itself and surrounding components [17].

In Figure 3.9, it can be observed the different mode shapes can study carried out by Kuldeep B, et al [29], which shows different mode shapes that could affect the surrounding components of the connecting rod, plus the resonant mode shape at given frequencies.

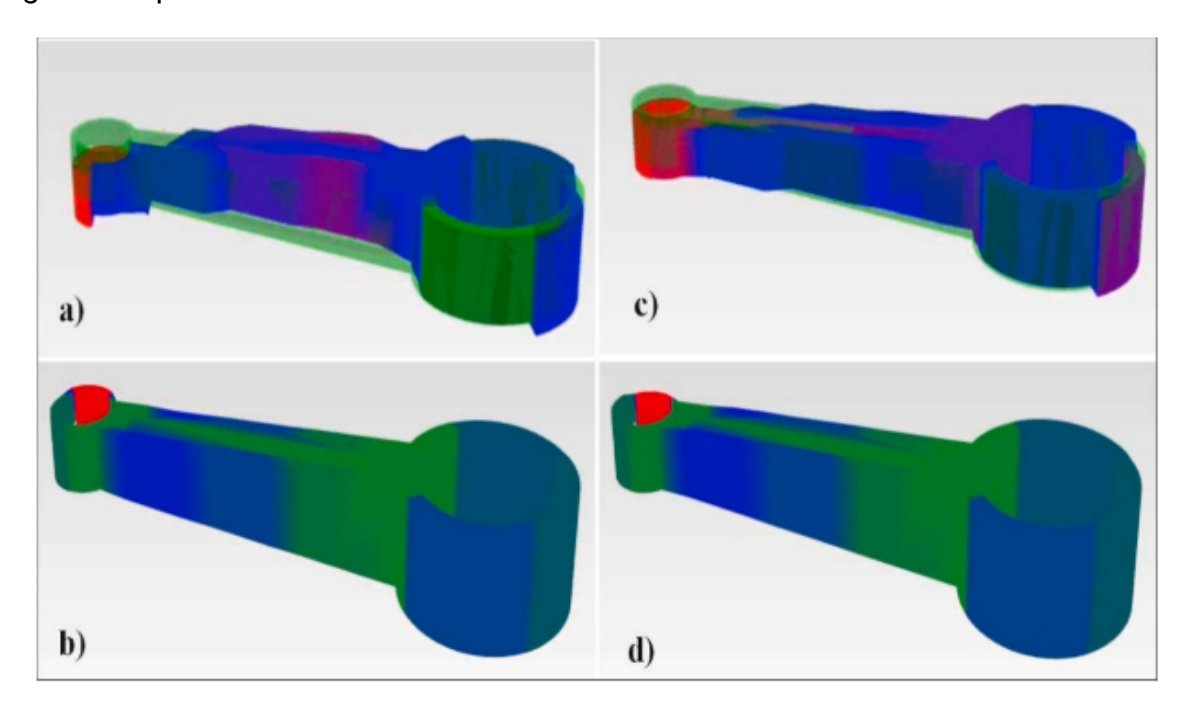


Figure 3.9 Modal analysis mode shapes of connecting rod [17].

As discussed, the load cases that have a deep influence are heavily influenced by the dynamics involved at the different speeds of the crankshaft. Secondly, the gas forces and the counteracting inertias of the reciprocating mass. The body interactions between the different components also play a significant role and the improper function can lead to different failure modes. Studies shown involving EHD loads have shown that they can be higher in comparison to classical rigid dynamics.

Chapter 4 Fatigue analysis & testing

Fatigue analysis in high cycle fatigue regimes has relied on foundational theories developed during the 1800s. While these classical models provide a general understanding of material endurance, modern advancements have revealed that diverse influencing factors e.g. surface finish, material homogeneity, and residual stress can significantly increase or decrease component longevity. The complexity of current applications requires a more detailed approach for fatigue prediction, as the interaction between material properties and external conditions often leads to unexpected variations in performance.

Despite achieving safety factors for high cycle fatigue may seem straightforward, the real challenge appears in designing components that operate under low stress targets without affecting the reliability. Designers must find a balance between optimizing durability and minimizing stress concentrations, ensuring that even minor design modifications do not drastically reduce fatigue resistance. As industries push for lighter, more efficient structures, refining fatigue assessment methodologies becomes increasingly critical to maintaining long-term structural integrity.

4.1 Fatigue life

Fatigue life is the available useful life for a given fatigue analysis. It can be set to a full model, parts, surfaces, edges, and vertices. Due to constant amplitude loading, there can be a given number of cycles until the study component fails due to fatigue. When non-constant loading is given, there could be a representation of loading blocks until the failure is present [30].

Despite new efforts, comparison between fatigue testing and prediction efforts, the high cycle fatigue (HCF) study has not advanced that much compared to the first studies of the 1800s. The connecting rod in this case, as similar as rotating components, experience HCF.

High cycle fatigue can be defined as a fatigue condition where the number of cycles between possible inspections is too large, while the stress or strain behavior prevails on the elastic region.

While low cycle fatigue (LCF) is basically controlled by elastic and cyclic plasticity behaviors. HCF usually involves high frequencies (cycles per second), low amplitudes, elastic cyclic behavior and more than one million cycles [31].

A common diagram to determine the fatigue life of a component of a certain material, can be studied using the S-N curve which is a plot of maximum stress as a function of cycles to failure. The S-N diagram that can be observed in the Figure 4.1 is constructed with a constant value of stress ratio, R.

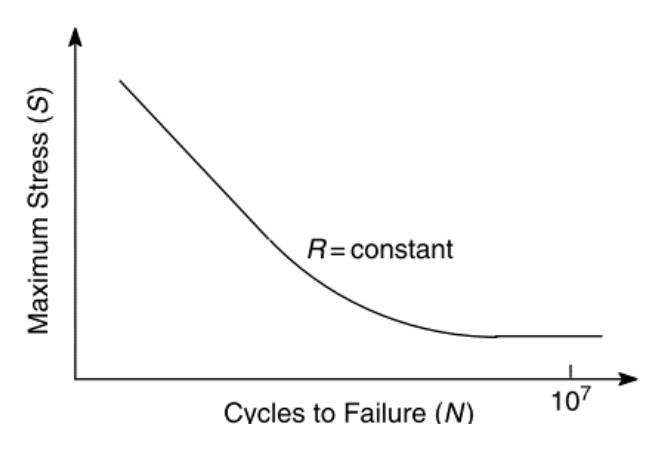


Figure 4.1 Typical S-N Curve[31]

The connecting rod, among other components in the engine does not have a scheduled maintenance, additionally it completes more than one million cycles within the first running engine hours. Therefore, a HCF approach is to be used, and implies no damage as well within the design life target [31].

The damage in fatigue terms can be defined as the design life/available life. The design life can be set manually based on the expected durability of the usefulness of the component. Values above 1 indicate a failure before the design life is reached [30].

There is also the well-known adoption of Miner's rule, which conceptualizes the loading history effects of cyclic loading to the available life of a component. This rule has been used to estimate the cumulative fatigue damage of metals using the linear accumulation approach. It is expressed as shown in the Equation 4.1 [32].

$$f_D = \sum_{i=1}^k \frac{n_i(\sigma_i^{ampl})}{N_i(\sigma_i^{ampl})}$$
 Equation 4.1

Here f_D refers to the total damage that can be set as one for the design purpose, while N_i is the number of cycles to failure when subjected to constant amplitude (σ_i^{ampl}). Depending on n_i the number of the applied load cycles under the same

load amplitude. In summary, when $f_D \le 1$ the component will not have a fatigue failure [32].

A fatigue safety factor is defined as the factor of safety with respect to a fatigue failure at a given design life. A value less than one indicates a failure before the design life is reached [30].

The failure of the component is basically defined by the loss of the functionality. In this case, it can be caused by a crack and afterwards a fracture. The crack initiation is mostly affected by the height of the fracture plane. While the fatigue life is affected by the surface roughness and hardening index [33].

In some commercial fatigue calculation software, there is a surface finish factor that will make a correction to the expected fatigue life and safety factor. The surface finish (Ra) is a key parameter that should be controlled during the manufacturing process [34].

Depending on its finish and the materials ultimate tensile strength (UTS), it can be obtained from the following Figure 4.2. The impact of the surface finish is due to the microscopic cracks that might lead to a crack initiation.

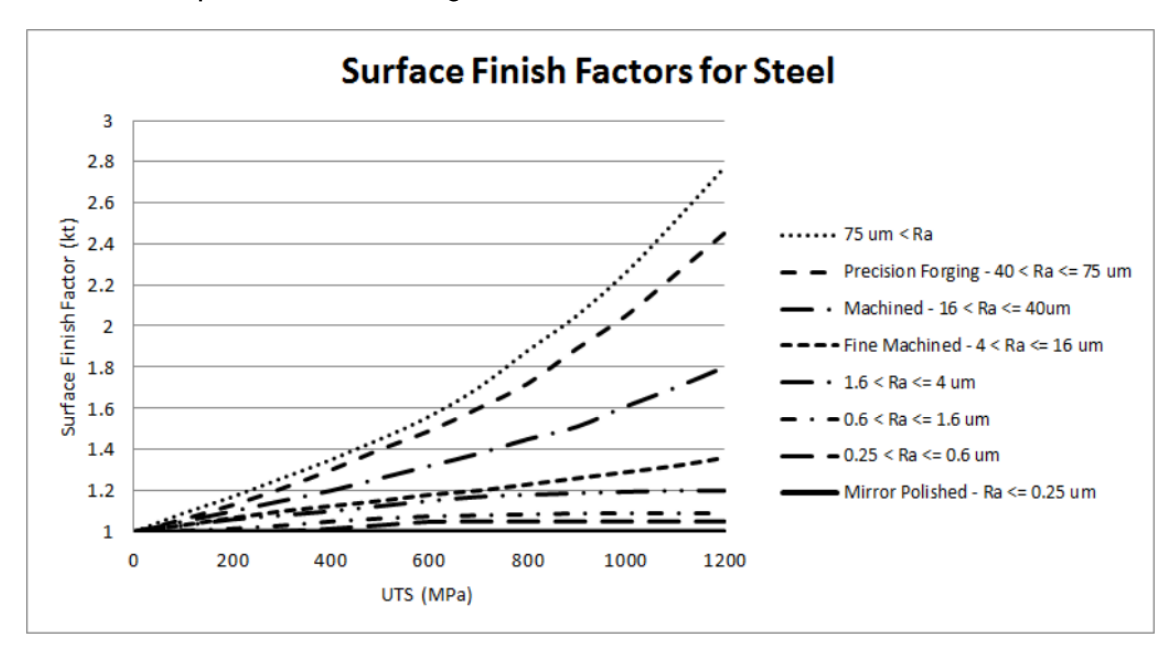


Figure 4.2 Stress concentration factor based on Ra, Kt vs UTS [35].

The surface finish factor as previously presented depends heavily on the production process used for the component. It could be different on each face,

since there are processes that are locational and others that might be specific for different points.

On Figure 4.3, shows the different average values according to the method being used for the manufacturing. At the end, the final surface finish will be dependent on the instrumentation and conditions, for instance the profile of the tool, the usage of lubes, among other factors [34].

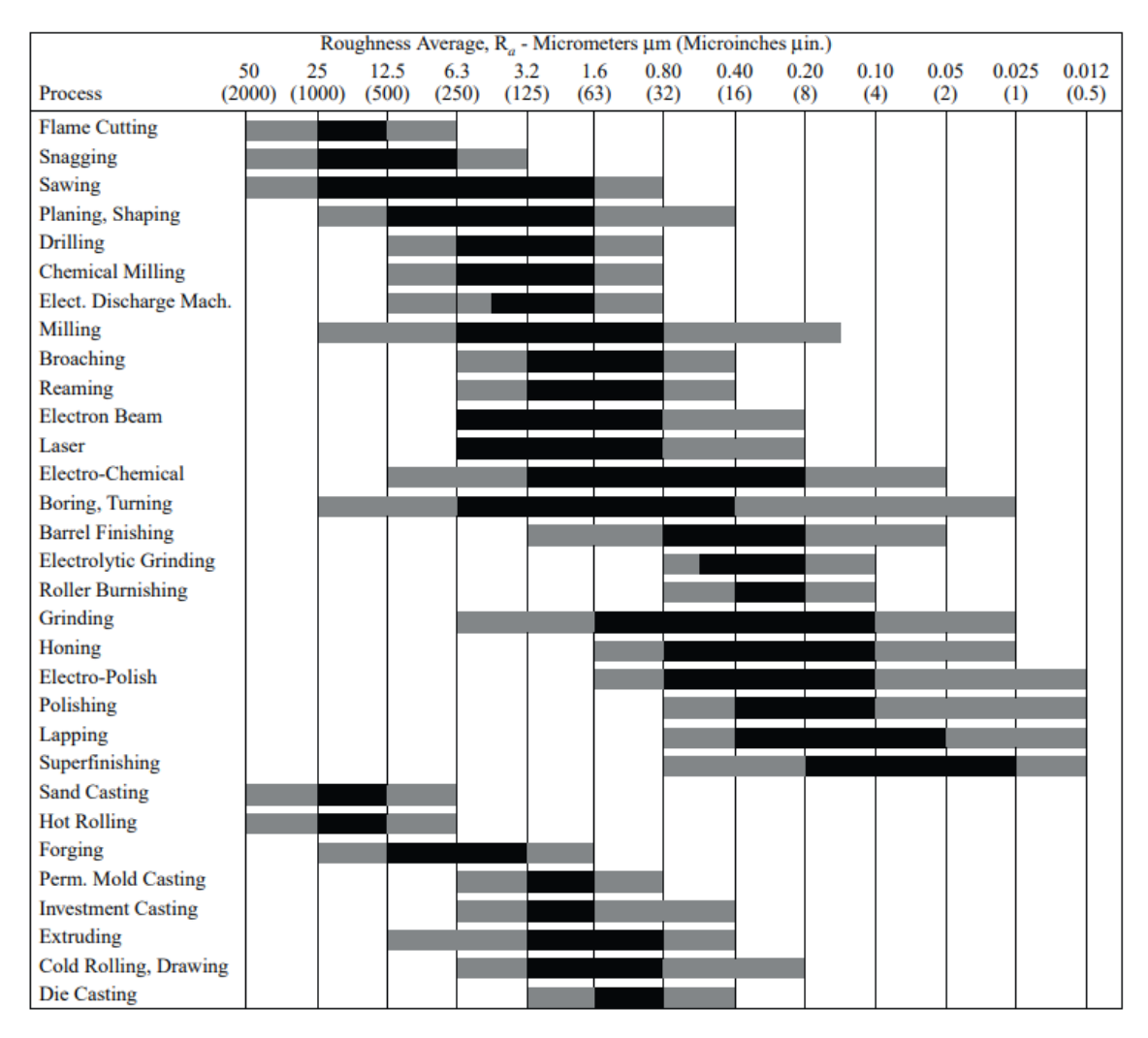


Figure 4.3 Surface roughness produced by common production methods [34].

4.2 Connecting rod testing

The connecting rod testing is carried out by assessing the loads generated by the combustion and the reciprocating motion of the piston due to the rotary motion of the crank. These results in an alternating load between compression and tension load cases [36]. A sample testbench is shown in Figure 4.4.



Figure 4.4 Connecting rod fatigue test bench[36].

There are laboratories that offer testing capabilities and machinery that have characterized the strength of the component. The test rigs replicate the operational environment for the rod, under compression, temperature, and oil supply. They are available for different force capacities in the range from 5 to 2,000 kN [37]. On Figure 4.5, it can be observed the different types of test bench offered by one supplier.



Figure 4.5 Test rig sizes by Sincotec [37].

From this chapter, it can be noted that the relationship between surface roughness, material properties, and design plays a critical role in determining a component's ability to endure high cycle fatigue. Surface roughness affects stress concentration, where irregularities can be the initiation points for fatigue cracks, ultimately reducing the corresponding endurance limit. Material properties, including homogeneity, strength, and microstructure, dictate how a component responds to cyclic loading among other peak events that cause damage, which at the end is cumulative and ends in a failure.

Achieving a design that consistently operates below the endurance limit requires balancing surface finish, proper material selection, and stress distribution considerations. By refining the design to minimize localized stress concentrations and selecting materials with adequate fatigue characteristics, engineers can enhance durability and extend component utility. Fatigue testing remains essential in validating these efforts, offering empirical insights into component behavior under cyclic loads and ensuring that theoretical predictions align with real-world performance. Through a combination of precise design changes and conscious fatigue analysis, components can be optimized for the desired utility and reliability in demanding applications.

Chapter 5 Design of experiments

The design of experiments is a strong statistical methodology that enables to systematically plan and analyze experiments. The methodology thrives on ensuring objective and data driven conclusions for taking decisions. This chapter will cover the usage of different methods that can bring different effects and variables together and get an answer on how they interact within.

The usage of the method can significantly improve the efficiency of the experiments and the corresponding budget. Since with different numerical methods it can describe the behavior of the factors selected, with its corresponding ranges that can later be translated to tolerances among other more tangible metrics.

5.1 Methodology of the design of experiments

Design of experiments (DoE) is a branch of the statistics that plays a key role in the planning, collection, and analysis of data to provide valid and objective conclusions for critical decision making. The DoE portrays the effect of the independent controlled variables or factors that create an effect during a process, method, etc.[38], [39].

The DoE is built by different concepts of randomization, block creation, replication, factorial approach, and the analysis of variance. The common applications within engineering are comparatives, screening, modelling, optimization among other applications [38]. The methodology to be applied list as follows:

- 1. Definition of the problem and objectives of the experiment.
- 2. Selection of responses, factors and levels for the study.
- 3. List of factors, levels, replications, blocks, randomization and model considerations.
- 4. Run the experiments according to the selection criteria.
- 5. Collection of the experimental data.
- 6. Computing of the data using a statistical method, ANOVA and graphical analysis techniques.
- 7. Evaluation of the model and relationship between factors and response (inputs and outputs). The conclusions of the study.

A graphical overview of the process can be observed in Figure 5.1. It's worth mentioning that these factorial designs can facilitate the identification of the impact of different variables to a response [39].

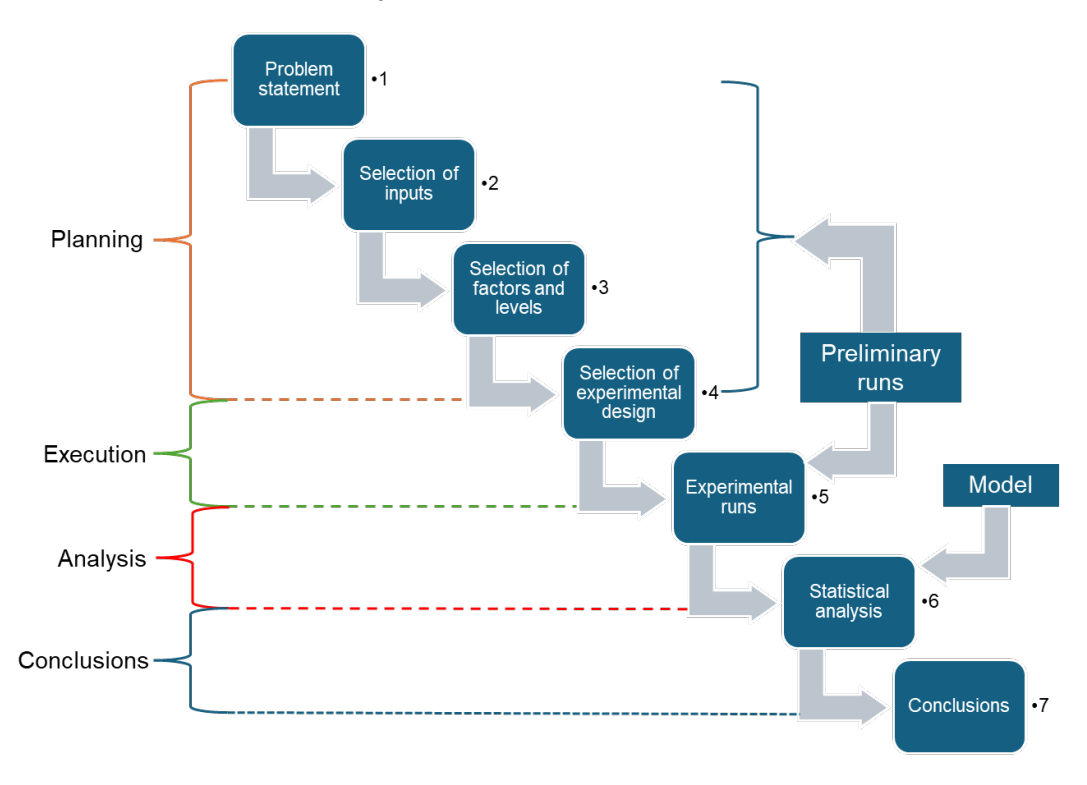


Figure 5.1 Design of experiments process overview.

There is also the possibility of interpretation of the results through the "cube" plot. Which could highlight the magnitude of the effect at each corner of the cube as it can be observed in Figure 5.2 [39].

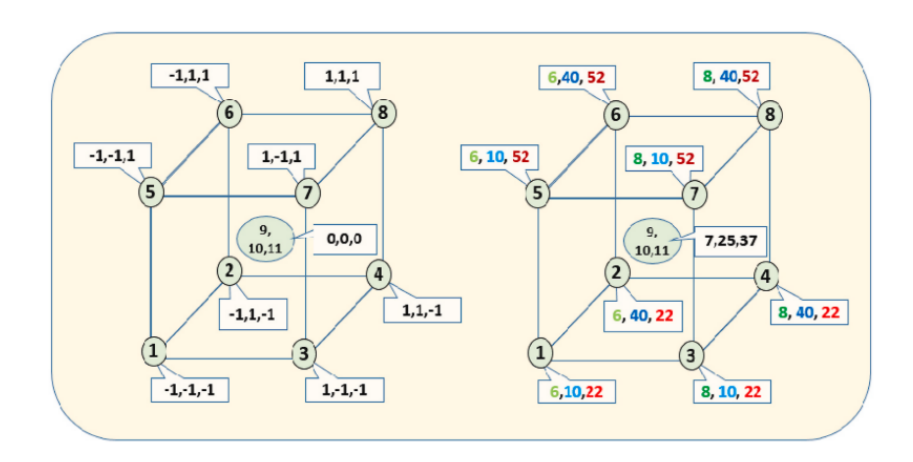


Figure 5.2 Cube plot sample[39].

5.1.1 Designs' summary

Full factorial designs involve the testing of all possible combinations of two or more factors and their respective levels. While the testing of only a set of the full factorial is named fractional factorial design. The number of experiments, N, for a full factorial is given by the Equation 5.1.

$$N = L^k$$
 Equation 5.1

Where L is the number of levels and k is the number of factors. The difference for conducting a fractional factorial is in its exponent, observed in the Equation 5.2, where p is the cofounding pattern of the design.

$$N = L^{k-p}$$
 Equation 5.2

Using full factorials can be time consuming and can become relatively large when values for L or k are >3 or >5, respectively. This method is mostly employed for screening, where a quadratic behavior between the response and factors is expected[38].

5.1.2 Screening

In this context, the screening is the procedure of identifying the most influential factors among the set of potential factors that affect the response. This allows to discard the least influential factors and focus the investigation on the remaining. These experiments usually involve many factors, often more than four with more than two levels [38].

There are some screening designs, as mentioned the factorial fractional design, Taguchi design and Plackett-Burnam, known in the common practice. The following Figure 5.3 shows the outcomes in the cube plots[40].

In brief there is the following relevance notes for the screening methods[40]:

- 际 Fractional factorial design (FFD)[40]
 - Considered as a low-resolution method.
 - Screens between three and seven factors
 - Commonly uses two levels to establish linear relationship between the points, +1 and -1.

际 Taguchi design[40]

- o Provides sensitivity testing, robustness analysis, aside from screening.
- Employs orthogonal arrays to generate objective functions to assess the influence factor on the response.
- o Suits well between three and seven factors
- o As well as FFD, it uses two levels.

际 Plackett-Burman[40]

- Design recommended for experiments with a high number of factors (9 to 11).
- A low-resolution design requiring two levels for each factor.
- o It generates a limited number of runs to efficiently identify the most influential factors.

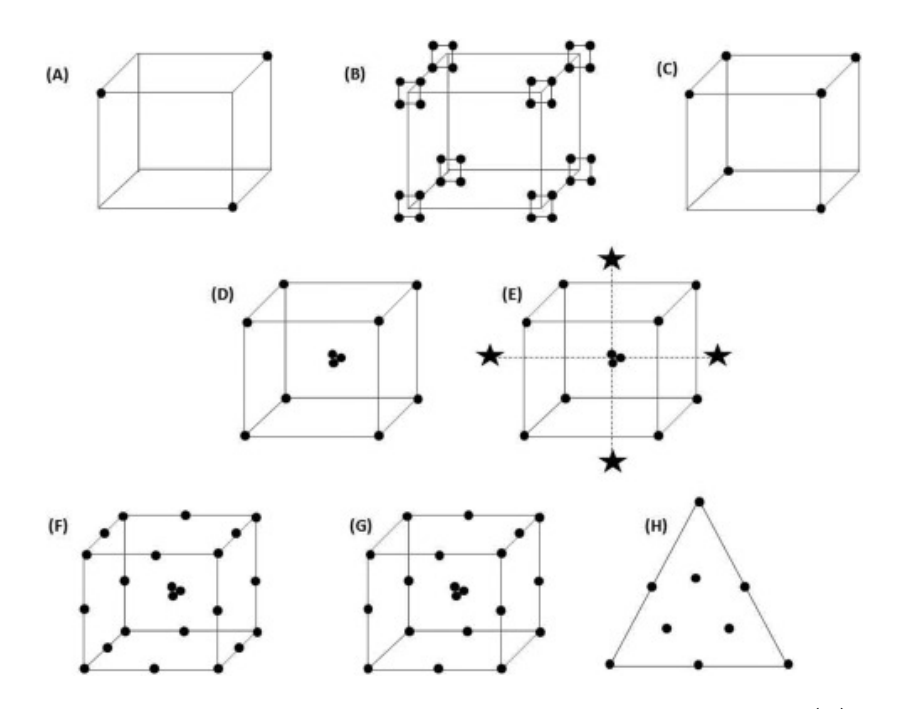


Figure 5.3 graphical depiction of various experimental designs: (A) fractional factorial design, (B) Taguchi design, (C) Plackett-Burman design, (D) full factorial design, (E) central composite design, (F) Box-Behnken design, (G) optimal design, and (H) mixture design [40].

5.1.3 Optimal designs

Optimal designs are an umbrella term for designs that are created based on certain specific objectives with optimality criteria. They are run via computational

algorithms and named computer-generated designs. The types of optimal designs list as follows [38]:

- 际 D-Optimal: Determinant optimal, it minimizes the variance of the regression coefficients of specific models.
- 际 G-Optimal: Global optimal, in this design the model is fitted from the experimental data, minimizes the maximum variance prediction over the design space.
- 际 I-Optimal: Integrated optimal, this design has the smallest average prediction variance.
- 际 A-Optimal: Average design, the design minimizes the average variances of the regression coefficients.
- 际 V-Optimal: Global optimal, aims to minimize the maximum prediction variance over a specified region of interest.

5.2 Factorial design of experiments in Minitab

There are different factorial designs available within the Minitab® software as observed in Figure 5.4. Depending on the complexity and resources available with various levels of resolution and related to the number of factors and runs, is the resolution given.

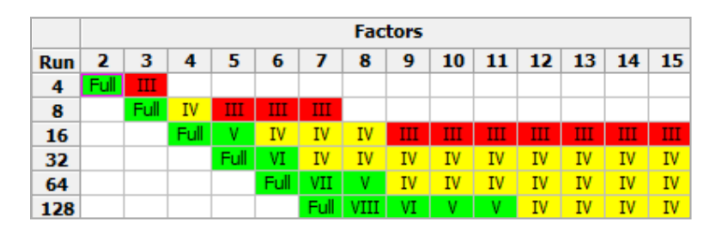


Figure 5.4 Available factorial designs[42].

The full factorial design of experiments will imply having all the different combinations performed. By having different resolutions, it might be achieved the same result as a full factorial, but the accuracy of the predictions might not be high. The higher the resolution, the less restrictive the assumptions required for the interactions[41]. Further differences can be observed in Table 5-1.

Table 5-1 Resolution differences.

	Resolution: III	Resolution: IV	Resolution: V
Main effects are aliased with any other main effect.	No	No	No
Main effects are aliased with two-factor interactions.	Yes	No	No
Two-factor interactions are aliased with each other.	Yes	Yes	No
Two-factor interactions are aliased with three-factor interactions.	No	No	Yes

To accomplish a simpler method and control of the experiment, when two or more effects have a property, they are called aliases[41]. The use of them is to establish a defining relationship between the effects and as well the factors. De aliases are determined as shown in Equation 5.3. Multiplying the effect by the defining relation yields the alias for that effect. In Minitab® it simplifies the aliasing by automatically setting them based on the factors given.

$$A \cdot I = A \cdot ABC = A^2BC$$
 Equation 5.3

When performing the factorial DoE, it is common to specify the plus and minus signs to indicate the high and low values of each of the factors involved. On the table they are aliased from the previous step already. The table allows to visualize the different set of combinations that are going to take place for the runs. Another of the advantages of performing the factorial experiment is that it contemplates the resources to get statistical information of the results to be obtained[41].

An analysis of variance (ANOVA) is a procedure that determines if there are differences between the means of a group in a sample, and if these differences exist due to randomness or have a specific root cause [43].

The coefficient of determination or of multiple determination, R^2 , is a measure of the amount of reduction in the variability obtained by the regression variables in the DoE[41].

The sum of squares is a measure of a general variability of the data, while an adjusted sum of squares considers the variability of an effect. The mean squares of a model works as an estimator of the data, whilst the adjusted mean squares have the estimator for a particular effect [41].

The F-Value in an ANOVA will tell if a group of variables together will have a significant effect. It is basically calculated by dividing the variance within the groups.

To accomplish a hypothesis testing, there is the use of P-Values. This value indicates the probability that the test statistics will take on a magnitude that is at least as off as the observed of the statistic when the null hypothesis is true. It can be defined as the smallest level of significance that can lead to the rejection of the null hypothesis[41].

Part of the DoE includes a Pareto Chart, which is a method to graphically display the factors that have the highest effect. It is characterized by sorting the relevance of the effects for the analyst to identify the significant drivers from the less influential ones. A sample of a Pareto chart, which obeys the 80-20 rule is displayed in Figure 5.5. This rule states that 20% of the causes lead to the 80% of the results [44].

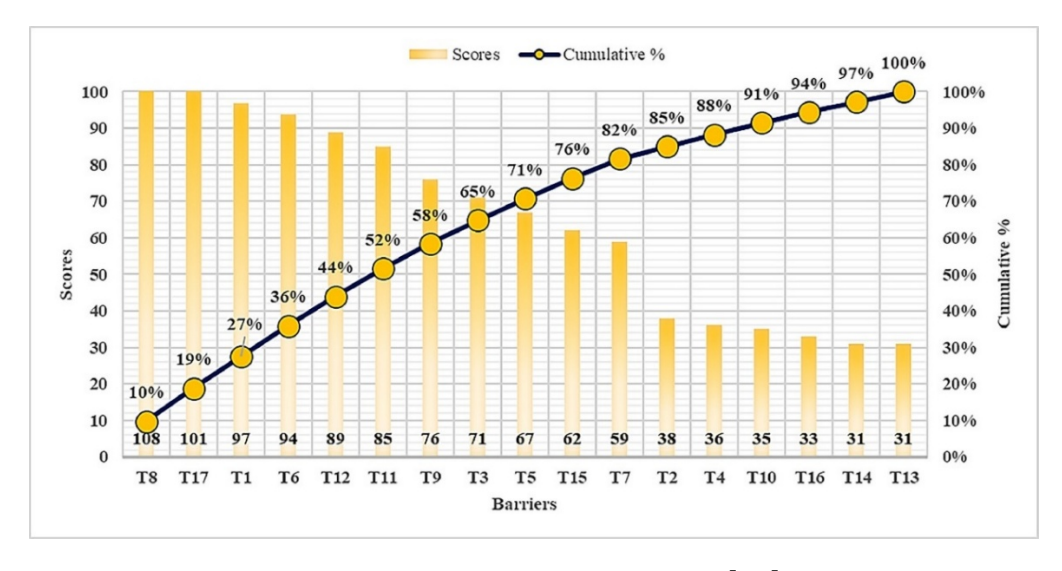


Figure 5.5 Pareto chart sample[44]

A main effect is the difference in the mean response between two levels of a factor. It can be plotted and graphically show the comparative relationship between the mean for all the runs in the DoE[42]. The interaction plot on the other hand shows the impact of the factors with the corresponding response [42].

Selecting the appropriate Design of Experiments (DoE) methodology is relevant in obtaining accurate and meaningful results. In particular when considering the resolution level of the experiment. The resolution level determines the degree to which factor interactions can be distinguished from one another, directly influencing the quality and reliability of the insights gathered. Higher resolution designs enable precise detection of complex relationships but demanding more resources, while lower resolution designs require less effort at the cost of the accuracy.

By carefully choosing the most suitable DoE framework, taking into account factors such as blocking, replication, and factorial structure it can optimize experiments to yield robust conclusions. A structured experimental design enhances efficiency and reduces unnecessary trials. It also strengthens the reliability of predictions and decision-making processes. Finally, the proper selection of a DoE contributes to improved process optimization, cost reduction, and innovation across various engineering and scientific applications.

Chapter 6 Finite element modelling & simulation

This chapter will cover the concept, history, and usage of the finite element analysis (FEA) from past to present work. The usage and impact of the analysis tool in product and engineering development on our day-to-day basis. This technique is in continuous improvement by adding more complexity to the solving process and adding more physical phenomena to the virtual world.

FEA continues to evolve alongside advancements in computational power, integrating more sophisticated algorithms that expand its capability to simulate more complex physical interactions. These enhancements improve accuracy, efficiency, and applicability across various industries, ensuring FEA remains a core tool for optimizing designs, decreasing experimental costs, and predicting realistic performance with an increasing precision.

6.1 Introduction to FEA

The concept of finite element method is to divide the whole, either structure, body, or region being analyzed into several finite elements. This method was first introduced in computing by Turner et al, in 1956, and is considered as a computational technique to get approximate solutions to different physical engineering problems with different boundary conditions[45], [46].

When a defined set of elements with different characteristics has been placed, the method provides an approximate solution to the problem stated. This is conducted by the reduction of different equations and matrices that part from different assumptions [45].

The major steps throughout the years can be considered as follows[45]:

- 1) Discretization of the domain into a different number of subdomains.
- 2) Interpolation functions selection.
- 3) Development of the subdomain matrix.
- 4) Assembly of the different subdomain matrices into a global matrix.
- 5) Boundary conditions definition.
- 6) Solution of the equation.
- 7) Additional calculation if needed.

Other simplification of these steps can be defined as the pre-processing, processing and post-processing phases. Where the pre-processing involves from 1) to 5), the processing is basically the solution of the equations in 6) and the last

phase at 7) as the post-processing [47]. The process and modelling samples will be covered in the next sections of the chapter.

6.2 Historical development

Gauss developed a weighted residuals solution method for different matrices during the XVIII century, which was the foundation for approximate solutions in differential equations. Then the elasticity theory developed through the XIX century. The problematic and driver to elaborate a method that could provide a solution to the complex engineering problems was the calculation for the trajectories for the artillery. At the same time, the jet-propelled airplane was under development and presenting reliability issues [48].

During the 1950's, Turner and Clough began with the analysis but referred to as the direct stiffness method. Nonetheless, in 1960 it was described by Argyris and Clough as it is known today, Finite Element Analysis[45], [46], [48].

6.3 Methodology

The main approaches to construct an approximate solution within the FEA are the direct, weighted residuals and variational. The direct approach is typically used for simple problems, such as a linear spring system. Weighted residuals approach uses the FEA in problems where the functionals cannot be constructed. It is based on the governing differential equations, commonly used in the heat transfer and fluid mechanics. While the variation approach relies on the calculus of variations, involving the extremizing of the potential energy in structural mechanics[45].

6.3.1 Preprocessing

As noted, before, the initial step in the preprocessing is the discretization of the domain. This consists in the transformation of the practical engineering problem into a mathematical representation. The process is to divide the domain into elements. The elements are the representation of the subdomain, and they relate to each other through common nodes. Each node has its own coordinate location in the working space and includes its own degrees of freedom (DoF). Each nodal variable assigned to an element is also known as the degrees of freedom of the element [45], [47].

There are several types of element shapes and order. The element shape depends on the dimensional type, 1-D, 2-D or 3-D. The 1-D elements are for instance a truss element, "bars" type element. They do not cover any area nor volume, hence the 1-D naming. The 2-D element type can have the shape indicated in Figure 6.1. The

element order can be defined as linear or quadratic, commonly known also as first and second order, respectively. The difference between them is the number of nodes connected to them. Linear elements have the nodes at the intersection of their edges, while quadratic elements have additional nodes between the intersection. This increases the DoF for each element, increases the resolution but also the computational requirements for solving. The 3-D elements at the end have a volume in comparison to the previous types [46]. Different types of element shapes can be observed in Figure 6.2.

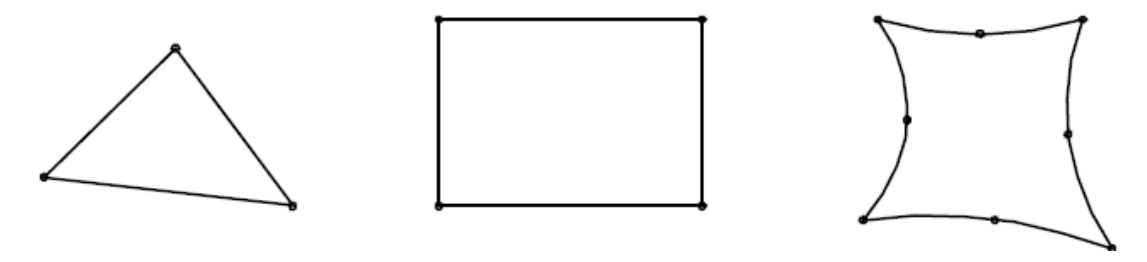


Figure 6.1 2-D Element shape: triangular, rectangular, quadrilateral [48]

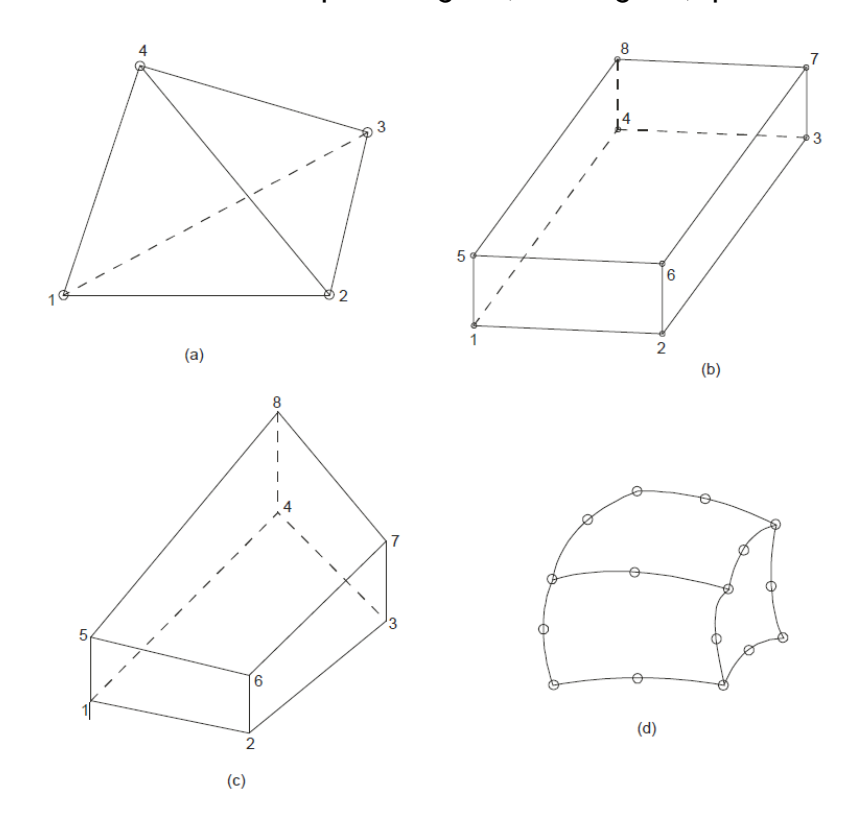


Figure 6.2 (a) Tetrahedron, (b) Rectangular prism, (c) Arbitrary hexahedron, (d) Three-dimensional quadratic [49].

Depending on the engineering principles, the degrees of freedom and force vectors will change in the FEA [45]. Further information samples can be noted in Table 5-1.

5		
Discipline	DOF	Force vector
Structural/solids	Displacement	Mechanical forces
Heat conduction	Temperature	Heat flux
Acoustic fluid	Displacement potential	Particle velocity
Potential flow	Pressure	Particle velocity
General flows	Velocity	Fluxes
Electrostatics	Electric potential	Charge density
Magnetostatics	Magnetic potential	Magnetic intensity

Table 6-1 Degrees of freedom and force vectors per discipline.

Nodes are also known as the interpolation functions and are a step of the discretization of the problem, refer to Figure 6.3 for a visual sample. In commercial software it is known as "meshing". They are also defined as the terms of the values of the field variables at specific points [45], [47].

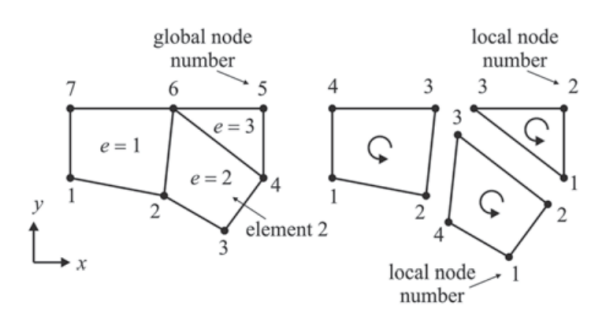


Figure 6.3 Element discretization of a domain[45].

Finally, the boundary conditions are the constraints that define the interactions of the model with its surroundings. Some of the inherent characteristics of the body such as the material properties that can be defined as the density, Young's modulus, Poisson's ratio, among others. The body interactions as contacts, flexible or rigid body elements and their corresponding constraints with different degrees of freedom. Vectors, such as forces, or scalars as pressures are also other types of available loads aside from the displacements, torque and so on[50].

Depending on the discipline, the development of the subdomain matrix will take place. In the case of structural analysis, it is often explained with the stiffness method.

The governing equation is taken from Hooke's Law, and in the standard matrix displacement in Equation 6.1.

$$[k]$$
 $\{\delta\} = \{F\}$ Equation 6.1

Where:

|k| is the stiffness matrix

 $\{\delta\}$ is the displacement vector (unknowns) $\{F\}$ is the force vector in the coordinate directions

According to the nature of the problem, the stiffness matrix may be dependent on the displacement vector or that the force vector dependent on time. In the next example shown in Figure 6.4, it is displayed the development and assembly of subdomain functions. The linear spring with two nodes has a stiffness k. Each node has axial loads f and a displacement u.

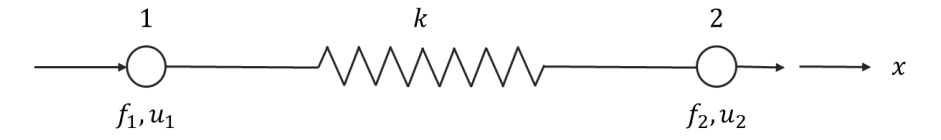


Figure 6.4 Free-body diagram of a linear spring element.

When the forces acting on the nodes generate a deformation, the spring's definition is defined by Equation 6.2

$$u = u_1 - u_2$$
 Equation 6.2

This relates to the force acting on the spring as shows Equation 6.3.

$$f_1 = ku = k(u_1 - u_2)$$
 Equation 6.3

Since it is a static analysis, the forces are in equilibrium depicted in Equation 6.4.

$$f_2 = -f_1$$
 Equation 6.4

The equation can be rewritten as Equation 6.5.

$$f_2 = k(u_2 - u_1)$$
 Equation 6.5

These set of equations can be taken to a matrix form to be solved shown in Equation 6.6 or Equation 6.7.

$$\begin{bmatrix} k & -k \\ -k & k \end{bmatrix} \begin{cases} \underline{u_1} \\ \underline{u_2} \end{cases} = \begin{cases} \underline{f_1} \\ \underline{f_2} \end{cases}$$
 Equation 6.6
$$\mathbf{k}^{(e)} \mathbf{u}^{(e)} = \mathbf{f}^{(e)}$$
 Equation 6.7

Where $\mathbf{u}^{(e)}$ is the vector of nodal unknowns that represent the displacement and $\mathbf{k}^{(e)}$ and $\mathbf{f}^{(e)}$ are referred to, as the element characteristic matrix and element vector. The characteristic matrix is also known as the stiffness matrix, and element vector is also named the force vector. The superscript (e) denotes the element number[45], [46], [48], [49].

The previous system depicts a small system, however the advantage of having a large-scale model with millions of nodes and elements is the core usage of the FEA. The following formulae are an example of the assembly of a global system of equations, from the system in Figure 6.5.

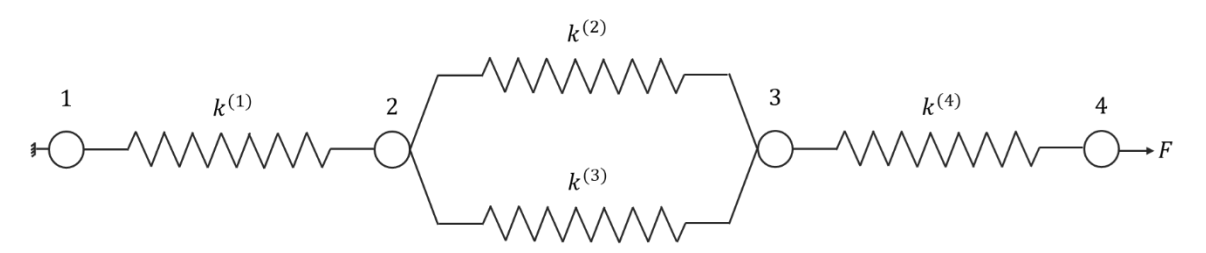


Figure 6.5 FEA model of linear springs.

To accomplish a global system matrix, K, parts from the expanded element coefficient matrices, $k^{(e)}$, by the summation form in Equation 6.8

$$\mathbf{K} = \sum_{e=1}^{E} \mathbf{k}^{(e)}$$
 Equation 6.8

At each local level of the springs, they have a behavior as Equation 6.6, still the connectivity with the other nodes change in the global node numbering as can be observed in the Table 6-2.

Table 6-2 Node and element connectivity table.

Element number	Local node numbering	Global node numbering
1	1	1
	2	2
2	1	2
	2	3
3	1	2
	2	3
4	1	3
	2	4

As depicted in Figure 6.5, the system consists of four spring elements which will be rewritten as with the elemental association as shown in the Equation 6.9.

$$\begin{bmatrix} k_{11}^{(e)} & k_{12}^{(e)} \\ k_{21}^{(e)} & k_{22}^{(e)} \end{bmatrix} \begin{pmatrix} u_1^{(e)} \\ u_2^{(e)} \end{pmatrix} = \begin{cases} f_1^{(e)} \\ f_2^{(e)} \end{cases}$$

Equation 6.9

Note that the subindex corresponds to the node number of the element. The global matrix is going to be constructed as show in Table 6-3.

Table 6-3 Element stiffness decomposition.

Element number	Element matrix	Global Matrix	Stiffness Index
1	$\begin{bmatrix} k_{11}^{(1)} & k_{12}^{(1)} \\ k_{21}^{(1)} & k_{22}^{(1)} \end{bmatrix}$	$\begin{bmatrix} k_{11}^{(1)} & k_{12}^{(1)} & 0 & 0 \\ k_{21}^{(1)} & k_{22}^{(1)} & 0 & 0 \\ 0 & 0 & 0 & 0 \\ 0 & 0 & 0 & 0$	k ⁽¹⁾
2	$\begin{bmatrix} k_{11}^{(2)} & k_{12}^{(2)} \\ k_{21}^{(2)} & k_{22}^{(2)} \end{bmatrix}$	$ \begin{bmatrix} 0 & 0 & 0 & 0 \\ 0 & k_{11}^{(2)} & k_{12}^{(2)} & 0 \\ 0 & k_{21}^{(2)} & k_{22}^{(2)} & 0 \\ 0 & 0 & 0 & 0 \end{bmatrix} $	k ⁽²⁾
3	$\begin{bmatrix} k_{11}^{(3)} & k_{12}^{(3)} \\ k_{21}^{(3)} & k_{22}^{(3)} \end{bmatrix}$	$\begin{bmatrix} 0 & 0 & 0 & 0 \\ 0 & k_{11}^{(3)} & k_{12}^{(3)} & 0 \\ 0 & k_{21}^{(3)} & k_{22}^{(3)} & 0 \\ 0 & 0 & 0 & 0 \end{bmatrix}$	k ⁽³⁾
4	$\begin{bmatrix} k_{11}^{(4)} & k_{12}^{(4)} \\ k_{21}^{(4)} & k_{22}^{(4)} \end{bmatrix}$	$\begin{bmatrix} 0 & 0 & 0 & 0 \\ 0 & 0 & 0 & 0 \\ 0 & 0 &$	$\mathbf{k}^{(4)}$

The assembly of the stiffness of each element in the global matrix by following Equation 6.8, and it is depicted in Equation 6.10 or Equation 6.11.

$$\mathbf{K} = \begin{bmatrix} k_{11}^{(1)} & k_{12}^{(1)} & 0 & 0 \\ k_{21}^{(1)} & (k_{21}^{(2)} + k_{21}^{(3)}) & (k_{12}^{(2)} + k_{11}^{(3)}) & 0 \\ 0 & (k_{21}^{(2)} + k_{21}^{(3)}) & (k_{22}^{(2)} + k_{11}^{(3)}) & k_{12}^{(4)} \\ 0 & 0 & k_{21}^{(4)} & k_{21}^{(4)} & k_{22}^{(4)} \end{bmatrix}$$
 Equation 6.10

The same assembly process is conducted for the force as it can be observed in the Table 6-4. Then their assemblies can be rearranged as in Equation 6.12 or Equation 6.13.

Table 6-4 Force contribution per element

Element number	Element matrix	Global Matrix	Force Index
1	$ \begin{cases} f_1^{(1)} \\ f_2^{(1)} \end{cases} $	$\begin{pmatrix} f_1^{(1)} \\ f_2^{(1)} \\ 0 \\ 0 \end{pmatrix}$	f (1)
2	$ \begin{cases} f_1^{(2)} \\ f_2^{(2)} \end{cases} $	$ \begin{pmatrix} 0\\f_1^{(2)}\\f_2^{(2)}\\0 \end{pmatrix} $	f (2)
3	$ \begin{cases} f_1^{(3)} \\ f_2^{(3)} \end{cases} $	$ \begin{pmatrix} 0\\f_1^{(3)}\\f_2^{(3)}\\0 \end{pmatrix} $	f (3)
4	(f ₁ ⁽⁴⁾) (f ₂ ⁽⁴⁾)	$\begin{pmatrix} 0 \\ 0 \\ f_1^{(4)} \\ f_2^{(4)} \end{pmatrix}$	f (4)

$$f = \sum_{e=1}^{4} f(e) = f(1) + f(2) + f(3) + f(4)$$
 Equation 6.12

$$\mathbf{f} = \begin{cases} f_1 \\ f_2 \\ f_3 \\ f_4 \end{cases} = \begin{cases} f_1^{(1)} \\ f_2^{(2)} + f_1^{(2)} + f_1^{(3)} \\ f_2^{(2)} + f_2^{(3)} + f_1^{(4)} \\ f_2^{(4)} \end{cases}$$
 Equation 6.13

Finally, for the displacement matrix it will be takin the shape as indicated in Equation 6.14.

$$\mathbf{u} = \begin{cases} u_1 \\ u_2 \\ u_3 \\ u_4 \end{cases} = \begin{cases} u_1^{(1)} \\ u_2^{(1)} = u_1^{(2)} = u_1^{(3)} \\ u_2^{(2)} = u_2^{(3)} = u_1^{(4)} \\ u_2^{(4)} \end{cases}$$
 Equation 6.14

6.3.2 Processing

The solution of the global matrix system is the processing phase, which is finding the values to the unknowns of the equation systems. To accomplish the reduction of the system and have a unique solution, the determinant of the global matrix must be nonzero. Computing the global matrix, it is revealed that one of its eigenvalues is zero, hence resulting in a zero determinant or singular matrix. Since the solution is not unique, the eigenvector corresponding to a zero eigenvalue represents a translational mode, while the remaining nonzero eigenvalues represent all the deformation modes.

When in our system $k_{11}^{(e)} = k_{22}^{(e)} = k^{(e)}$ and $k_{12}^{(e)} = k_{21}^{(e)} = -k^{(e)}$, the global matrix will be arranged as show in Equation 6.15.

$$\mathbf{K} = k^{(e)} \begin{bmatrix} 1 & -1 & 0 & 0 \\ -1 & 3 & -2 & 0 \\ 0 & -2 & 3 & -1 \\ 0 & 0 & -1 & 1 \end{bmatrix}$$
 Equation 6.15

The solution for the eigenvalues from the global matrix are λ_1 = 0, λ_2 = 2, λ_3 = 3 – $\sqrt{5}$,and λ_4 = 3 + $\sqrt{5}$ showing the eigenvectors in Equation 6.16.

$$\mathbf{u}^{(1)} = \begin{cases} 1\\1\\1\\1\\1 \end{cases}, = \mathbf{u}^{(2)} = \begin{cases} 1\\-1\\-1\\1 \end{cases}, \mathbf{u}^{(3)} = \begin{cases} -1\\2-\sqrt{5}\\-2+\sqrt{5}\\1 \end{cases}, \mathbf{u}^{(3)} = \begin{cases} -1\\2-\sqrt{5}\\1\\1 \end{cases}$$
 Equation 6.16

The eigenvectors displayed in the *Equation 6.16*, depict a possible solution, however at this point it cannot be solved since it is missing the accountability of the boundary conditions. Which must be specified at the preprocessing phase. Otherwise, the approximation results (if achieved) will show an incorrect solution.

In the assumption that the displacement in node #1 is constrained in all directions, it will mean that u_1 = 0. While the rest of the displacements are unknown.

Regarding the corresponding nodal forces, f_1 is unknown, but f_2 = 0, f_3 = 0, and f_4 = F

Replacing the known values from the boundary conditions it forms the Equation 6.17, and leading to Equation 6.18 and Equation 6.19.

$$k^{(e)} \begin{bmatrix} 1 & -1 & 0 & 0 \\ -1 & 3 & -2 & 0 \\ 0 & -2 & 3 & -1 \\ 0 & 0 & -1 & 1 \end{bmatrix} \begin{bmatrix} u_1 = 0 \\ u_2 \\ u_3 \\ u_4 \end{bmatrix} = \begin{cases} f_1 \\ f_2 = 0 \\ f_3 = 0 \\ f_4 = F \end{cases}$$
 Equation 6.17
$$k^{(e)} \begin{bmatrix} 3 & -2 & 0 \\ -2 & 3 & -1 \\ 0 & -1 & 1 \end{bmatrix} \begin{bmatrix} u_2 \\ u_3 \\ u_4 \end{bmatrix} = \begin{cases} 0 \\ 0 \\ F \end{cases}$$
 Equation 6.18
$$-k^{(e)}u_2 = f_1$$
 Equation 6.19

With the addition of the boundary condition, the coefficient matrix changes since it is no longer singular and yields the following solution in Table 5-1.

Table 6-5 Solution to displacements

Solution to the displacements per element		
$u_2 = \frac{F}{k^{(e)}}$	$u_3 = \frac{3 F}{2k^{(e)}}$	$u_4 = \frac{5 F}{2k^{(e)}}$

6.3.3 Postprocessing

The results from the solution phase or processing phase must be interpreted and evaluated to determine if they make engineering sense. Nowadays the commercial analysis software has the ability to create different plots and trace results per, element, node, body, among other features [47].

Postprocessing results depend as well on the engineering discipline. The nature between the different physics phenomena, such as the high speed and low speed situations, such as a modelling a car crash, or a beam under static load. These are also classified between explicit and implicit simulations[51].

The Figure 6.6 shows a maximum and minimum principal stress plot of a connecting rod simulation. The common information to be gathered is the locations where the stress has concentrations that can be related to a possible failure. It is common that some locations present high concentrations, but it is the analyst's task to determine whether it is a potential hotspot or a singularity. Stress

singularities are relatively common. They usually generate high stress values that tend to go to infinity. The contact as well can create a singularity due to the over constraint of the nodes selected[49].

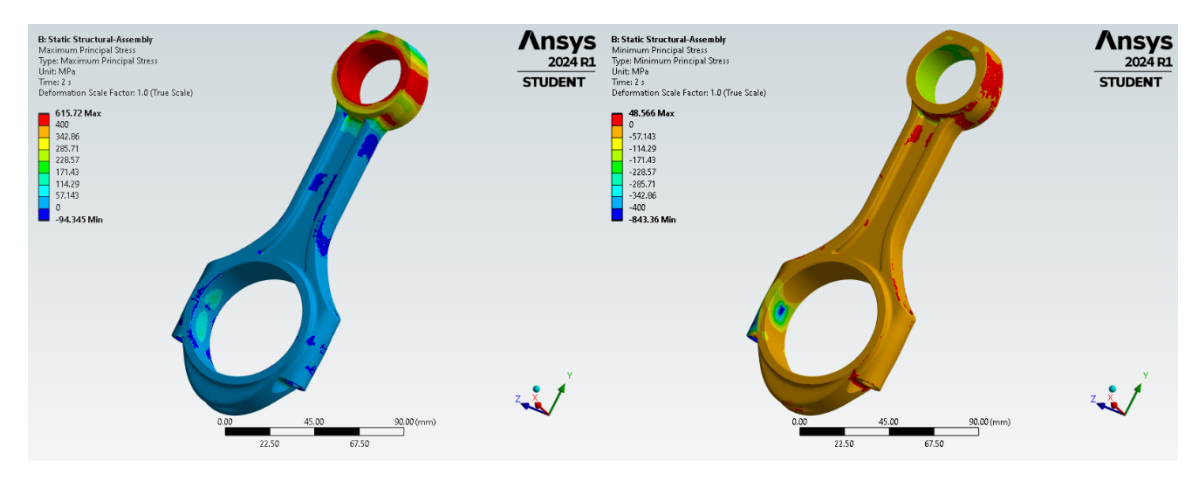


Figure 6.6 Max and min principal stress plot sample.

The results' quality depends on the preprocessing phase, so the quality given will impact heavily on the results. Mesh quality in terms of shape, type, ratios and aspects will end up showing different results but there are available tools to ensure the mesh's convergence and validity.

6.4 Modelling approaches and applications

In the last few years, there have been enhancements to the different software packages that have increased their fidelity. As well as computational power increases, the complexity of the engineering problems to solve becomes achievable [52]. The linearity is related to the complexity of the model and is a key factor for the computational demand.

Common nonlinearities are listed as follows:

- Contact behavior.
- Geometry deflection.
- Material properties.

Contact definition is a key step in the preprocessing phase, and its nonlinearity depends on the degrees of freedom allowed. By nature, the contact has a normal and tangential relationship when defined between two faces. If there is a constraint in one of the degrees of freedom, the linearity will be preserved. Otherwise, the

contact will be nonlinear and can lead to quite different results, since it can allow or constrain the relative displacement between elements[47].

The small or large deflections of a geometry change the stiffness of the system and adds another variable for the calculations. The deflection is usually controlled by the user within the software, but within the preprocessing adds the change in stiffness due to the deformation or displacement of the nodes, which generates a recalculation of the global and local matrices[45].

Material nonlinearities are mostly defined on the elasticity and plasticity of materials. Depending on the component to be analyzed, this nonlinearity will be used. For instance, in modelling of gaskets, or components that will exceed their yield strength, there must be a consideration for the nonlinearity[45].

The effectiveness of FEA depends on properly defining the right fidelity model. This means selecting the appropriate level of complexity for a given problem. Contact definition is essential in capturing realistic interactions between components, influencing factors like friction, pressure distribution, and material deformation. While they all can bring simplifications and complexities for a given model.

Accurately modeling these interactions can give stress and displacement values that reflect actual behavior under operational conditions. Additionally, incorporating multi-physics such as thermal effects, pressures, and electromagnetism can allow developing more comprehensive simulations that account for the complexities of actual applications.

Chapter 7 Experimental process

This chapter will cover the different procedures to achieve the general and specific objectives of the project. Initially a worksheet was developed to obtain the theoretical loads that the connecting rod would face in engine operations and field operations.

The dynamic loads are used as inputs for the different load cases that will face the connecting rod, translating them among the testing conditions, field, and laboratory conditions to a virtual model. In order to apply the design of experiments methodology a factorial DoE (design of experiments) was selected.

The DoE will address with a statistical and linear methodology the effects that mostly affect the connecting rod. The response obtained will provide a confirmation in the assumptions for testing and potential further effects to be considered for failures.

7.1 Dynamic load calculation

To have certainty for the dynamic loads to be used on the static analysis, a study was implemented from another benchmark engine between AVL's Excite PU (EPU), Ansys Rigid Dynamics (ARD) and an Excel based calculator (Ecalc).

The inputs considered for the dynamic load calculator are listed below:

- 际 Reciprocating mass
 - o Piston
 - o Piston pin
 - Bushing
 - o Rings' mass
 - o Mass portion of the connecting rod (1/3)
- 际 Crankshaft angular speed
- 际 Crankshaft radius
- 际 Length of the connecting rod (bore to bore)

7.2 Geometry description of Engine "A" connecting rod

The first connecting rod to be studied is the one of the Engine "A". The component was initially preprocessed in SpaceClaim within the Ansys Workbench software. Component descriptions is as follows in Figure 7.1:

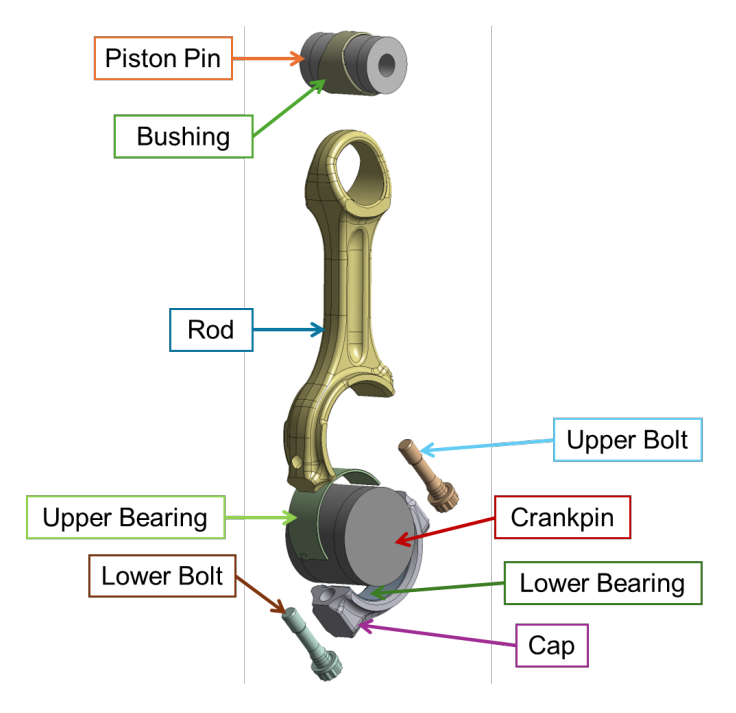


Figure 7.1 Connecting rod components for simulation.

The initial revision has a 1-millimeter radius while the production part has 1.5 millimeters, detail shown in the Figure 7.2. The same procedure will be run in the updated revision of the production part that currently passed the test.

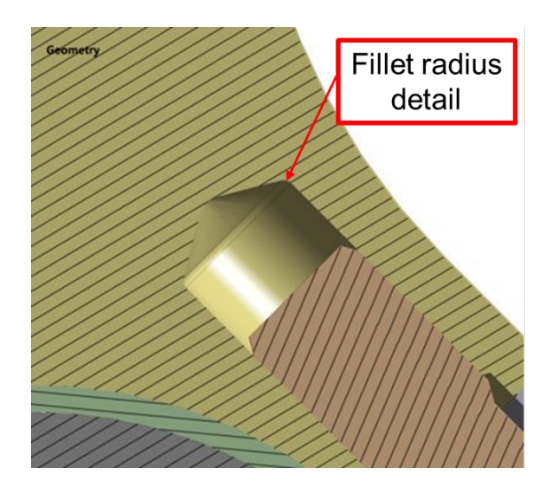


Figure 7.2 Fillet radius detail of first revision.

Regarding the component detail to be used, it has been decided to consider the connecting rod as the focus component, while the rest of the list will be taken as secondary and auxiliary components. In SpaceClaim, the following parameters to address the physical manufacturing and assembly conditions must be adjusted:

- 际 The bushing press fit must be adjusted, by giving the interior mean diameter of interference to the wrist pin and the bushing. So, the interference being the established on the print.
- 际 In the bolt and thread diameters, they are modified to match the mean pitch diameter from the according standard.
- 呀 Bearing to bearing interface is set to zero interference, but matching faces.

7.3 Load case description

The torque curve performance of the engine depicted in Figure 7.3, obtained by physical test or performance simulations will be used to generate the load cases of the engine operation.

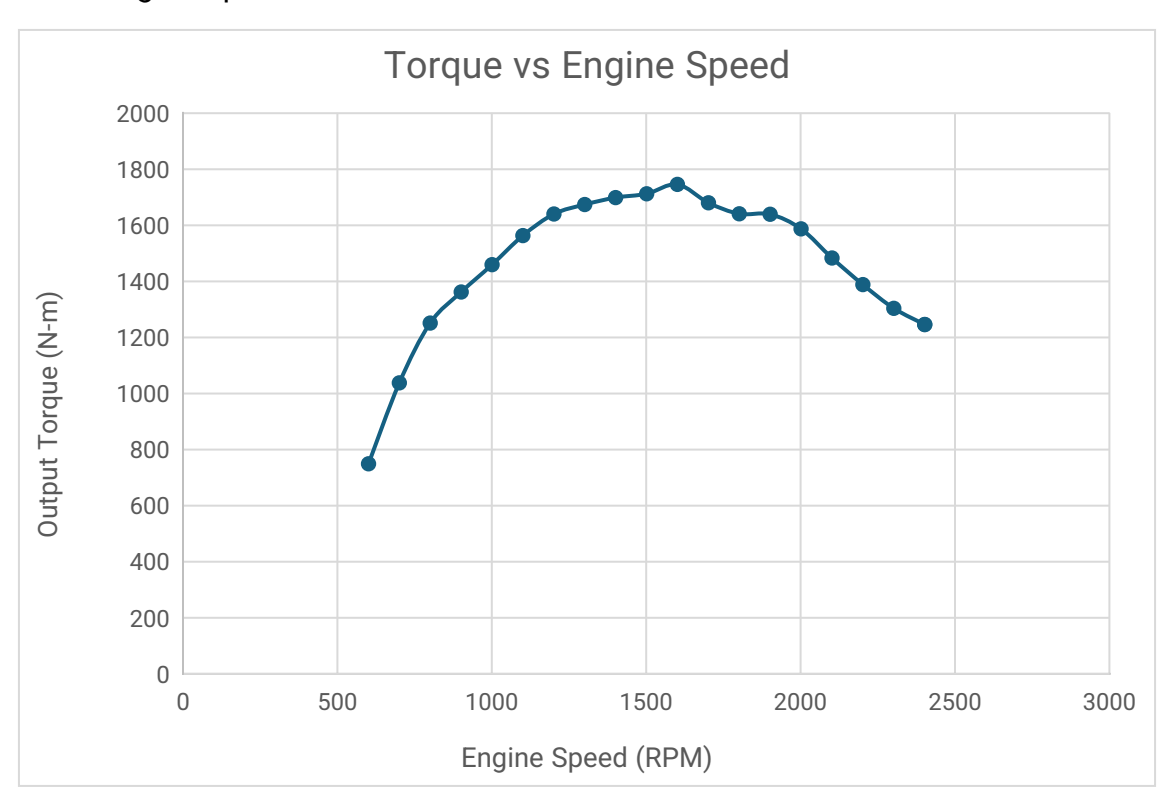


Figure 7.3 Output torque vs Engine speed curve.

The firing load cases are going to be extracted to cover the firing pressure in Figure 7.4 plus the inertial loads due to the accelerations involved in the connecting rod mechanism.

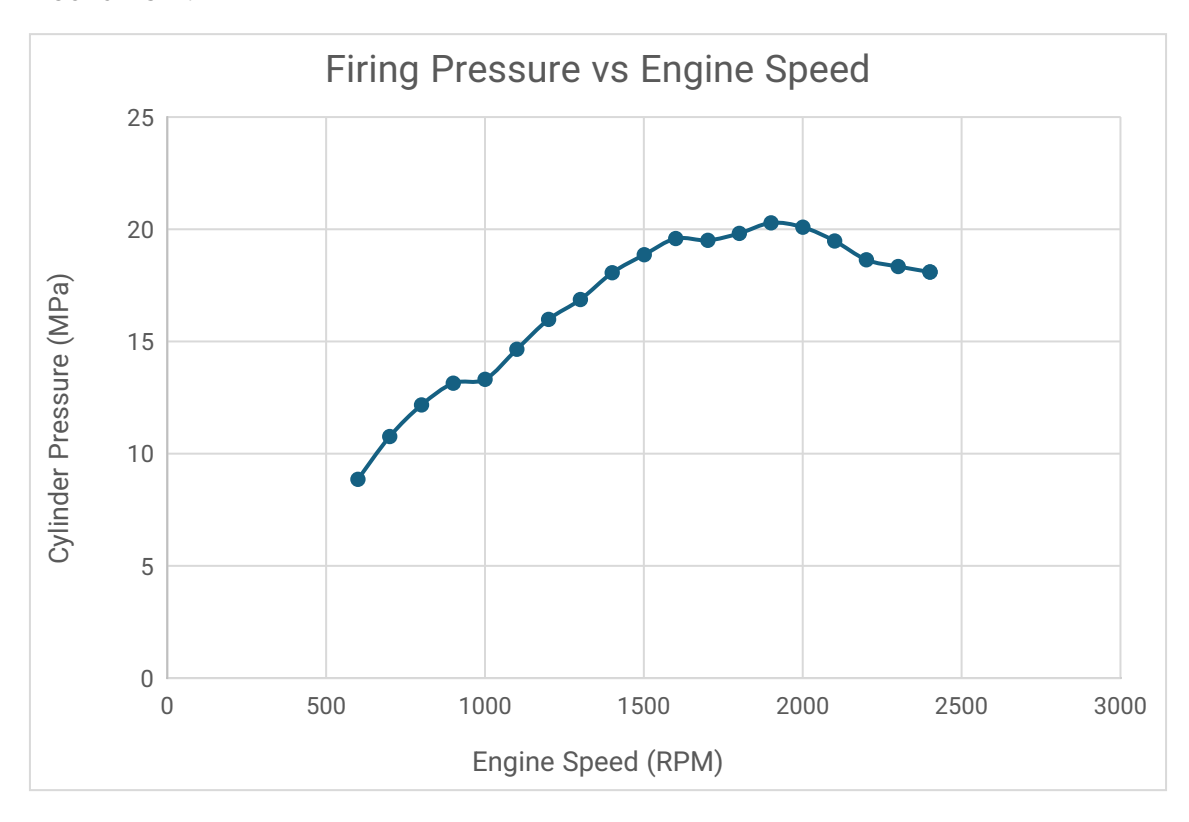


Figure 7.4 Firing pressure vs Engine speed curve.

Load case setup description is as follows, plus the configuration can be observed in Figure 7.5:

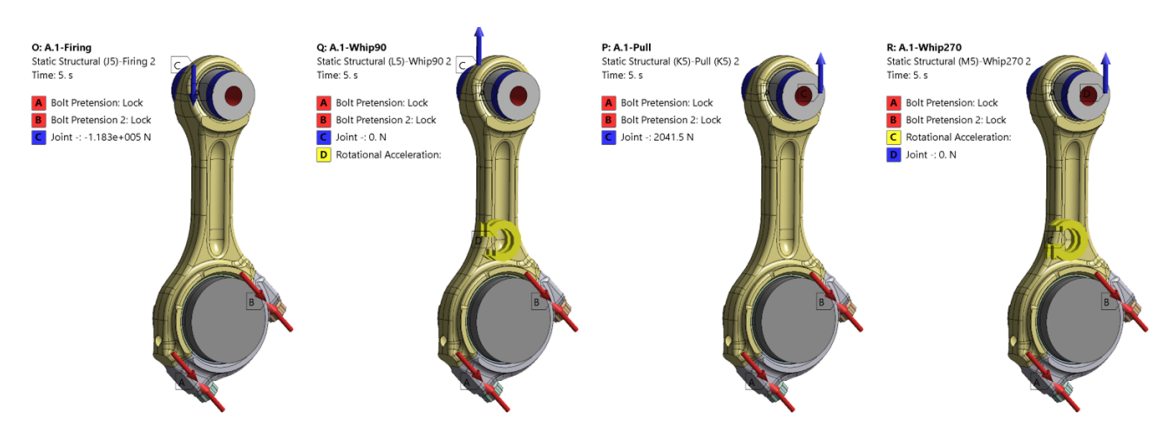


Figure 7.5 Load cases description.

Assembly of the connecting rod, also initial state for following load cases.

- a. Bolt pretension to nominal specification of 85,000 N.
- b. Bearing crush, due to the contact offset between bearing to bearing.
- c. Bushing press fit and piston pin assembly.
- 1. Firing load at the connecting rod.
 - a. Application of the firing load at the piston pin, calculated by Equation 3.16.
 - b. Incremental load at each step to cover the firing forces at the demand of the torque from 600 to 2400 r.p.m.
- 2. Lateral acceleration at 270° rotation of the crankshaft from top dead center.
 - a. The speed of the crankshaft is going to be from 1,300 to 2,400 r.p.m. plus an overspeed condition of 3,600 r.p.m.
- 3. Lateral acceleration at 90° rotation of the crankshaft from top dead center.
 - a. The speed of the crankshaft is going to be from 1,600 to 2,400 r.p.m. plus an overspeed condition of 3,600 r.p.m.
- 4. Pull load due to the acceleration of the piston.
 - a. The pull load was calculated by Equation 3.15, depending on the linear acceleration of the piston according to the crankshaft's speed. Incremented at each step, to cover the forces due to the speeds of 600 to 2,400 r.p.m. Additionally a load case condition of 3,600 r.p.m.

Frictional loads due to the interface between the piston and liner are not considered since the theoretical loads are less than 0.01% and do not really represent an impact on the results.

A summary of the load cases per each of the speed is shown in the Figure 7.6. Where the full engine performance curve is represented at each of the crankshaft speeds, note as well that it shows that the maximum combustion force is at 1,900 r.p.m. while the highest acceleration is proportionally increasing with the engine speed.

Engine Speed	MaxPressure •	Firing Load (N)	AœSE	Pull Load (N)	Whip90 (rad/s^ئ	Whip 270 (rad/s^2)
600.00	8837674.75	-97304.14	352.19	1499.86	1296.10	-1296.10
700.00	10744818.72	-118302.08	479.37	2041.48	1764.14	-1764.14
800.00	12034807.34	-132505.05	626.12	2666.43	2304.19	-2304.19
900.00	13129862.52	-144561.77	792.43	3374.70	2916.24	-2916.24
1000.00	13291504.30	-146341.47	978.31	4166.29	3600.29	-3600.29
1100.00	14606793.99	-160823.01	1183.75	5041.21	4356.35	-4356.35
1200.00	15954373.91	-175660.07	1408.76	5999.46	5184.42	-5184.42
1300.00	16803660.40	-185010.84	1653.34	7041.03	6084.49	-6084.49
1400.00	17972190.83	-197876.54	1917.48	8165.93	7056.57	-7056.57
1500.00	18711287.63	-206014.11	2201.19	9374.15	8100.65	-8100.65
1600.00	19462155.96	-214281.28	2504.47	10665.71	9216.74	-9216.74
1700.00	19325423.68	-212775.84	2827.31	12040.58	10404.84	-10404.84
1800.00	19462155.96	-214281.28	3169.72	13498.78	11664.94	-11664.94
1900.00	20258238.22	-223046.27	3531.69	15040.31	12997.05	-12997.05
2000.00	20091440.66	-221209.80	3913.23	16665.16	14401.16	-14401.16
2100.00	19360860.62	-213166.00	4314.34	18373.34	15877.28	-15877.28
2200.00	18455514.42	-203198.01	4735.01	20164.85	17425.40	-17425.40
2300.00	18200864.40	-200394.27	5175.25	22039.68	19045.53	-19045.53
2400.00	18024534.57	-198452.85	5635.06	23997.84	20737.67	-20737.67
3600.00	N/A	N/A	12678.87	53995.13	46659.76	-46659.76

Figure 7.6 Load cases summary per engine speed.

7.4 Factorial design of experiments

A factorial design of experiments was carried out to determine the factors that have most of the effect on the connecting rod's fillet. The response to be measured through the finite element model was the alternating stress at the failure location. On the Table 7-1 it can be observed the design's summary.

Table 7-1 Design summary

Factors:	6	Base Design:	6, 16	Resolution:	IV
Runs:	16	Replicates:	1	Fraction:	1/4
Blocks:	1	Center pts (total):	0		

Design Generators: E = ABC, F = BCD

The factors considered for the study were as follows on Table 7-2, followed by the alias structure for the analysis indicated in

Table 7-3. The alias table shows the relationship between the different factor combinations used for the DoE.

Table 7-2 Alias structure naming

Factor	Name	Description
Α	Firing	Firing load due to combustion
В	Lat90	Lateral acceleration at 90° crank angle
С	Lat270	Lateral acceleration at 270° crank angle
D	Bolt Preload	Bolt pretension load
E	Bearing Crush	Bearing crush offset
F	Tension	Pull load due to reciprocating mass vertical acceleration

Table 7-3 Alias structure

Alias S	tructure
I + ABCE + ADEF + BCDF	AC + BE + ABDF + CDEF
A + BCE + DEF + ABCDF	AD + EF + ABCF + BCDE
B + ACE + CDF + ABDEF	AE + BC + DF + ABCDEF
C + ABE + BDF + ACDEF	AF + DE + ABCD + BCEF
D + AEF + BCF + ABCDE	BD + CF + ABEF + ACDE
E + ABC + ADF + BCDEF	BF + CD + ABDE + ACEF
F + ADE + BCD + ABCEF	ABD + ACF + BEF + CDE
AB + CE + ACDF + BDEF	ABF + ACD + BDE + CEF

Next, the design randomization of factors and levels were applied. Where the low and high levels are the maximum and minimums values for each factor. For instance, for the factor "F" (Tension), the maximum and minimum values are at the highest and lowest engine speeds, respectively.

On Table 7-4, it can be observed the design of experiments, note that the "+" indicates the highest level, while the "-" the lowest level.

Table 7-4 Design table (randomized)

Run	Block	Α	В	С	D	Ε	F
1	1	-	+	+	-	-	-
2	1	+	+	-	+	-	-
3	1	-	+	+	+	-	+
4	1	-	+	-	-	+	+
5	1	-	+	-	+	+	-
6	1	+	+	+	-	+	-
7	1	+	-	+	-	-	+
8	1	+	+	+	+	+	+
9	1	-	-	+	-	+	+
10	1	+	-	-	-	+	-
11	1	+	-	-	+	+	+
12	1	+	-	+	+	-	-
13	1	-	-	-	-	-	-
14	1	-	-	-	+	-	+
15	1	+	+	-	-	-	+
16	1	-	-	+	+	+	-

7.5 Finite element model description for the Engine "A" connecting rod.

The finite element model (onwards FE model) was developed within Ansys Mechanical. The mesh was created with tetrahedral second order elements, for components with exception on the crankshaft surface since it is a surface mesh.

The thread size locations for bolt and rod, was modelled with $\frac{1}{4}$ of the pitch length since it is required for the contact modelling. Mesh can be observed in Figure 7.7.



Figure 7.7 Mesh generated for the simulation.

Contact configurations are as follows depending on the nature of the physical interactions:

- sushing to rod: the press fit occurs on manufacturing process, from bronze coated to steel interface. It has a friction coefficient of 0.2.
- 际 Piston pin to bushing: high lubricated joint, from bronze coated to steel interface. It was supposed that there is a friction coefficient of 0.07.
- 际 Rod to bolt: from steel-to-steel interface. It has a friction coefficient of 0.14. According to the print specification of the bolt's coating.

- 际 Cap to rod: from steel-to-steel interface. It is known that there is a friction coefficient of more than 1. It is fracture split with irregular contours, so it is modelled as a rough contact to decrease the computational effort.
- 际 Bearing to rod & bearing to cap: these are assembled with some lubrication but at the bearing crush, the interface oil is pressed out. So, to account for remaining particles, it has is a friction coefficient of 0.23.
- 际 Bearing to bearing: Due to bearing crush effect it is assigned an offset previously calculated, and dry assembly so that the friction coefficient of 0.23 due to the steel-to-steel interface but with wear protecting coating.
- 际 Crankshaft to bearings: Since there is a constant oil supply, and a clearance due to the oil film. The contact is modelled as an exponential contact, which implies a minimum given gap and a pressure, which is calculated as the 5% of the firing force in the bearing shell area. Frictionless contact is used since friction coefficient rounds values between 10^{-6} and 10^{-7} .

A fixed joint element has been applied to the crankshaft's geometry.

The contact status can be observed in Figure 7.8.

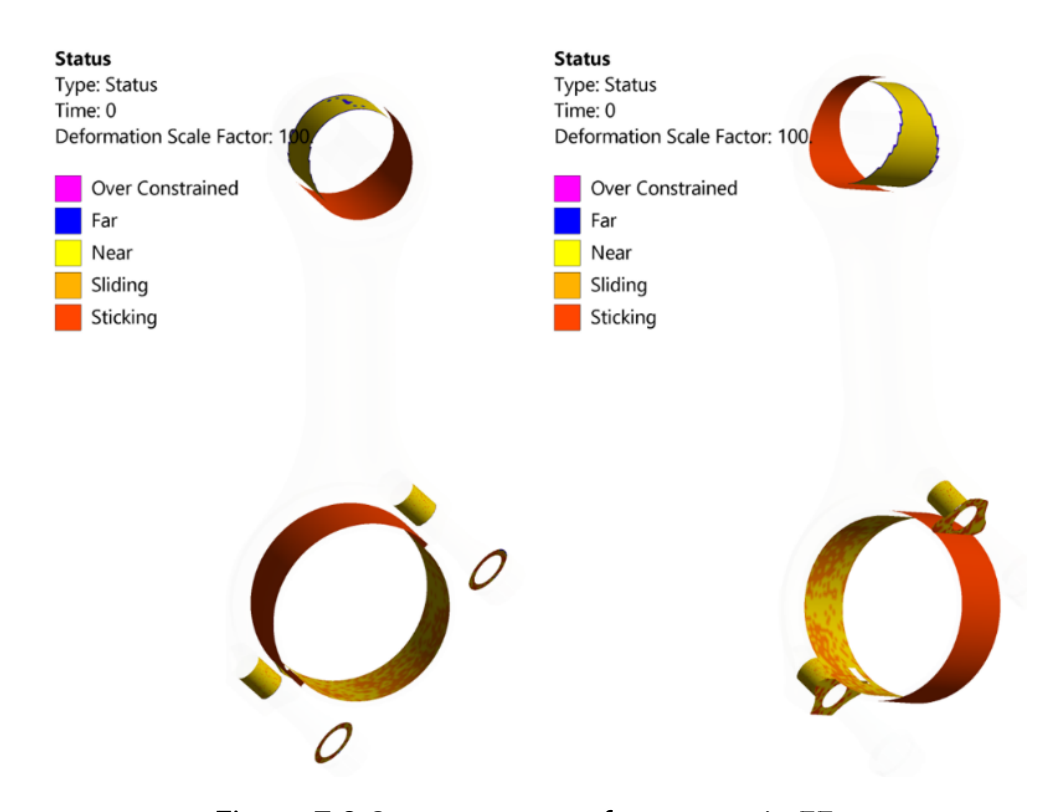


Figure 7.8 Contact status of geometry in FE.

Chapter 8 Results & discussion

The following results section will cover the findings of the experimental process. Reviewing from the crack during testing as the physical evidence of the design intent. The connection between the testing and the finite element analysis will be supported by the findings on the design of experiments.

8.1 Testing Results

As shown during the testing practices for the connecting rods in the industry, the common load cases are the compression and tension scenarios. The connecting rod is subjected to a load assimilating a peak firing pressure of the cylinder and a high-tension load that assimilates a high crankshaft speed as shown in Table 8-1. Nonetheless, with the intention to speed up the testing, it is used an accelerated fatigue testing with the corresponding equivalences.

Table 8-1 Testing loads.

Compression (kN)	Tension (kN)
-263.4	78.5

The broken connecting rod found during testing had the crack initiation at the blind thread of the connecting rod, as shown in Figure 8.1. The connecting rod did not meet the cycles expected. Afterwards it was determined that the crack initiation was due to fatigue since the components were compliant with the tolerances and material specification per the requirement.



Figure 8.1 Broken connecting rod of engine "Engine "A".

Additionally, on the Figure 8.2 it can be observed the origin of the crack at the fillet location of the blind hole of the rod. The pattern of the "beach" lines and the transition of the areas are some of the signs of the fatigue crack.



Figure 8.2 Crack initiation site of the connecting rod in Engine "A".

8.2 Design of experiments results

From the results of the coded coefficients of the study shown in *Table 8-2*, it can be noted that the effect of the firing and tension factors have the highest magnitudes.

The highlighted effects suggest that the increase in those magnitudes of these factors from low to high values will have an increment in the output, in this case the alternating stress on the fillet. The remaining lower values denote that the other factors do not have a strong impact in the outcome in comparison.

Term	Effect	Coef	SE Coef	T-Value	P-Value	VIF
Constant		14.9163	0.0667	223.66	0.000	
Firing	5.7548	2.8774	0.0667	43.14	0.000	1.00
Lat90	-0.0085	-0.0043	0.0667	-0.06	0.951	1.00
Tension	1.2824	0.6412	0.0667	9.61	0.000	1.00
Firing*Lat90	-0.0259	-0.0130	0.0667	-0.19	0.851	1.00
Firing*Tension	-0.5780	-0.2890	0.0667	-4.33	0.003	1.00
Lat90*Tension	-0.2755	-0.1378	0.0667	-2.07	0.073	1.00
Firing*Lat90*Tension	-0.2585	-0.1292	0.0667	-1.94	0.089	1.00

Table 8-2 Coded coefficients for the factors.

On Table 8-3, the coefficient of determination, R^2 , is 99.60%. This indicates that the model fits the data adequately and can be useful for predicting response behavior.

The result is also valid, as the test procedure historically represents both compression and tension cases. If the value was above 100%, it would indicate overfitting of the data taken. Alternatively, if the value was less than 100%, only that percentage of variance is explained by the variables in the DoE model.

Table 8-3 Coefficient of determination.

S	R-sq	R-sq(adj)	R-sq(pred)
0.266769	99.60%	99.25%	98.39%

The analysis of variance (ANOVA) shown in Table 8-4, displays as well that the adjusted sum of squares of the firing and tension factors are the highest magnitudes.

Table 8-4 Analysis of variance

Source	DF	Adj SS	Adj MS	F-Value	P-Value
Model	7	140.959	20.137	282.96	0.000
Linear	3	139.049	46.350	651.29	0.000
Firing	1	132.471	132.471	1861.44	0.000
Lat90	1	0.000	0.000	0.00	0.951
Tension	1	6.578	6.578	92.43	0.000
2-Way Interactions	3	1.643	0.548	7.69	0.010
Firing*Lat90	1	0.003	0.003	0.04	0.851
Firing*Tension	1	1.336	1.336	18.78	0.003
Lat90*Tension	1	0.304	0.304	4.27	0.073
3-Way Interactions	1	0.267	0.267	3.76	0.089
Firing*Lat90*Tension	1	0.267	0.267	3.76	0.089
Error	8	0.569	0.071		
Total	15	141.529			

Based on the results of the design of experiments, evaluating the response of the alternating stress of the fillet. It can be observed in Figure 8.3, that the firing load and the tension load case are the ones having the strongest effect on the fillet.

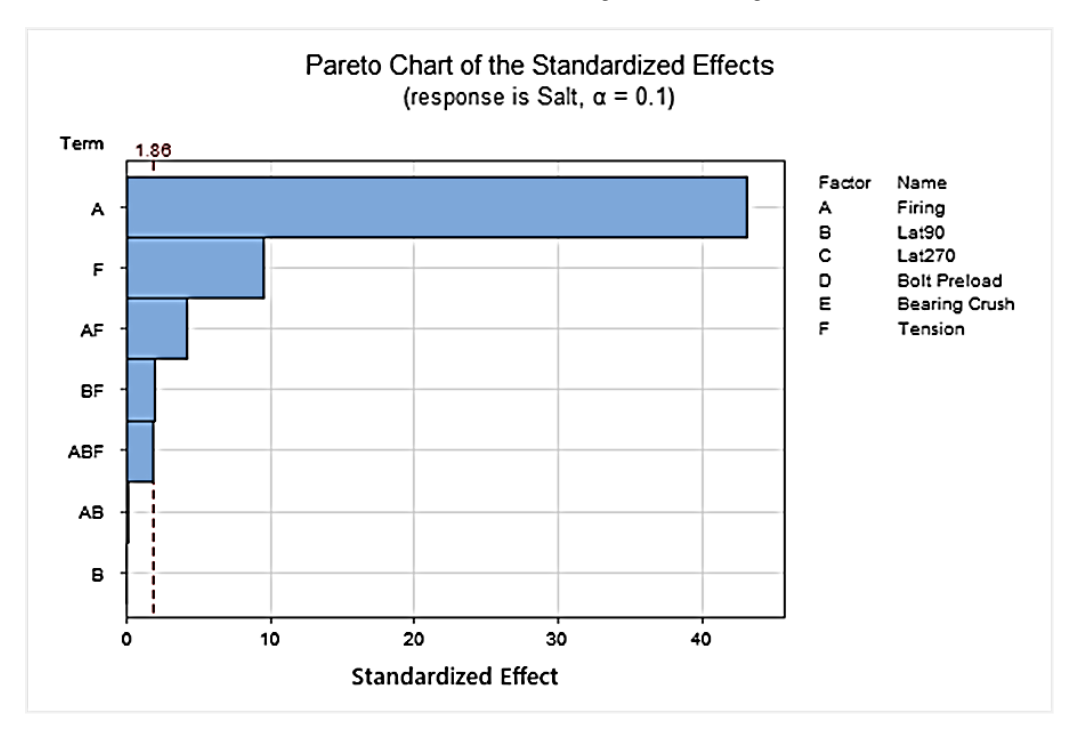


Figure 8.3 Pareto chart of effects.

Establishing them as the most important load cases to take in count for the connecting rod. It is also remarkable that the main effect plot shows as well bigger change relatively in the Figure 8.4, showing larger slopes on the firing and tension plots.

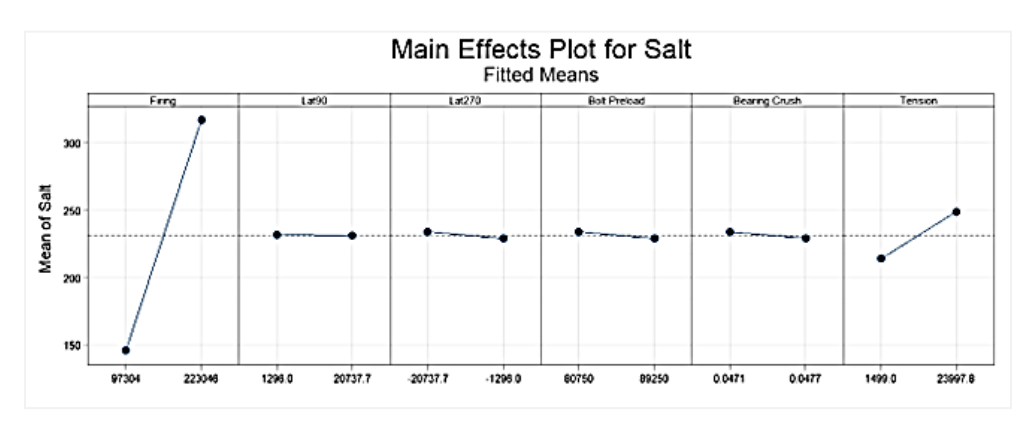
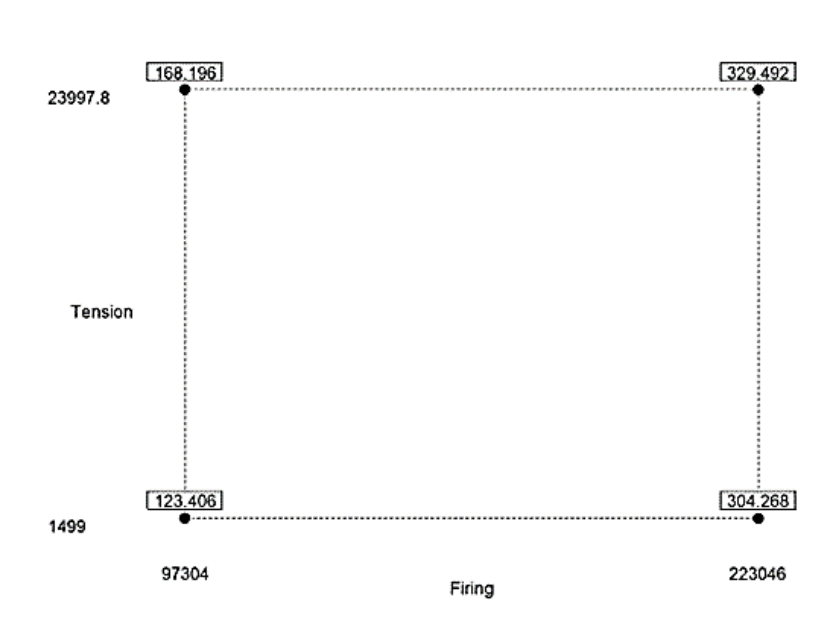


Figure 8.4 Main effects plot for alternating stress (Salt)

Lastly on the cube plot, Figure 8.5, it can be observed that the combination of the tension and firing factors have the highest effect. Which is where the alternating stress, the main enabler of fatigue failures, shows the highest value despite the low and high levels of each.



Cube Plot (fitted means) for Salt

Figure 8.5 Cube plot for alternating stress (Salt)

The results of the DoE suggest that the testing that has been done throughout the years has been representative of the load cases that affect the most the alternating stress. This also reflects that a connecting rod that can endure the tension and compression load cases, is not so likely to fail due to the bending effect of lateral accelerations.

8.3 Finite element analysis results

The results will be discussed according to the relevant load cases that have affected the connecting rod in engine operation. Supported by the DoE results, firing and tension loads have the strongest effect on the fillet. However, the assembly state will be depicted in an assembly-prestress analysis. The lateral accelerations and overspeed load case show less effect as well in the simulation.

8.3.1 Assembly state

The analysis was performed with the intent to have the effects of the stresses caused by the assembly. Which raise the stress at different locations, as can be observed at Figure 8.6 for revision 1 (A1).

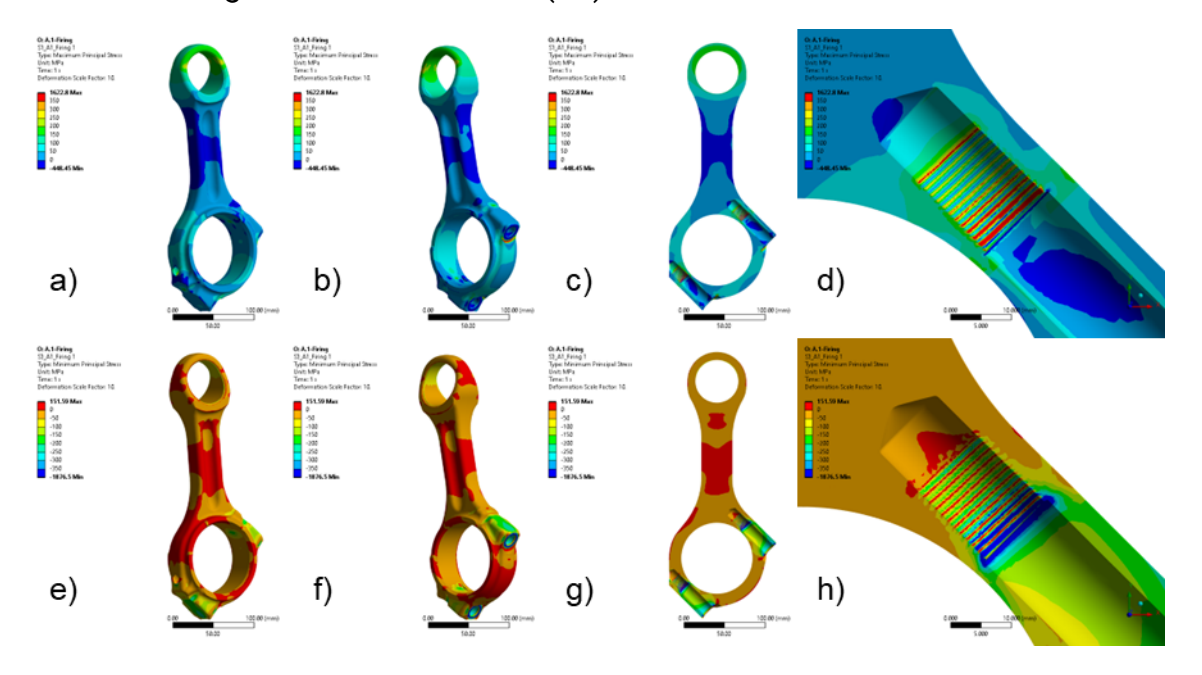


Figure 8.6 A1 Assembly Max & Min Principal Stress

The maximum principal stress plot, in MPa, highlights the locations that have a tension behavior. Although, in the minimum principal stress plot the compressive behavior is shown. The fillet radius (Figure 8.6 at b) on the cap near the bolted locations are common areas to have high maximum principal stress, now on named "S1".

The chamfer at the beginning of the thread area is mostly compressive, being shown on the minimum principal stress, now on "S3" (Figure 8.6 at d,h). The small end of the connecting rod shows as well high S1 on the outer faces, and high compression on the S3 on the inner face (Figure 8.6 at b,f). These locations show high risk of failure, since the mean stress of the locations leave small room for alternating stress that later induces a fatigue design point. However, they are beneficial to the connecting rod performance by adding stiffness to the joints.

The assembly state for revision 2 (A2) can be consulted in the appendix in Figure 0.1.

8.3.2 Peak pressure condition at 1,900 r.p.m.

Following the cycle of the engine, the firing load is expected to generate high compressive stress on the connecting rod, due to the expansion of the cylinder volume and the connecting rod pushing down the crankshaft.

It can be observed that the S3 plot on section f), g) and h) in Figure 8.7. Note that the stress is less than -350 MPa, which is more compressive than the material's endurance limit. The shank of the connecting rod is the location of highest compression.

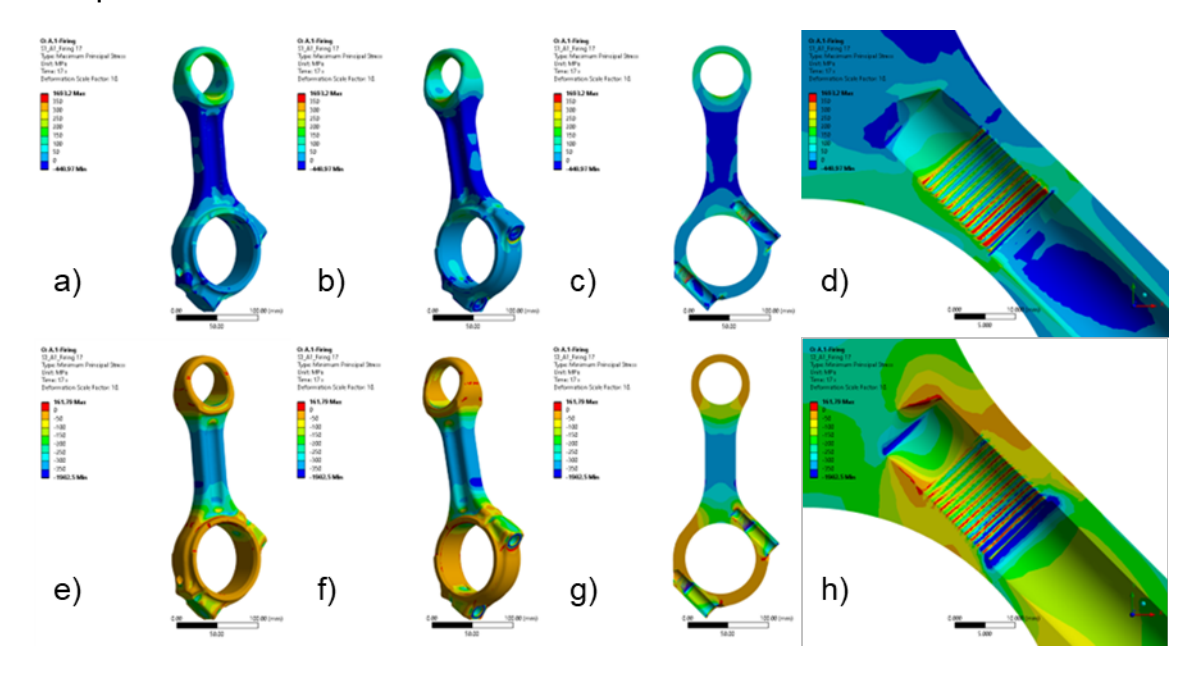


Figure 8.7 A1 Firing Max & Min Principal Stress at 1,900 r.p.m.

The peak pressure condition has the relevance for the fatigue assessment, as it represents the maximum compressive load to which the connecting rod is subjected. According to the results of the DoE it will cause the highest compressive effect on the alternating stress of the fillet detail.

The compressive load showed a minor difference between the revisions. Since the compression is mostly affecting the shank and is being diffused around the full volume of the lower portion of the connecting rod.

The stress plot for the A2 revision can be found at the appendix in Figure 0.2 for further detail. Following the next position of the connecting rod in comparison to the crank angle, are *whips* of the connecting rod at the 90° and 270° from T.D.C.

Note in Figure 8.8 and Figure 8.9 that the stress is not so different from the assembly condition (section 8.3.1) for this engine speed. Meaning that the force due to the acceleration of the reciprocating mass plays negligible effect on the component.

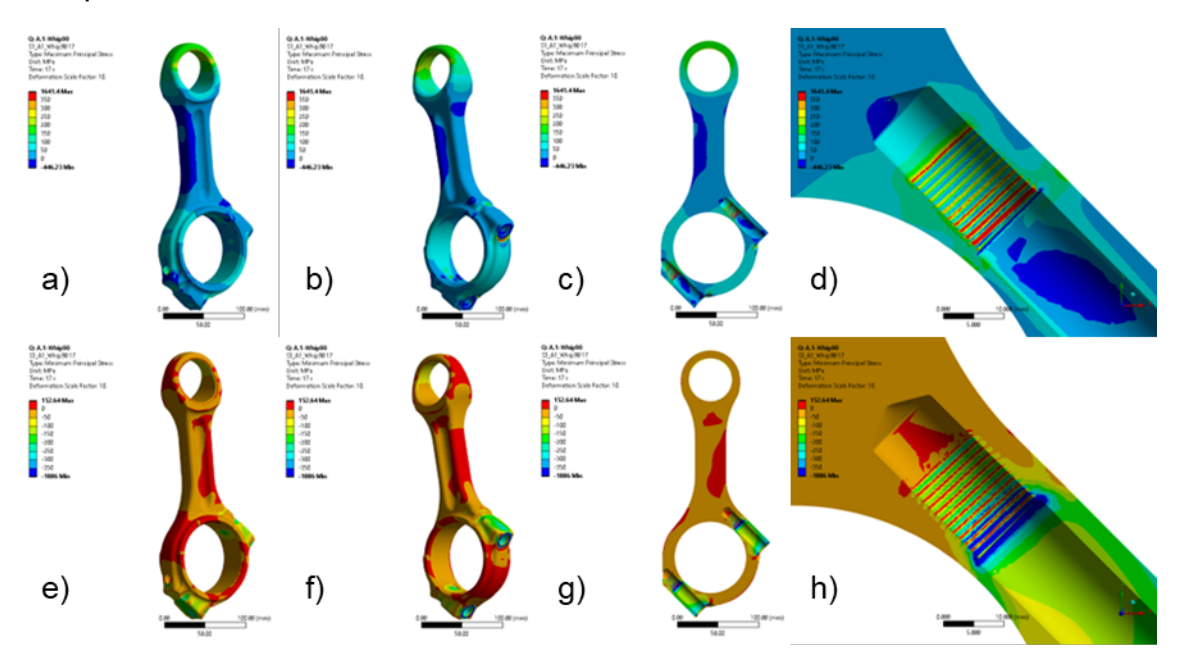


Figure 8.8 A1 Whip 90° Max & Min Principal Stress at 1,900 r.p.m.

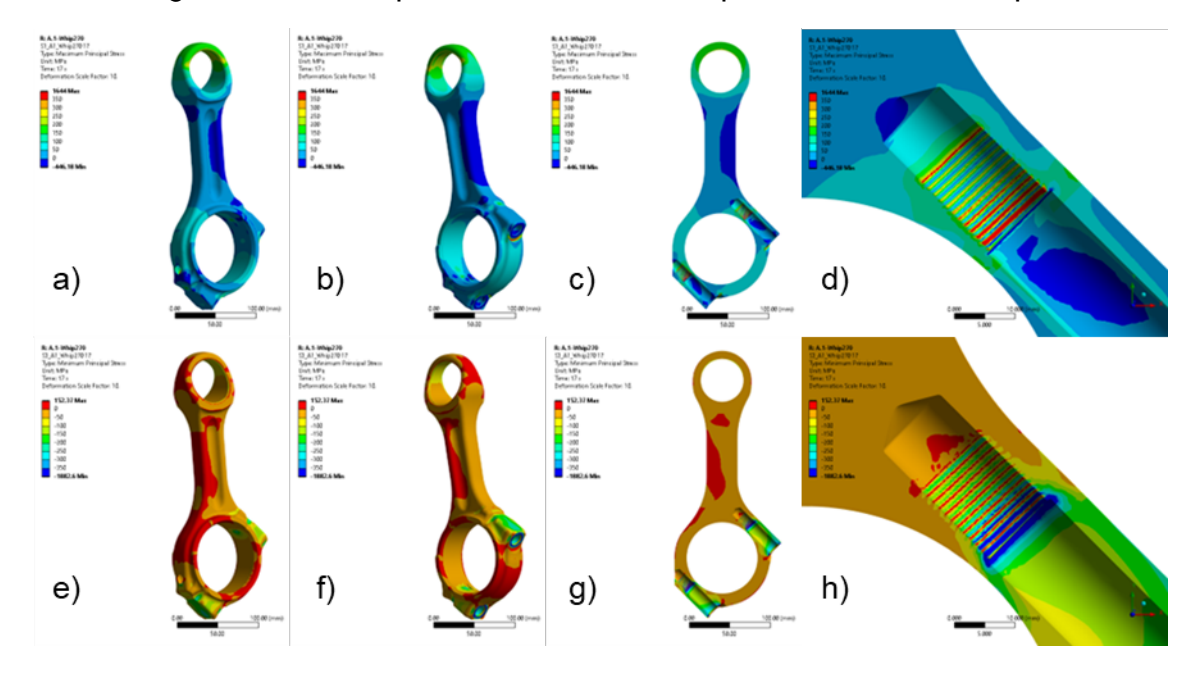


Figure 8.9 A1 Whip 270° Max & Min Principal Stress at 1,900 r.p.m.

Though, it has its added value in the simulation of the detection of an area that might get affected from the *bending of* the shank. This brings a scenario where the alternating load can generate a reversed stress that is over the endurance limit. Nonetheless, it could be determined by the simulation and the fatigue assessment plot.

For further detail on the behavior for the A2 revision, consult the appendix Figure 0.3 and Figure 0.4 for both whip load cases.

Finally, to close the cycle at the 1,900 r.p.m., Figure 8.10 in d) shows an increase on the stress in comparison to the assembly stress of approximately 50 MPa.

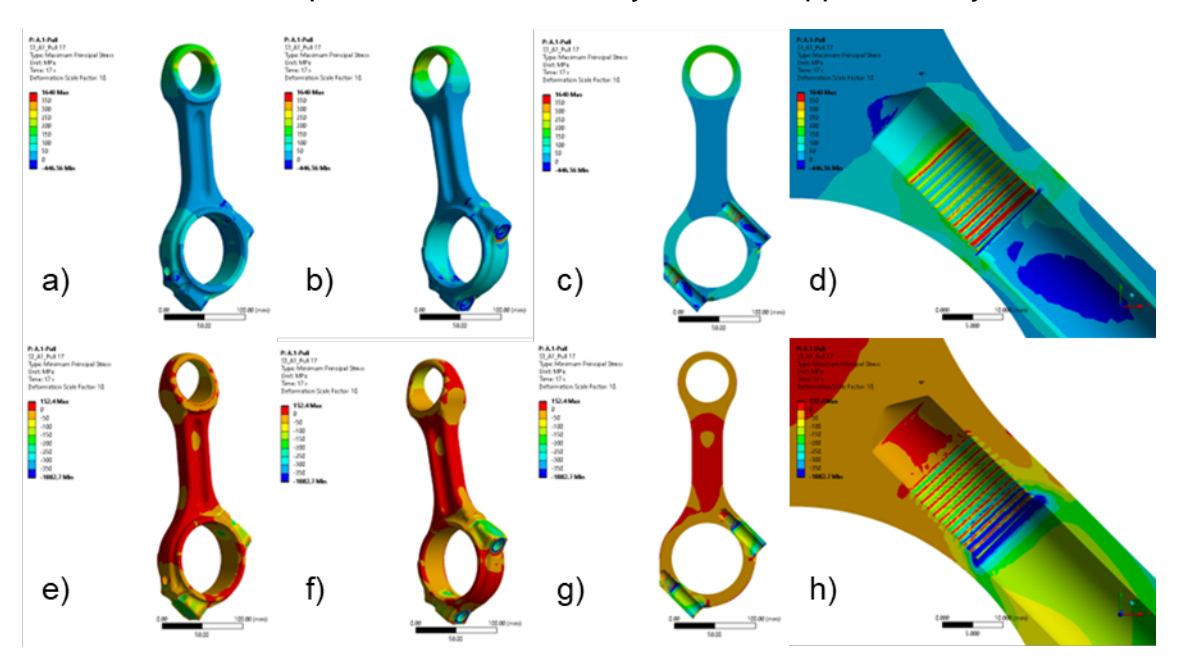


Figure 8.10 A1 Pull Max & Min Principal Stress at 1,900 r.p.m.

Despite that, it is not a high stress at this load case, but while the engine speed increases there is already a tendency to have an increase in the S1. For further details on revision A2, consult the appendix in Figure 0.5.

8.3.3 Full load at rated speed at 2,400 r.p.m.

The firing load case at full load rated speed condition for the connecting rod, has a decrease at the force of approximately 30kN. Which continues to be noted on the S3 plots of the Figure 8.11. Note that as similar to the compression on peak pressure condition, there is high compression on the fillet area.

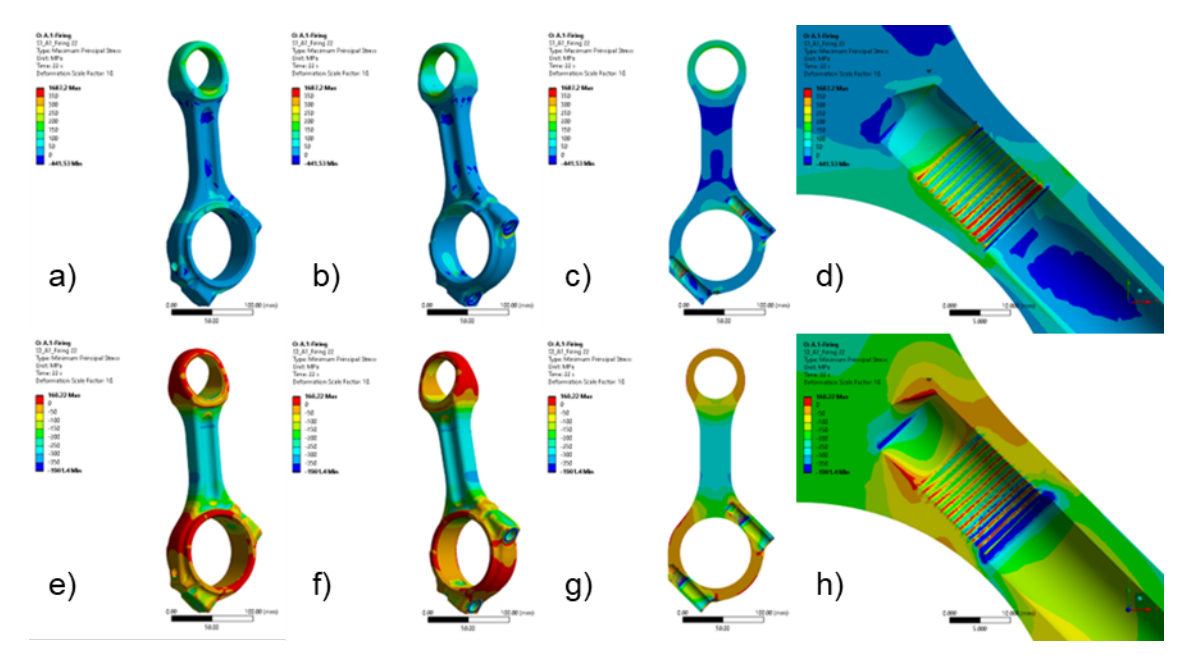


Figure 8.11 A1 Firing Max & Min Principal Stress at 2,400 r.p.m.

The lateral acceleration load cases share a similar behavior as the peak pressure case, not showing a high stress alternation. In Figure 8.12 and Figure 8.13, it shows little increase in the S1 in comparison to the assembly condition.

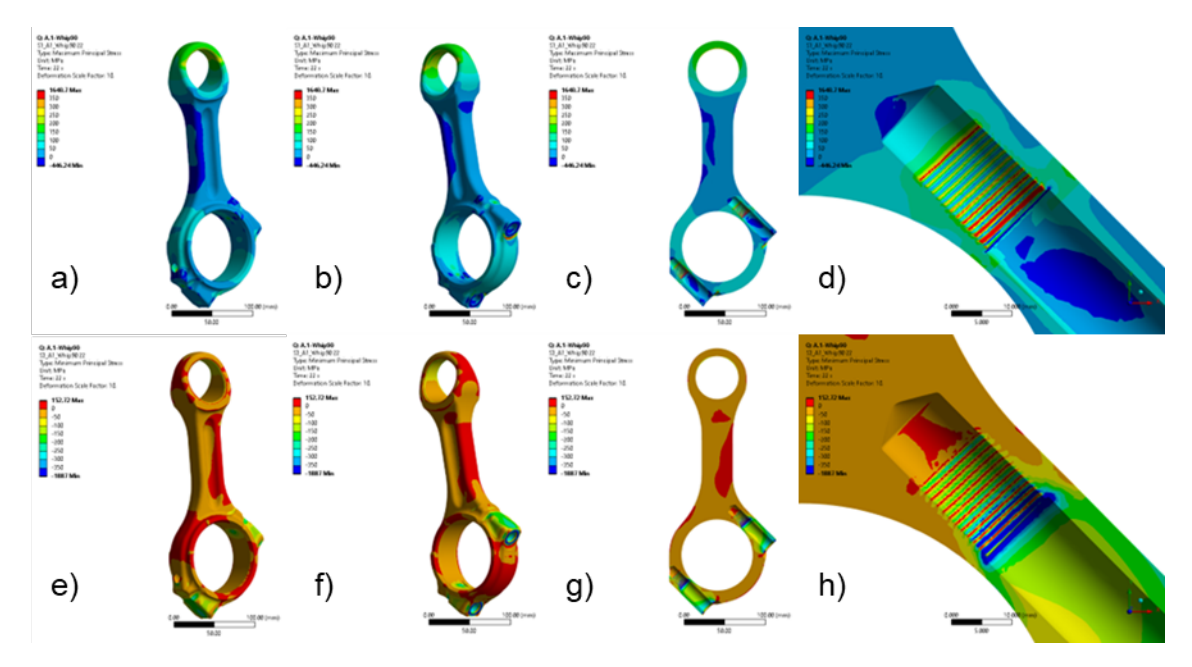


Figure 8.12 A1 Whip 90° Max & Min Principal Stress at 2,400 r.p.m.

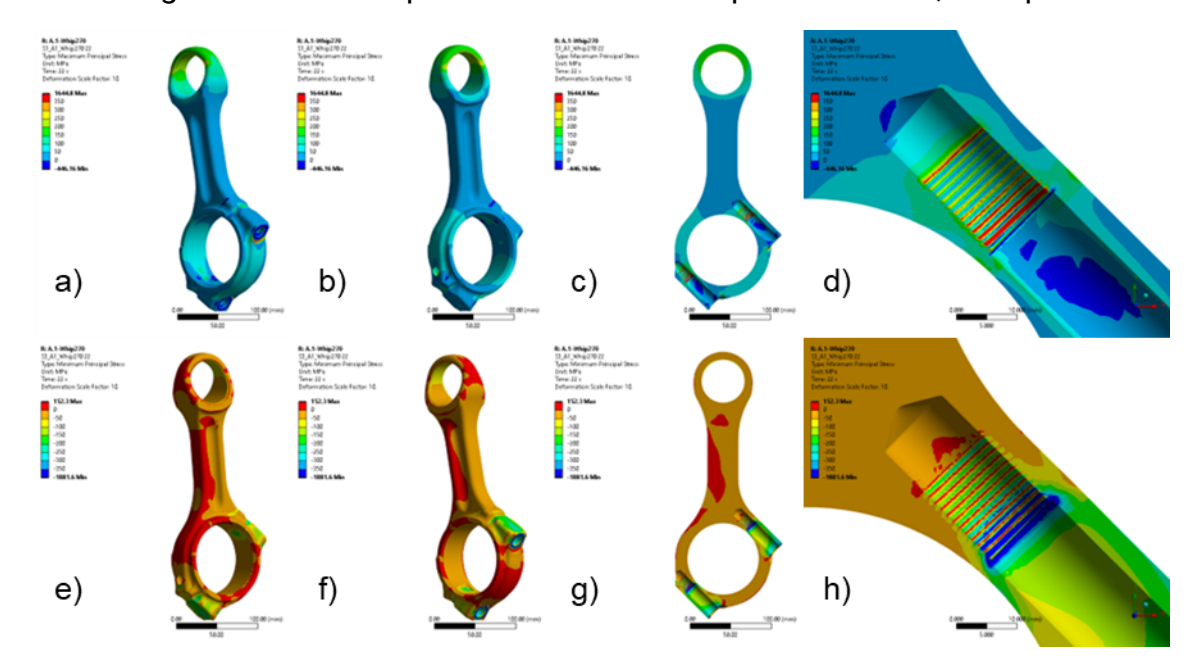


Figure 8.13 A1 Whip270° Max & Min Principal Stress at 2,400 r.p.m.

Further details for revision A2 consult the appendix Figure 0.7 and Figure 0.8

Moving on to the pull load case, in the Figure 8.14 for A1, note that the stress changes proportionally to the results shown at section 8.3.2. Showing a consistency with linear increase for the inertial load cases, in proportion to the increase of the accelerations at different crank angles.

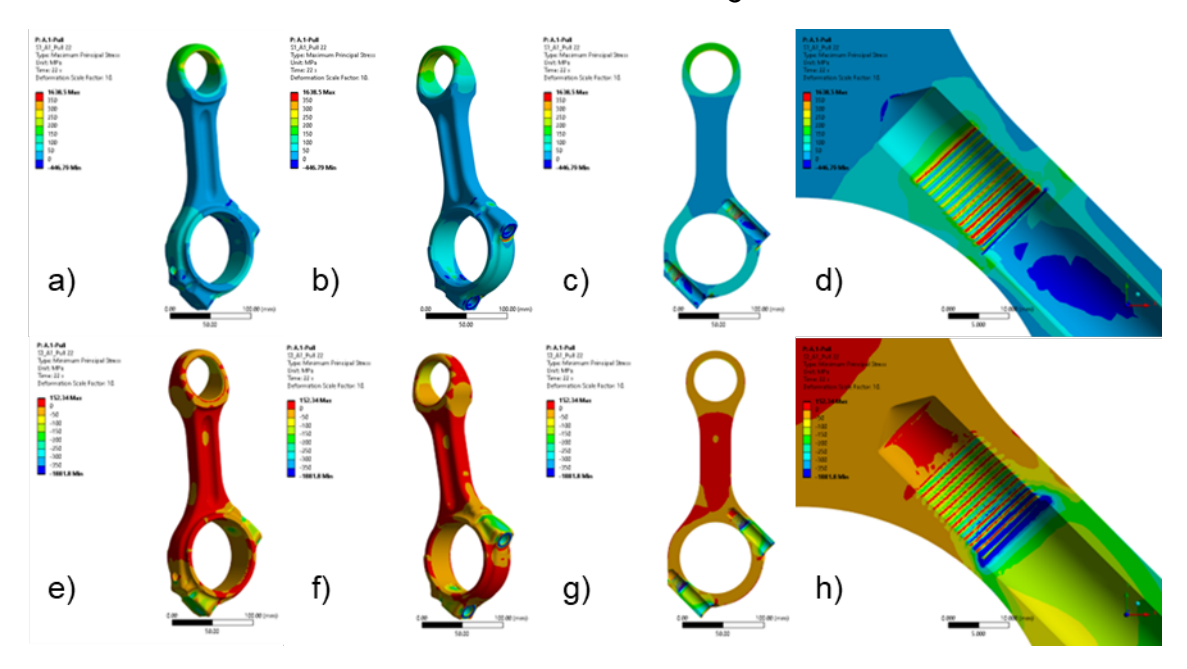


Figure 8.14 A1 Pull Max & Min Principal Stress at 2,400 r.p.m.

For the engine operating conditions, it can be noted that the stress alternation between firing and pull load cases is the highest. The lateral accelerations can indicate when the connecting rod is having a weak cross section that will end on a buckling or bending failure.

8.3.4 Overspeed

The engine overspeed condition does not have a firing event discarding the combustion forces. In the Figure 8.15 and Figure 8.16 at a) and c) can be noted a trend in the increase of the S1 and more compression in S3.

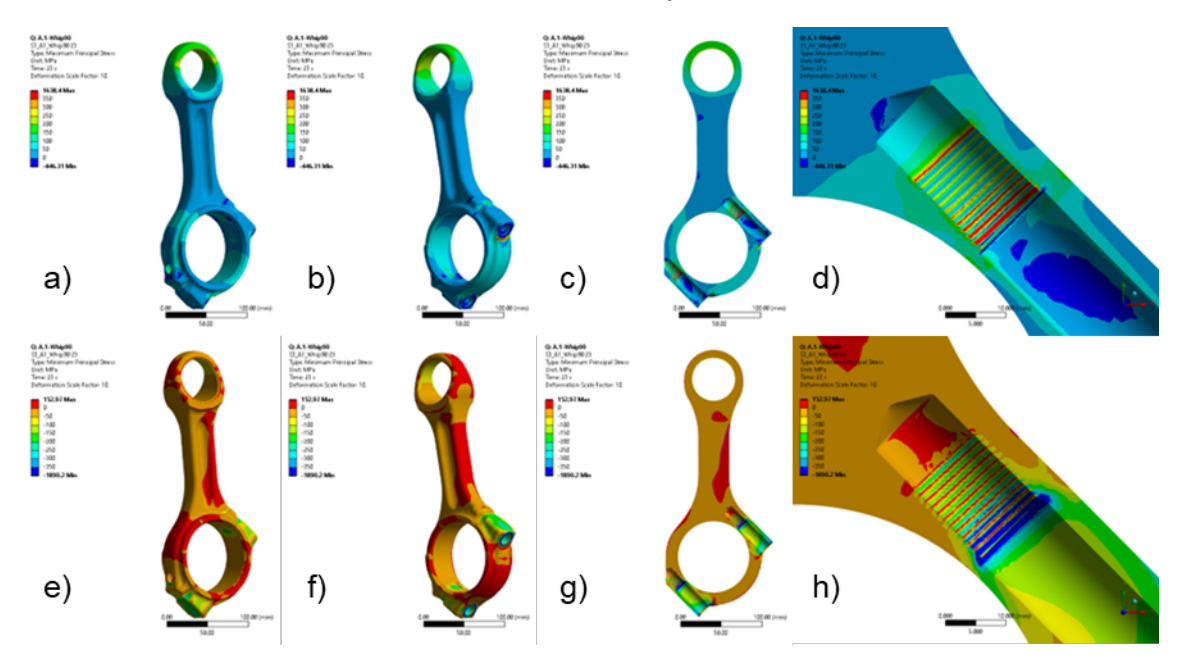


Figure 8.15 A1 Whip 90° Max & Min Principal Stress at 3,600 r.p.m.

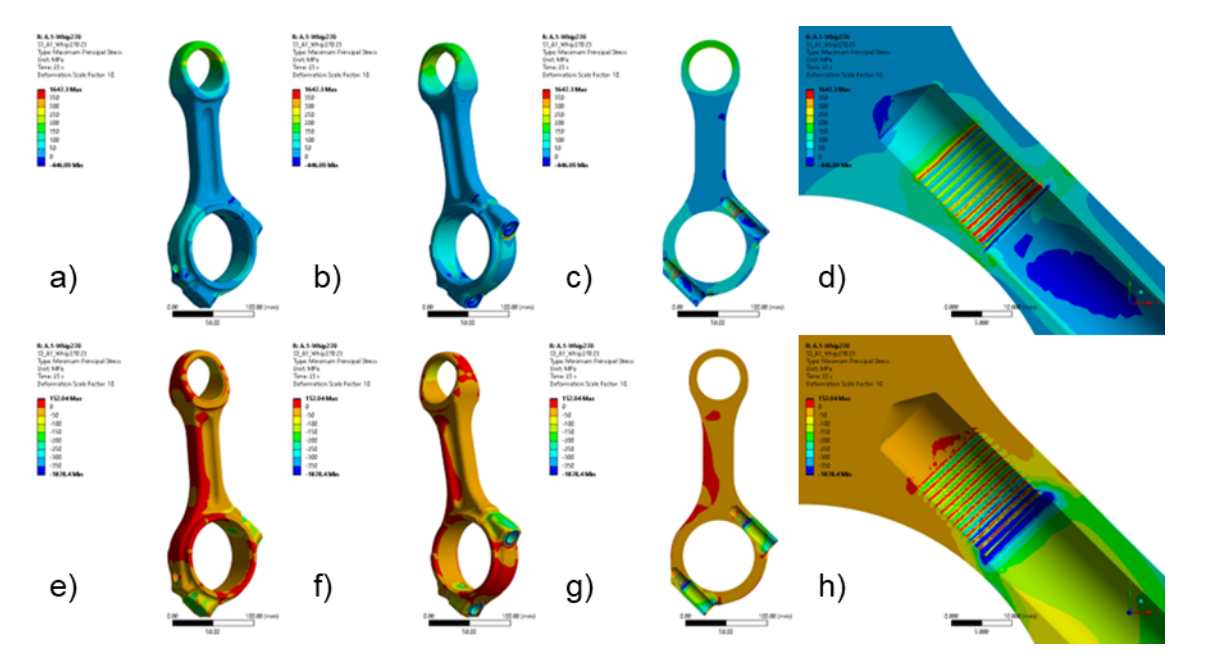


Figure 8.16 A1 Whip 270° Max & Min Principal Stress at 3,600 r.p.m.

This means that there is a tension and compression due to the lateral acceleration affecting the connecting rod. This load case allows to observe the critical locations along the *long leg* of the connecting rod where a fatigue crack can occur.

Further detail for revision A2 can be consulted in the appendix in Figure 0.10 and Figure 0.11.

The pull load case at 3,600 r.p.m. generates a high tensile stress concentration at the fillet area as can be observed in Figure 8.17 at d). This will increase the alternating stress between the firing load at peak pressure in section 8.3.2 and this pull load.

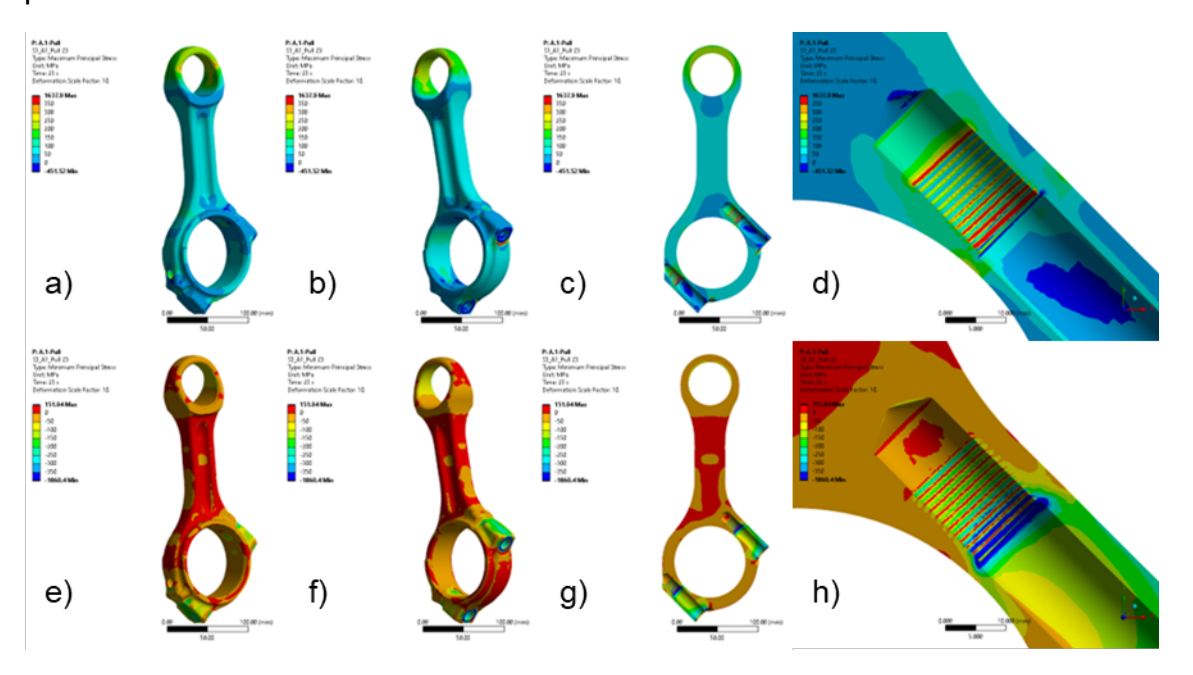


Figure 8.17 A1 Pull Max & Min Principal Stress at 3,600 r.p.m.

Now it can be identified that the physical testing shows the relationship between the firing and pull load case, which will subject the connecting rod to the most extreme conditions that can be found in regular engine operations and an overspeed condition.

The overspeed condition cannot be controlled, since it happens due to the nature of the usage of the vehicle, whereas the firing pressure can be controlled via a governor.

The correction performed to the revision A2, with a bigger fillet radius, has a clear positive effect on this load case. Note in Figure 8.18 at d), that the tension at the

fillet is at least 100 MPa less. This reduces the alternating stress and improves the fatigue life.

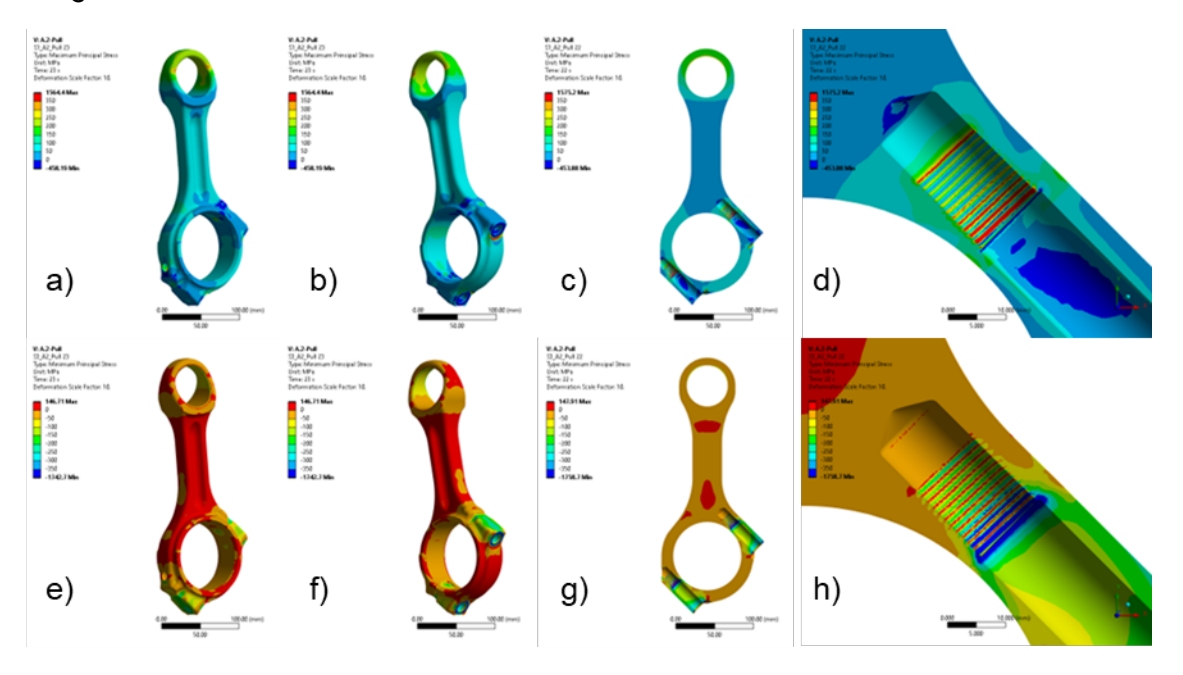


Figure 8.18 A2 Pull Max & Min Principal Stress at 3,600 r.p.m.

Observing the results of the Figure 8.17 and Figure 8.18, it can be noted that the fillet stress on A1 is at least 50 MPa in comparison to A2. Recalling the results obtained from the DoE, the pull load case was determinant in the alternating stress. Here it also backs up, that an overspeed condition will generate high tensile stress that will be *reversed* by the highest firing load.

8.4 Fatigue assessment results

The fatigue assessment was conducted with the Fe-Safe software, where different kt values were used according to the surface roughness of the component. The mean stress correction technique used was from Goodman to allow some conservative approach to secure product development. The Neuber stress correction was also used, since the model was running on linear properties only.

Two different scenarios were considered. The regular operating condition of the engine, according to the rated engine's speed and a second condition with an engine overspeed. Despite that an overspeed case is rarely seen, it can cause heavy damage on the connecting rod. Also, as observed on the DoE, the tension generated can increase the alternating stress and hence promote a fatigue crack. Overall, it can be observed that the connecting rod would have been working on normal engine conditions, as shown in Figure 8.19 and Figure 8.20, where A1 is marginally reaching a 1 in terms of safety factor (FoS).

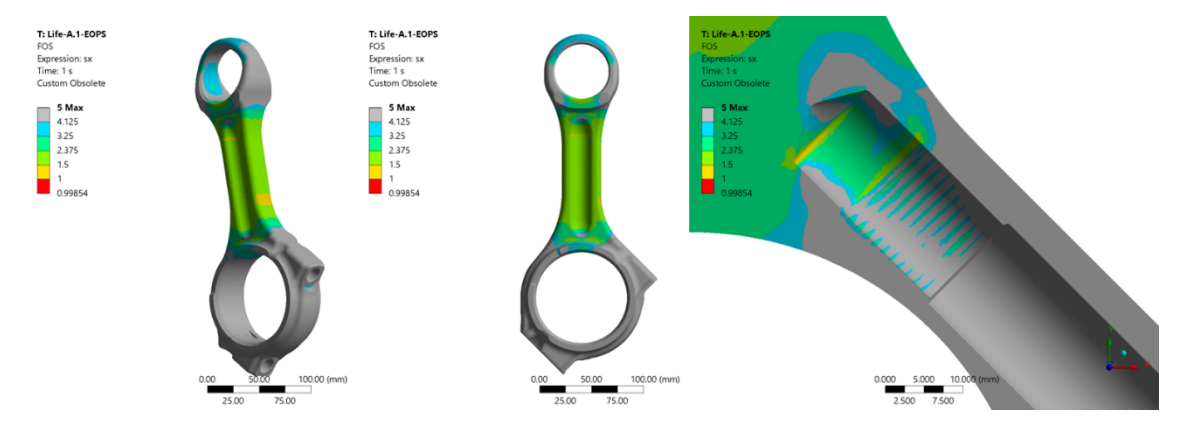


Figure 8.19 Safety factor A1 - Engine operation.

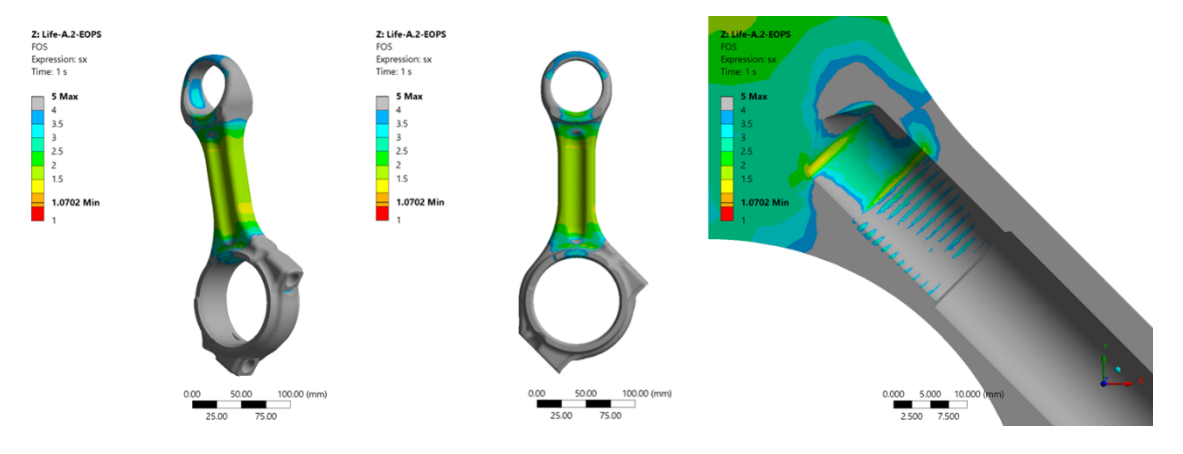


Figure 8.20 Safety factor A2 – Engine operation.

When adding a the overspeed condition to the connecting rods, it can be observed that both decreased their FoS drastically as shown on Table 8-5. Note the results as well on Figure 8.21 and Figure 8.22, where the overspeed affects the shank of the components as well. There was found a contact singularity on the threaded area to be ignored for the analysis, showing the low FoS at the thread end.

Table 8-5 Safety factor (FoS) on fillet.

Load Case	A.1	A.2
Engine Operation	0.99	1.23
Engine Operation + Overspeed	0.83	1.01

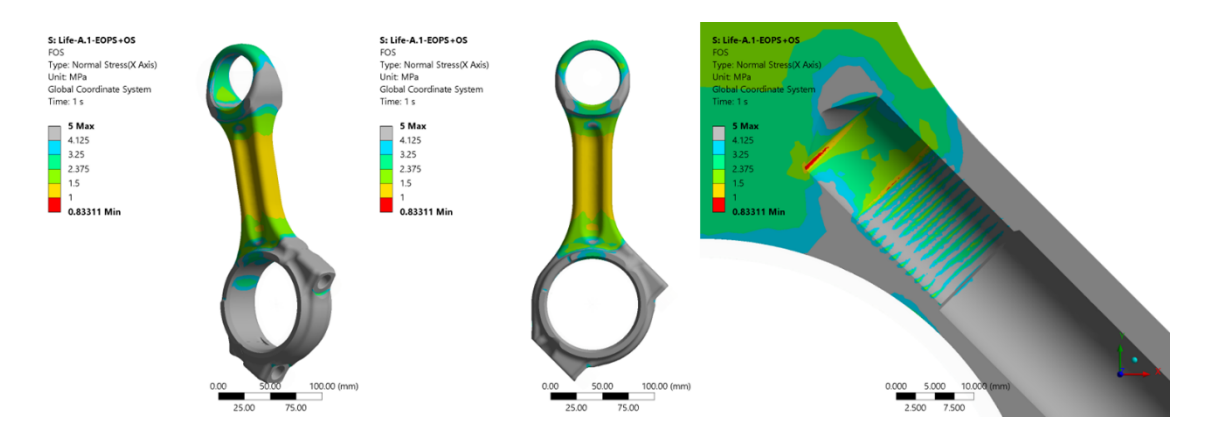


Figure 8.21 Safety factor A1 – Engine operation + Overspeed.

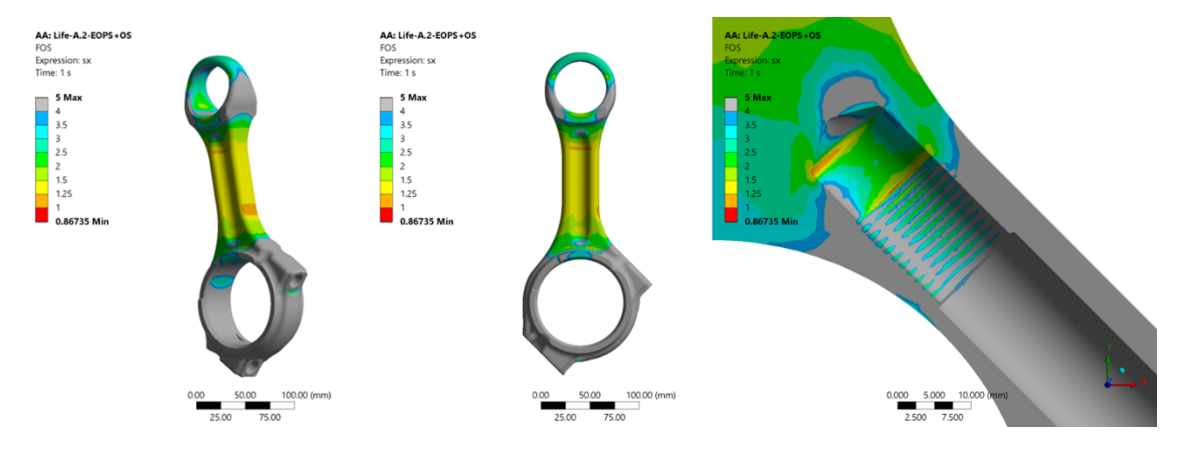


Figure 8.22 Safety factor A2 - Engine operation + Overspeed.

The connecting rod used for testing showed marginal results almost achieving the criteria, however it ran short of having a reliable product. Once the corrective action was taken, by increasing the fillet radius it can be observed the change in the

safety factor. On Figure 8.23 and Figure 8.24, it can be observed the safety factor distribution across the fillet for normal engine operation with no overspeed.

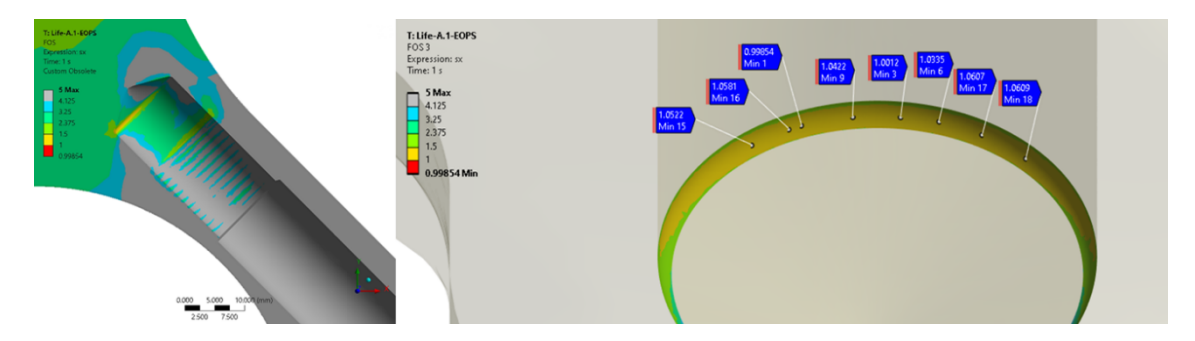


Figure 8.23 Revision 1 at fillet, FoS = 0.99

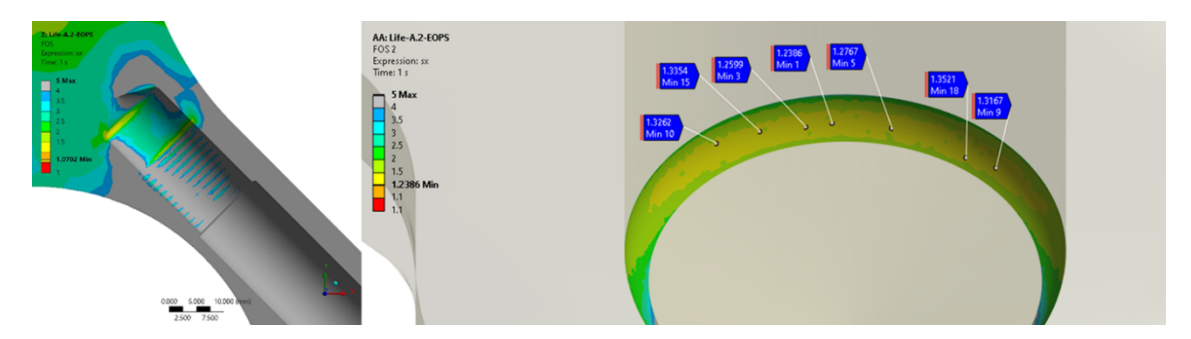


Figure 8.24 Revision 2, FoS = 1.23

As observed in the previous results, it can be noted that the surface finish in combination with the known loads can change the outcome of the results. The location detected on the fillet is one sample of the most common performance inconsistency. At this point, the FoS not reaching the target of 1, leaves the accuracy of the method on the edge. While doing the correction, and rerunning the study showed a clear difference on the criteria.

Finally, the testing technique will cover the highest factors that affect the connecting rod. The high compressive forces due to the combustion, and the high pull force due to the return at T.D.C. due to the crankshaft accelerations. Nonetheless, the bending due to the lateral acceleration is not represented through the test but is captured in the simulation. This will improve the capability to detect and prevent a failure mode due to the bending and combination of buckling of the connecting rod in the engine.

Chapter 9 Conclusions & perspectives

The scope of this work was based on the need for a virtual validation procedure that can demonstrate a connection between physical testing and simulation. Decrease the timeframe to release and to optimize the performance, reduce emissions to meet the demands of the market and regulations across the globe.

The limitation of the study is that it is based on classic mechanics, and dynamics that do not take into account some of the new approaches of integrating elastohydrodynamic loads. Which can be higher than the classical mechanics. However, the connection between testing, design and analysis is still under development in the industry to determine how big this gap is.

As I previously stated, safety factors are introduced and studied depending on the component and its functional intent. The design target is to comply with the requirements of weight and performance and strongly related to the durability of the useful life.

From the general objective, a safety factor was established from the design perspective. According to the simulation, the target with the present boundary conditions will be around 1.07. However, this value is constrained to ideal manufacturing situations.

To achieve this target, an engine with development point by design that is complaint with the emissions regulations of the latest generation was selected. The quality assurance survey concluded that there are enhancements due to machining, boring, more adequate material or tolerance specifications.

The characterization for the material was conducted prior to the start of this project, having available the fatigue properties as well as the performance and torque curves.

The simulations were performed capturing the full performance curve. It was studied with a DoE which are the factors that most affect the connecting rod. The results concluded that the current methods are adequate to have the highest effects captured in testing.

With the simulation strategy I found that there are still advantages in performing inertial lateral load cases. The bending of the connecting rod, if given, will not be covered by the testing activities.

Another area that is reflected in the simulation, is the assembly stress that is not measured in the testing. Having the effect captured in the simulation allows to detect the residual or initial stresses that affect the fatigue safety factor either positively or negatively.

In order to cover the deviation from standards that can increase due to the manufacturing, it is recommended to increase the safety factor. Depending on the application, based on the design criteria the FoS can have a variation from 0.2 in conditions where materials are reliable and environmental conditions are not severe. So, I recommend to stretch the FoS to 1.2 to give an additional margin for useful life to the components.

The nature of the performance of the connecting rods makes them a highly compliant part of the engine. Where an unexpected outcome results in a full engine replacement. Increasing the FoS can lead to more expensive connecting rods, but low FoS can lead to unmet expectations in the long term.

Bibliography

- [1] M. Grosso *et al.*, "How will vehicle automation and electrification affect the automotive maintenance, repair sector?," *Transp Res Interdiscip Perspect*, vol. 12, p. 100495, Dec. 2021, doi: 10.1016/J.TRIP.2021.100495.
- [2] R. C. Dorf, *The engineering handbook: CD-ROM version*. CRC Press, 1998.
- [3] J. Göös, A. Leppänen, A. Mäntylä, and T. Frondelius, "Large Bore Connecting Rod Simulations," *Rakenteiden Mekaniikka*, vol. 50, no. 3, 2017, doi: 10.23998/rm.64658.
- [4] W. W. Pulkrabek, *Engineering Fundamentals of the Internal Combustion Engine*. New Jersey: Pearson Prentice Hall, 2004.
- [5] N. Azeem *et al.*, "Experimental study of cycle-by-cycle variations in a spark ignition internal combustion engine fueled with hydrogen," *Int J Hydrogen Energy*, vol. 60, pp. 1224–1238, Mar. 2024, doi: 10.1016/j.ijhydene.2024.02.182.
- [6] H. Söyler, M. K. Balki, and C. Sayin, "The impact of injection timing and pressure on a CRDI engine's combustion characteristics," *Journal of Engineering Research*, Feb. 2024, doi: 10.1016/J.JER.2024.02.015.
- [7] F. Leach, G. Kalghatgi, R. Stone, and P. Miles, "The scope for improving the efficiency and environmental impact of internal combustion engines," *Transportation Engineering*, vol. 1, p. 100005, Jun. 2020, doi: 10.1016/J.TRENG.2020.100005.
- [8] Ö. Can and Ö. Çetin, "Potential use of graphene oxide as an engine oil additive for energy savings in a diesel engine," *Engineering Science and Technology, an International Journal*, vol. 48, p. 101567, Dec. 2023, doi: 10.1016/J.JESTCH.2023.101567.
- [9] M. Oikawa, Y. Kojiya, R. Sato, K. Goma, Y. Takagi, and Y. Mihara, "Effect of supercharging on improving thermal efficiency and modifying combustion characteristics in lean-burn direct-injection near-zero-emission hydrogen engines," *Int J Hydrogen Energy*, vol. 47, no. 2, pp. 1319–1327, Jan. 2022, doi: 10.1016/j.ijhydene.2021.10.061.
- [10] Garrett Motion, "VNT Turbochargers," https://www.garrettmotion.com/es/turbocharger-technology/how-a-turboworks/broadest-turbo-range/vnt-turbochargers/.

- [11] R. S. Khurni, J. K. Gupta, and S. Chand, *Textbook of Machine Design R.S. Khurmi, J.K. Gupta, S.Chand.* 2005.
- [12] Alma. Hillier and V. A. W. (Victor A. W. Hillier, *Hillier's fundamentals of motor vehicle technology. Book 1.* Nelson Thornes, 2011.
- [13] Deere & Co., "7R Power & Efficiency," https://www.deere.ca/en/tractors/row-crop-tractors/row-crop-7-family/engines-transmissions/.
- [14] C. Fayette Taylor, *The Internal-Combustion Engine in Theory and Practice*, *Volume 1*, Second edition., vol. Volume 1. Massachusetts: The M.I.T. Press, 1985.
- [15] INGENIERIA Y MECANICA AUTOMOTRIZ, "¿Qué son las Cadenas de Transmisión y cómo se diseñan para la industria Automotriz?," https://www.kwikfit.com/assets/kwikfit/engine_with_flywheel.jpeg.
- [16] J. L. Meriam, L. G. Kraige, and J. N. Bolton, *Engineering Mechanics : Dynamics*, Eight edtion., vol. Volume 8. Wiley, 2015.
- [17] B. Kuldeep *et al.*, "A novel composite connecting rod: study on mechanical and dynamic behaviour through experimental and finite element approach," *Composites Part C: Open Access*, vol. 12, p. 100413, Oct. 2023, doi: 10.1016/J.JCOMC.2023.100413.
- [18] P. Dempsey, *Troubleshooting and Repairing Diesel Engines*, Fourth. Mcgraw-Hill, 2008. doi: 10.1036/0071493719.
- [19] Z. Gu, S. Yang, S. Ku, Y. Zhao, and X. Dai, "Fracture splitting technology of automobile engine connecting rod," *International Journal of Advanced Manufacturing Technology*, vol. 25, no. 9–10, pp. 883–887, May 2005, doi: 10.1007/S00170-003-2022-2.
- [20] G. Ellwood. Dieter and D. J. Bacon, *Mechanical metallurgy*. McGraw-Hill, 1988.
- [21] Wilmar Veiga Vasques Jr, "For Clean-Cut Fracture Splitting: Monitor Cutting Processes with Kistler," https://www.linkedin.com/pulse/clean-cut-fracture-splitting-monitor-cutting-kistler-wilmar-vasques/.
- [22] J. A. Collins and H. Busby, *Mechanical Design of Machine Elements and Machines: A Failure Prevention Perspective*, 2nd ed. John Wiley & Sons, 2010.
- [23] P. Hou and W. Zhang, "Bolt Coupling Structure of Contact Stress and the Influence Factors of Joint Stiffness Based on Finite Element Method," *Procedia*

- Comput Sci, vol. 208, pp. 658-665, Jan. 2022, doi: 10.1016/J.PROCS.2022.10.090.
- [24] V. Mangeruga, S. G. Barbieri, M. Giacopini, L. Bianco, A. Ferretti, and M. Mazziotta, "Analysis of the tribological behaviour of the lubricated contacts of a connecting rod equipped with a direct pin oiling gallery," *Tribol Int*, vol. 198, p. 109851, Oct. 2024, doi: 10.1016/J.TRIBOINT.2024.109851.
- [25] A. E. Anderson et al., Friction, Lubrication, and Wear Technology, vol. 18. 1992.
- [26] M. M. Khonsari and E. R. Booser, *Applied Tribology: Bearing Design and Lubrication, 3rd Edition,* Third. John Wiley & Sons Ltd, 2017.
- [27] J. FRÉNE and T. CICONE, "Friction in Lubricated Contacts," *Handbook of Materials Behavior Models*, pp. 760–767, Jan. 2001, doi: 10.1016/B978-012443341-0/50076-4.
- [28] R. D. Sulamet-Ariobimo, M. Fadhlan, Y. Oktaviano, T. Sukarnoto, Y. Mujalis, and A. Witonohadi, "The effects of I-Beam thickness to microstructure and compression load of thin wall ductile iron connecting rod," *International Journal of Lightweight Materials and Manufacture*, vol. 6, no. 3, pp. 392–404, Sep. 2023, doi: 10.1016/J.IJLMM.2023.01.001.
- [29] B. Kuldeep *et al.*, "A novel composite connecting rod: study on mechanical and dynamic behaviour through experimental and finite element approach," *Composites Part C: Open Access*, vol. 12, p. 100413, Oct. 2023, doi: 10.1016/J.JCOMC.2023.100413.
- [30] M. Sri Vidhya and K. V Merlyn Christina, "Fatigue Life, Fatigue Damage, Fatigue Factor of Safety, Fatigue Sensitivity, Biaxiality Indication and Equivalent Stress of a Radial Connecting Rod," *International Research Journal of Engineering and Technology*, 2020, [Online]. Available: www.irjet.net
- [31] T. Nicholas, *High Cycle Fatigue: A Mechanics of Materials Perspective*, First. Elsevier, 2006.
- [32] H. Liu, F. Pisanò, H. P. Jostad, and N. Sivasithamparam, "Impact of cyclic strain accumulation on the tilting behaviour of monopiles in sand: An assessment of the Miner's rule based on SANISAND-MS 3D FE modelling," *Ocean Engineering*, vol. 250, p. 110579, Apr. 2022, doi: 10.1016/J.OCEANENG.2022.110579.
- [33] E. Maleki, S. Bagherifard, and M. Guagliano, "Correlation of residual stress, hardness and surface roughness with crack initiation and fatigue strength of

- surface treated additive manufactured AlSi10Mg: Experimental and machine learning approaches," *Journal of Materials Research and Technology*, vol. 24, pp. 3265–3283, May 2023, doi: 10.1016/J.JMRT.2023.03.193.
- [34] E. Oberg and C. J. McCauley, *Machinery's handbook: a reference book for the mechanical engineer, designer, manufacturing engineer, draftsman, toolmaker, and machinist,* 29th ed. New York: Industrial Press, 2012.
- [35] Dassault Systemes, "fe-safe 2021 User Guide." 2020.
- [36] S. Cecchel *et al.*, "Fatigue testing and end of life investigation of a topology optimized connecting rod fabricated via selective laser melting," *Int J Fatigue*, vol. 164, p. 107134, Nov. 2022, doi: 10.1016/J.IJFATIGUE.2022.107134.
- [37] SincoTec, "Connecting rods | Sincotec," https://www.sincotec.de/tested-components/connecting-rods/?lang=en.
- [38] L. A. Román-Ramírez and J. Marco, "Design of experiments applied to lithiumion batteries: A literature review," *Appl Energy*, vol. 320, p. 119305, Aug. 2022, doi: 10.1016/J.APENERGY.2022.119305.
- [39] A. I. Al-Zoubi, T. M. Alkhamis, and H. A. Alzoubi, "Optimized biogas production from poultry manure with respect to pH, C/N, and temperature," *Results in Engineering*, vol. 22, p. 102040, Jun. 2024, doi: 10.1016/J.RINENG.2024.102040.
- [40] S. Beg and M. Rahman, "Design of experiments application for analytical method development," *Handbook of Analytical Quality by Design*, pp. 191–197, Jan. 2021, doi: 10.1016/B978-0-12-820332-3.00011-X.
- [41] D. C. Montgomery, *Design and analysis of experiments*, 8th ed. Wiley and Sons, 2013.
- [42] Minitab, "Getting Started with Minitab Statistical Software." 2021.
- [43] A. Jankovic, G. Chaudhary, and F. Goia, "Designing the design of experiments (DOE) An investigation on the influence of different factorial designs on the characterization of complex systems," *Energy Build*, vol. 250, p. 111298, Nov. 2021, doi: 10.1016/J.ENBUILD.2021.111298.
- [44] M. R. Rashid, S. K. Ghosh, M. F. Bin Alam, and M. F. Rahman, "A fuzzy multicriteria model with Pareto analysis for prioritizing sustainable supply chain barriers in the textile industry: Evidence from an emerging economy," *Sustainable*

- *Operations and Computers*, vol. 5, pp. 29–40, Jan. 2024, doi: 10.1016/J.SUSOC.2023.11.002.
- [45] E. Madenci and I. Guven, *The finite element method and applications in engineering using ANSYS®*, *second edition*. Springer US, 2015. doi: 10.1007/978-1-4899-7550-8.
- [46] I. Koutromanos, *Fundamentals of Finite Element Analysis*, First. New Jersey: John Wiley & Sons, 2018.
- [47] Y. Feng, J. A. A. Mena, H. Yang, H. Wang, and B. Jeremić, "Domain specific language for finite element modeling and simulation," *Advances in Engineering Software*, vol. 193, Jul. 2024, doi: 10.1016/j.advengsoft.2024.103666.
- [48] F. Rieg, R. Hackenschmidt, and B. Alber-Laukant, *Finite element analysis for engineers: basics and practical applications with Z88Aurora*. Munich: Haser-Fachbuch, 2014.
- [49] S. Bhavikatti, *Finite Element Analysis*. New Dehli: New Age International Publishers, 2005.
- [50] M. Saranik, L. Jézéquel, and D. Lenoir, "Experimental and numerical study for fatigue life prediction of bolted connection," in *Procedia Engineering*, Elsevier Ltd, 2013, pp. 354–368. doi: 10.1016/j.proeng.2013.12.090.
- [51] T. W. I. Kuan and J. Szmelter, "Explicit and implicit large eddy simulations of variable-density low-speed flows," *J Comput Phys*, vol. 499, p. 112715, Feb. 2024, doi: 10.1016/J.JCP.2023.112715.
- [52] G. Markou and M. AlHamaydeh, "Computationally-efficient high-fidelity nonlinear FEA of seismically isolated post-tensioned RC bridges," *Structures*, vol. 60, p. 105816, Feb. 2024, doi: 10.1016/J.ISTRUC.2023.105816.

Appendix

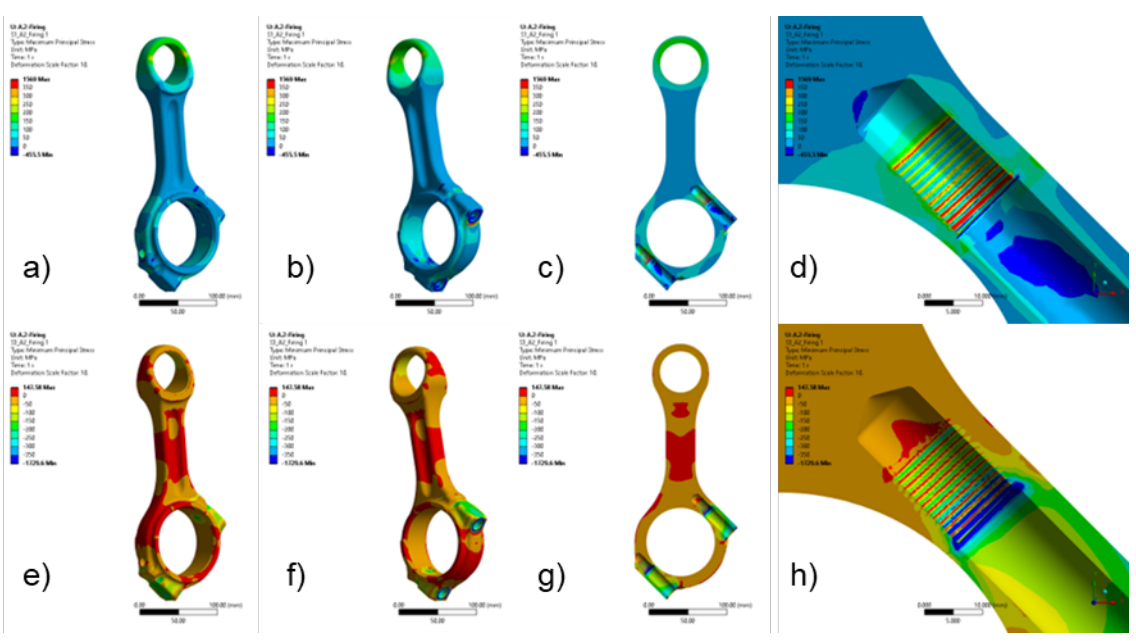


Figure 0.1 A2 Assembly Max & Min Principal Stress

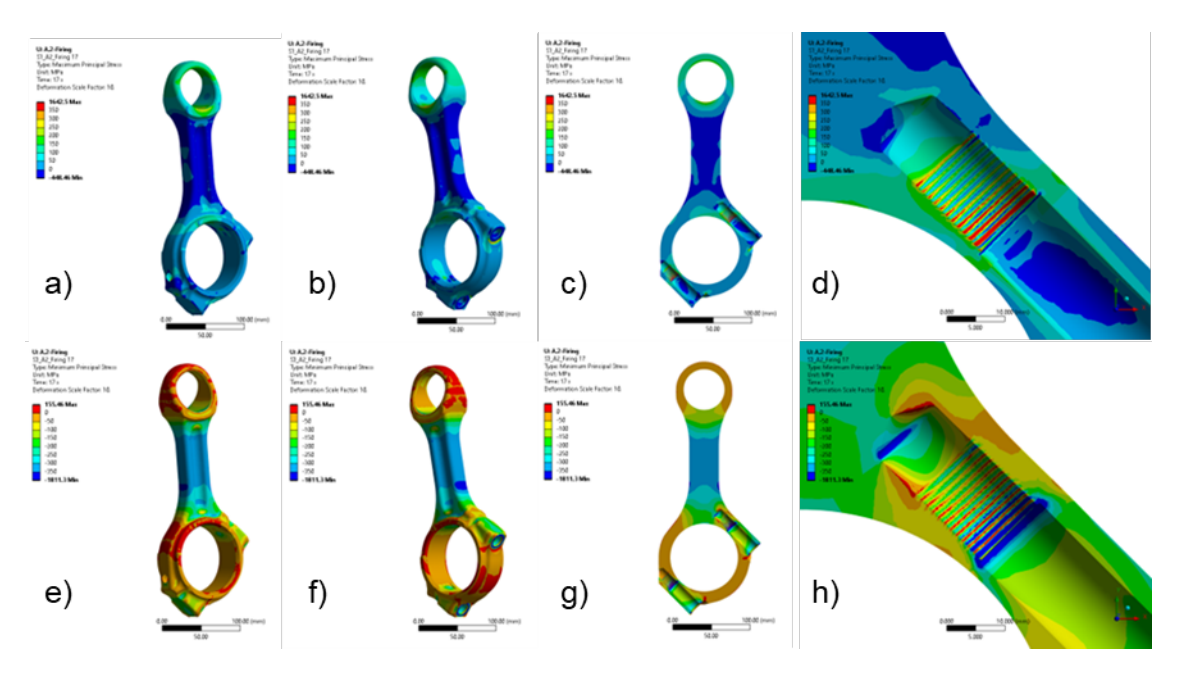


Figure 0.2 A2 Firing Max & Min Principal Stress at 1,900 r.p.m.

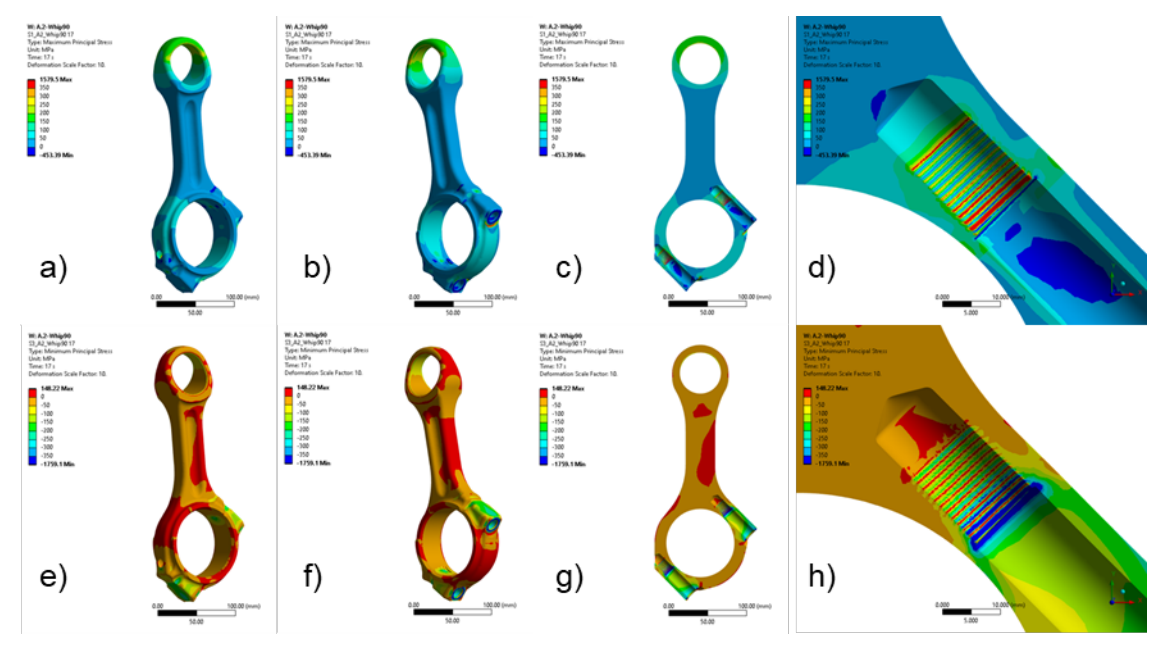


Figure 0.3 A2 Whip 90° Max & Min Principal Stress at 1,900 r.p.m.

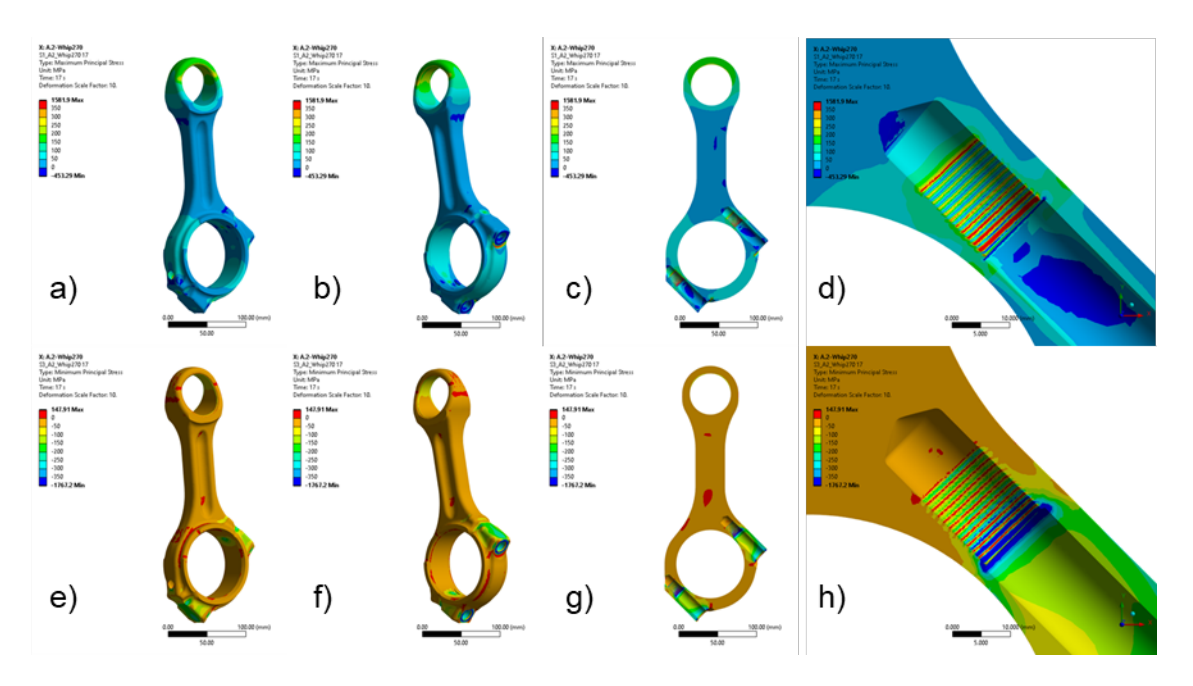


Figure 0.4 A2 Whip 270° Max & Min Principal Stress at 1,900 r.p.m.

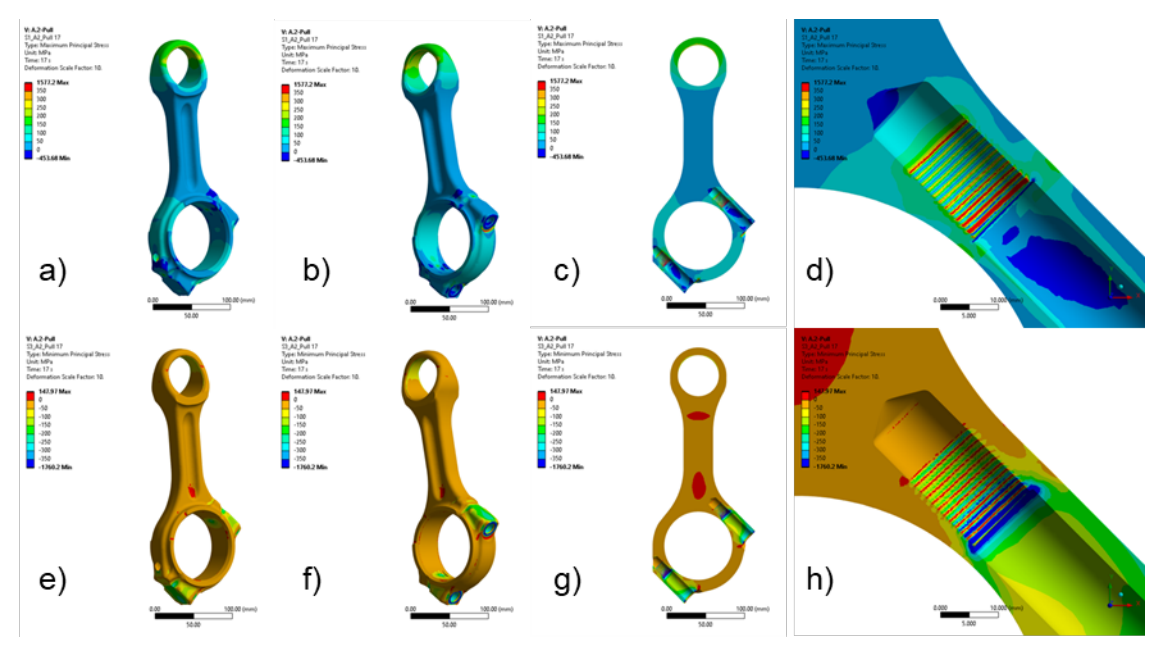


Figure 0.5 A2 Pull Max & Min Principal Stress at 1,900 r.p.m.

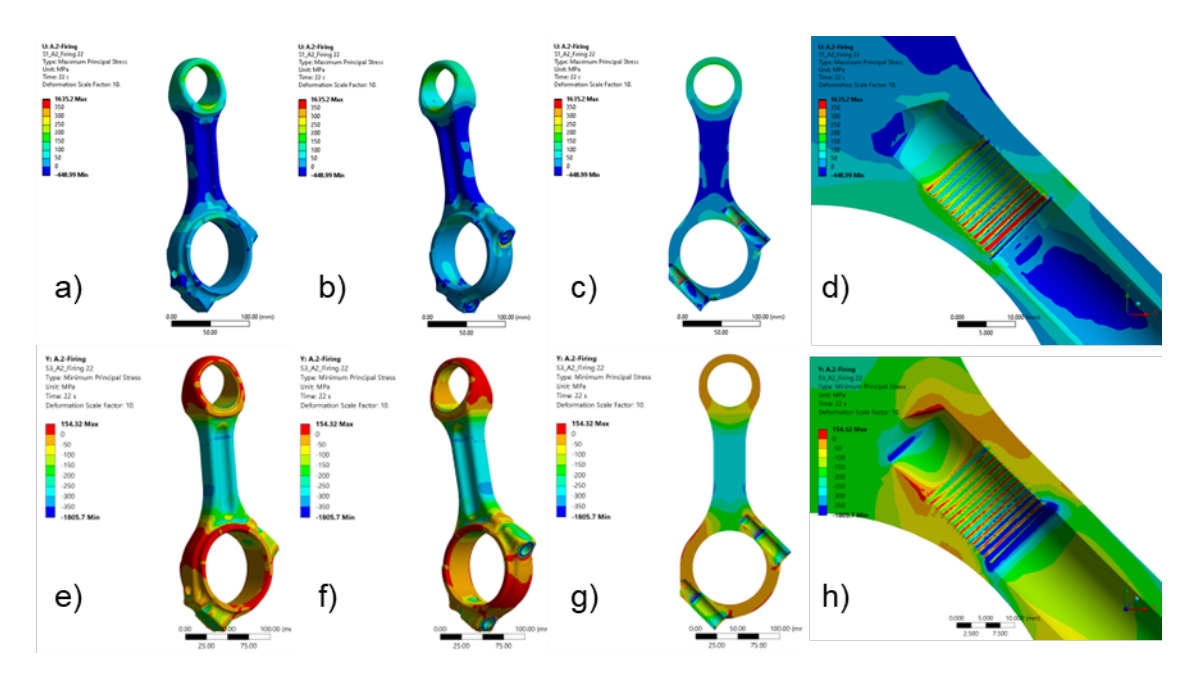


Figure 0.6 A2 Firing Max & Min Principal Stress at 2,400 r.p.m.

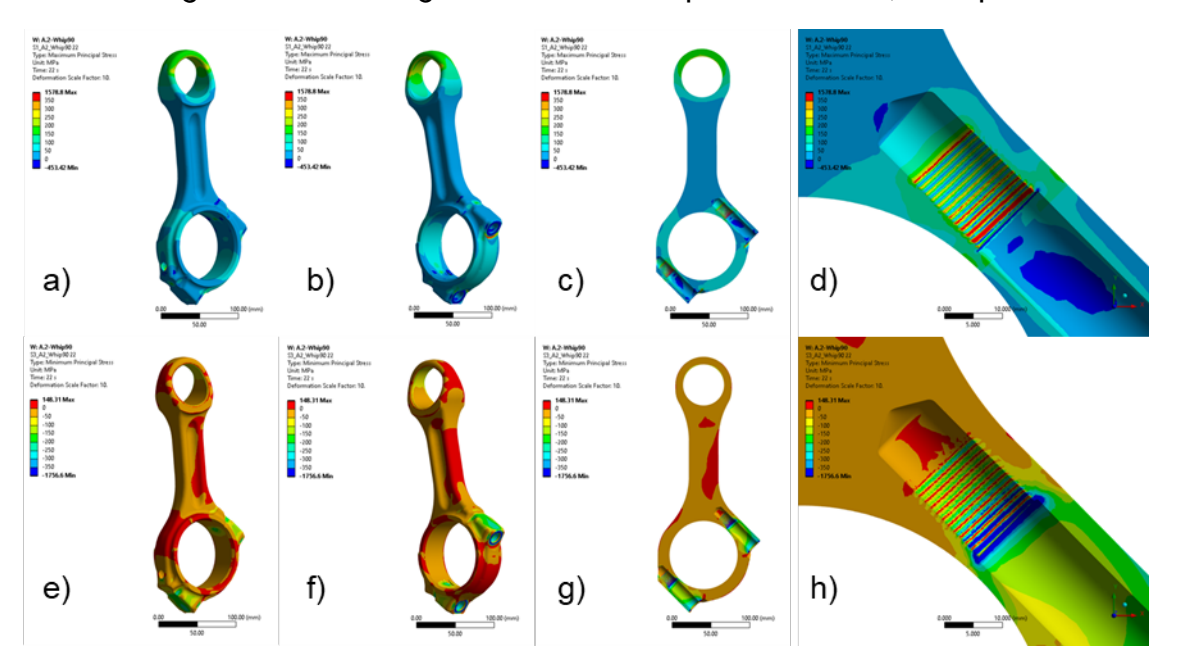


Figure 0.7 A2 Whip 90° Max & Min Principal Stress at 2,400 r.p.m.

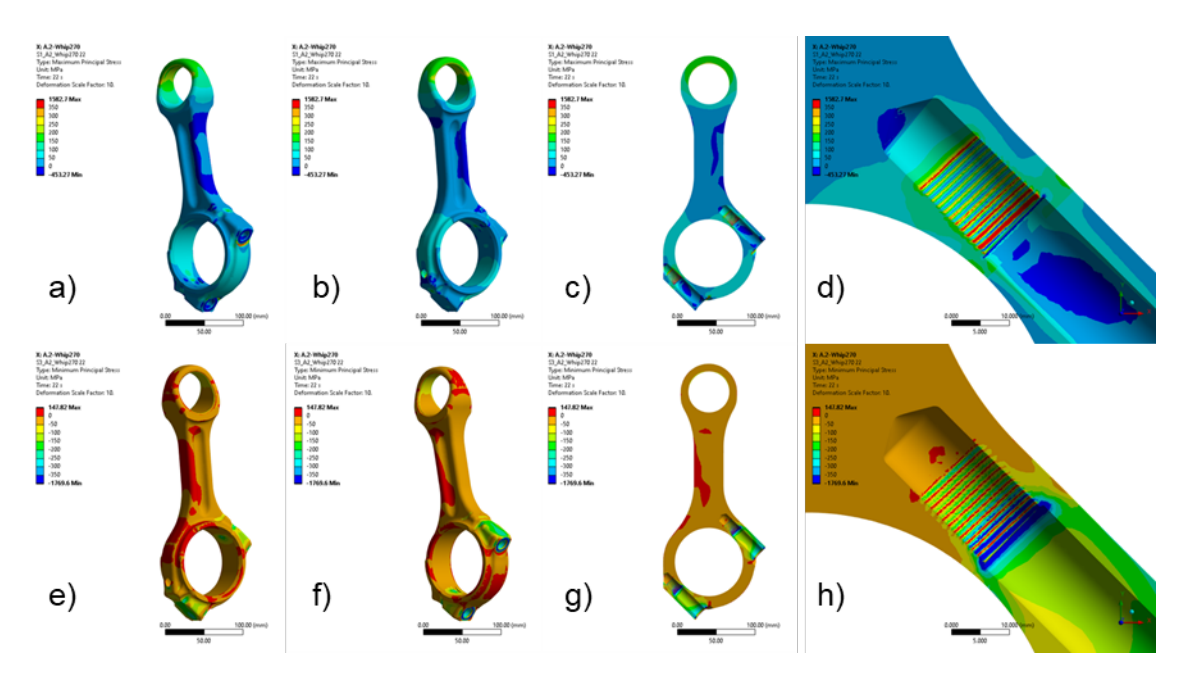


Figure 0.8 A2 Whip 270° Max & Min Principal Stress at 2,400 r.p.m.

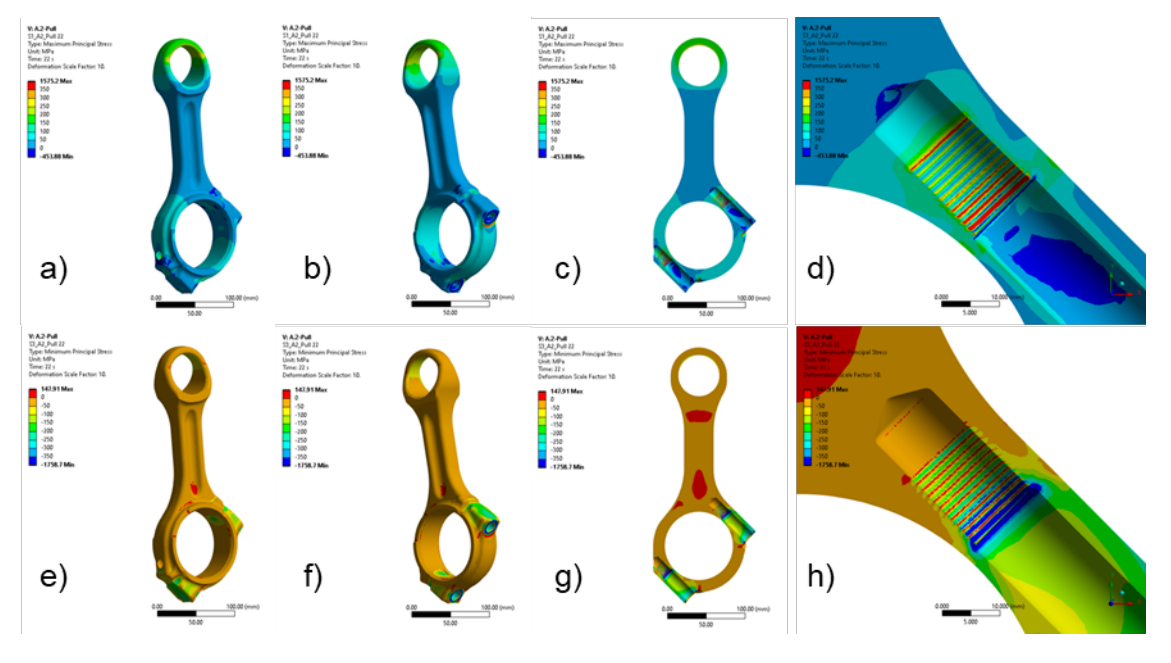


Figure 0.9 A2 Pull Max & Min Principal Stress at 2,400 r.p.m.

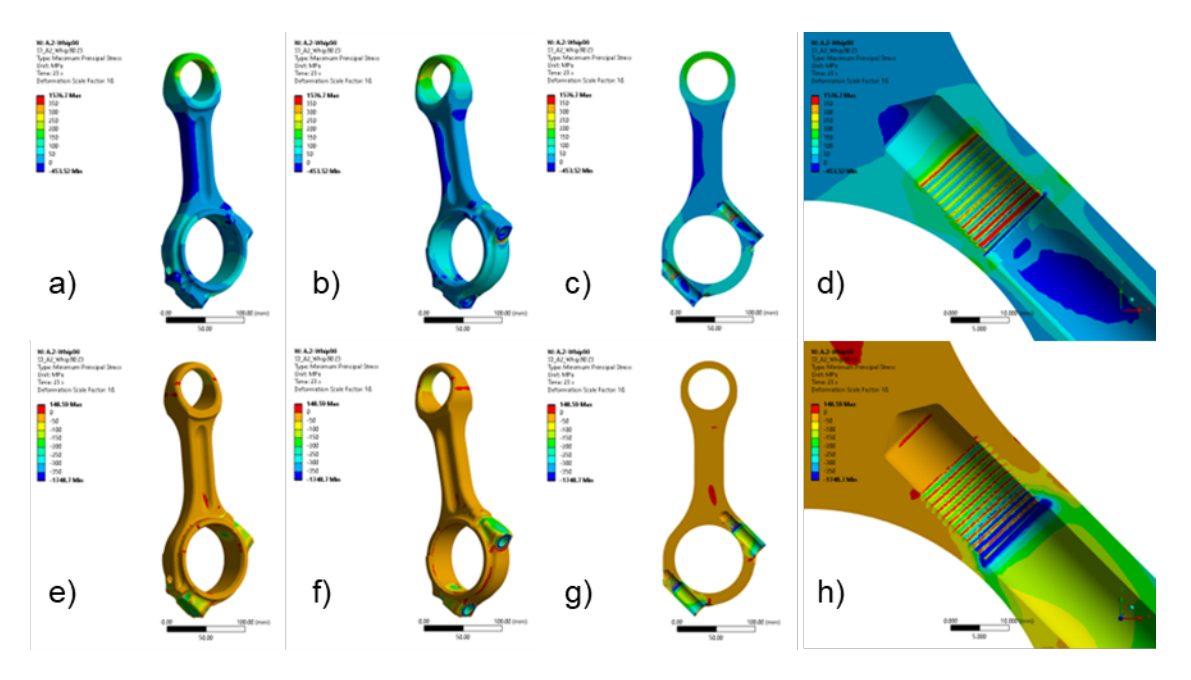


Figure 0.10 A2 Whip 90° Max & Min Principal Stress at 3,600 r.p.m.

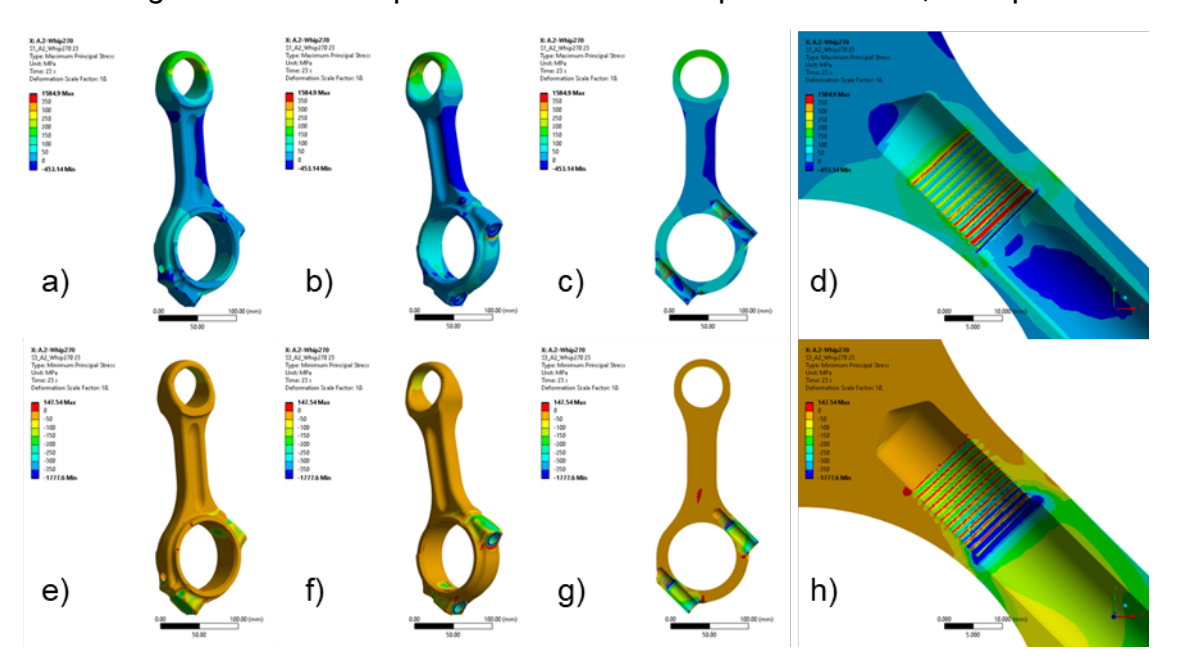


Figure 0.11 A2 Whip 270° Max & Min Principal Stress at 3,600 r.p.m.